© Antonis Iacovou Vakis

NANOSCALE INTERFACE MECHANICS WITH APPLICATION TO MAGNETIC STORAGE

BY

ANTONIS IACOVOU VAKIS

DISSERTATION

Submitted in partial fulfillment of the requirements
for the degree of Doctor of Philosophy in Mechanical Engineering
in the Graduate College of the
University of Illinois at Urbana-Champaign, 2011

Urbana, Illinois

Doctoral Committee:

Professor Andreas A. Polycarpou, Chair and Director of Research
Professor Lawrence A. Bergman
Associate Professor Ioannis Chasiotis
Associate Professor Christoforos N. Hadjicostis

ABSTRACT

The study of the mechanics and dynamics of nanoscale interfaces is of great interest, particularly for cutting-edge applications such as magnetic storage, which arguably constitutes the most successful application of nanotechnology. The goal in magnetic storage is to increase the recording density by reducing the physical spacing between the magnetic layer of the disk and the recording elements, which, in commercial hard disk drives, is of the order of few nanometers. Achieving this goal entails the understanding of the physics at the head-disk interface and being able to reliably predict system performance in terms of flyability and contact. This dissertation presents continuum, physics-based models of the head-disk interface that were validated through comparisons with experimental and atomistic simulation data. A novel model is presented for dynamic contact with molecularly thin lubricant layers that exhibit solid-like responses under extremely high shear rates. The limits of continuum theory were investigated based on experimentally measured response of such lubricant layers and accounted for during lubricant contact. The comprehensive models were used to investigate and optimize the design of hard disk drives for near-contact recording. Having reached the physical limits of traditional magnetic recording, these models should prove useful in the design and implementation of future nanotechnologies.

To my family

ACKNOWLEDGEMENTS

This work would not have been possible without the help, guidance and support of my adviser, Professor Andreas A. Polycarpou. I would like to thank Professors Lawrence A. Bergman, Ioannis Chasiotis and Christoforos N. Hadjicostis for their help. Special thanks to Melih Eriten for our very useful discussions and to the other members of the Microtribodynamics laboratory at the University of Illinois, past and present, for their help. Last but not least, I would like to thank Stefania and my family in Cyprus for their continued patience, love and support.

Financial support for this research was provided in part by the Information Storage Industry Consortium, INSIC, and the Cyprus Research Promotion Foundation's Framework Program for Research, Technological Development and Innovation 2009–2010 (DESMI 2009–2010), co-funded by the Republic of Cyprus and the European Regional Development Fund, under Grant PENEK/0609/03.

TABLE OF CONTENTS

Chapter 1 – Introduction 1
1.1: TFC Nanotechnology 1
1.2: MTL Layers in Magnetic Storage 4
1.3. Research Outline 8
1.4: Nomenclature 9
Chapter 2 – Two-DOF Dynamic Contact Model for TFC Nanotechnology 12
2.1: Two-DOF Model 12
2.2: Improved Two-DOF Model with Rigorous Definition of Contact 21
2.3: Optimization for Near-Contact Recording 37
2.4: Summary 47
2.5: Figures 50
2.6: Tables 62
Chapter 3 – MTL Contact Model 65
3.1: Sphere-on-flat Model of MTL Contact 65
3.2: Sliding Contact of Rough Surfaces with MTL Layers 88
3.3: Summary 103
3.4: Figures 104
3.5: Tables 112
Chapter 4 – Lubricant Contact for TFC Sliders 113
4.1: Three-DOF Dynamic Contact Model with Lubricant Contact 113
4.2: Summary 133
4.3: Figures 134
4.4: Tables 139
Chapter 5 – Conclusions 142
5.1: Summary 142
5.2: Recommendations for Future Work 143
References 144
Appendix A 153
A.1: ISBL Contact Model Equations 153
A.2: MTL Contact Model Equations 155
Appendix B 157
B.1: The Role of Dynamic Excitation 157

B.2: Figures 160
Appendix C 165
C.1: Roughness Measurements 165
C.2: TFC Geometry Measurements 167
C.3: Figures 169

CHAPTER 1 – INTRODUCTION

While the scope of this research has been application-specific, with focus on thermal fly-height control (TFC) nanotechnology in magnetic storage, investigation into fundamental questions on the nature of molecularly thin lubricant (MTL) layers, presented in Chapter 3, forms a major part of the dissertation. The comprehensive model presented in Chapter 4 combines the earlier TFC nanotechnology models (Chapter 2) with the MTL contact model (Chapter 3) to provide insight into the role of lubricant parameters, morphology and chemistry, to the response at the head-disk interface (HDI).

1.1: TFC NANOTECHNOLOGY

TFC nanotechnology was implemented in commercial hard disk drives (HDDs) to achieve Tbit/in^2 recording densities. The HDI consists of a slider flying at a prescribed height (few nanometers) over a rotating, multi-layered, magnetic disk. The slider is balanced by the suspension and applied preload on one hand, and the air bearing (AB) created by the flow of air between the slider and disk surfaces on the other. For nanometer-level separations, intermolecular adhesive forces act to bring the slider and disk into contact and induce slider vibrations when the surfaces are in proximity. It is desirable to reduce vibrations in order to maintain recording signal integrity, as well as avoid contact between the solid substrates altogether so as not to catastrophically damage the magnetic disk.

Instead of bringing the entire slider closer to the disk, TFC nanotechnology works by thermo-mechanically actuating a small volume around the read/write elements to bring them closer to the rotating disk surface without compromising system stability at sub-5-nm flying heights (FHs) [1]. A number of studies have been published on the performance of TFC sliders. Of these, several focus on the effect of AB design to flyability through numerical simulations [2-5], while others utilize experiments to either validate AB simulation results [6, 7] or investigate the dynamics and the various regimes of contact [8, 9]. System-level, lumped parameter models encompassing both flying and contacting of TFC sliders are fewer in number [4, 6, 9-12] but have been useful, for example, in performing TFC optimization studies for flyability and contact

severity [13]. In comparison, component-level models that utilize coupled-field analyses [14-16] are computationally intensive and cannot be easily used in parametric or optimization studies.

A system-level, lumped parameter, 2-degree-of-freedom (DOF) dynamic contact model specific to TFC nanotechnology was introduced by the author in 2009 [11], and allowed for the calculation of the dynamically changing mechanical clearance between the read/write elements and the disk along with the interfacial forces, namely adhesion, contact and friction. The definition of contact was systematically defined as a function of the clearance between the two solid surfaces. Negative clearance corresponds to solid contact with the protective diamond-like carbon (DLC) overcoat, which results in significant wear and is generally undesirable at the HDI, while positive clearance corresponds to either fully flying or light contact within the lubricant layer (near-contact recording). Operation within the latter regime, also termed "surfing" recording, is deemed a desirable alternative to contact recording and is based on the assumption that MTL layers, behaving as semi-solids at very high shear rates [17], could provide sufficient bearing and protection to the disk [18]. In the absence of contact models that included the effects of lubricant behavior, the lubricant layer was until recently modeled as being displaced by the slider without resistance during contact [10, 11].

The improved sub-boundary lubrication (ISBL) contact model, summarized in Appendix A, was used to calculate the forces and real area of contact at the HDI during solid contact [19]. The model uses physics-based formulations for adhesion, contact and friction forces with respect to the separation between an equivalent smooth flat and a rough surface. The forces are dimensionalized with respect to the nominal area of contact, which is analytically calculated for a specific TFC geometry as a function of protrusion height. While other researchers have used similar models investigating TFC flyability and partial contact [20-22], the strength of the ISBL model lies in its use of surface roughness and material properties as the only inputs to the calculation of the interfacial forces, without the use of empirical coefficients. Using the improved dynamic contact model with the exact TFC geometry, the identification and definition of the contact criterion as a function of surface roughness were investigated. The onset of contact was correlated with touchdown (TD) experiments using TFC sliders. This approach was used in the initial 2-DOF model [11]; subsequent dynamic models consistently defined contact as

occurring for separations smaller than three standard deviations of the combined surface roughness instead [10, 12, 13, 23, 24].

In addition to topographical roughness and material parameters that were used as inputs for the contact model, dynamic microwaviness (DMW) was measured experimentally and used as the dynamic input to the models. An investigation into the nature of DMW is presented in Appendix B. Stiffening of the rear AB spring force as a function of TFC actuation was reported in the literature [7] and was included in the improved 2-DOF model [10]. The complex overall behavior of the system was described as a function of TFC actuation and various operating regimes were identified and characterized by three quantities: clearance, vibrations and the contact severity [10, 13].

Two-DOF models of conventional non-TFC sliders were deemed sufficient in capturing dynamic AB behavior [25]. Indeed, as will be shown in Chapter 2, such models are able to successfully capture experimentally observed instabilities when TFC sliders are close-to, into and out-of contact with the disk [4, 10]. Even though past work was published with multi-DOF models that have focused, for example, on the slider suspension [26] or secondary slider structures [27], the third DOF of the slider, roll, was not included in any of the lumped parameter models until recently [24]. Including the roll DOF has been shown to be important within the context of operational shock where the contact pads are brought into contact with the disk, whereas only the TFC bulge comes into contact during normal operation as predicted by 2-DOF models. More importantly, the 3-DOF model presented in Chapter 4 includes the effects of lubricant contact through a new contact model introduced by the author, termed the MTL contact model. The MTL model is explained in detail in Chapter 3, while its formulation is summarized in Appendix A.

1.2: MTL LAYERS IN MAGNETIC STORAGE

MTL layers are used in nanotechnology to lubricate and protect contacting surfaces. In magnetic storage, the disk and slider are coated with 2-nanometer thick DLC films to protect against accidental contact, while the disk is also coated with a polymeric lubricant layer of atomic thickness that also protects against corrosion [10, 11, 13]. The presence of this lubricant layer alters the surface energy of the disk and, in turn, the adhesive forces acting on the slider, thereby affecting its dynamic response. Furthermore, as the flying clearance between the slider and disk is sought to be minimized to increase storage density, possible operation within the lubricant layer – referred to as "lubricant contact" – cannot be simplified by assuming that the lubricant is readily displaced upon contact, and that it offers no resistance to shearing and compression. While the effect of MTL layers on adhesion has been studied previously, e.g. in [28], until recently, there has been a lack of models predicting normal and shear forces during contact with such layers.

Polymeric lubricants confined in nanometer-scale gaps can have different rheological properties from the bulk [29, 30]. For example, when lubricant molecules are confined between two solid surfaces that slide past each other with high velocities, the lubricant viscosity starts to increase at gaps smaller than a few hundred nanometers; similarly, elasticity appears suddenly when the gap becomes smaller than a few nanometers and both viscosity and elasticity increase monotonically with decreasing gap. Then, the viscoelastic properties of the film start to differ from those of the bulk and exhibit enhanced shear viscosities or prolonged relaxation times. This is considered to be caused by a confinement-induced, glasslike transition of the polymer chains at very high shear rates [31], which, in magnetic storage, can be of the order of 10^{10} s^{-1} [32]. Sliding velocity is a critical parameter such that viscous forces dominate at the interface [33].

Interfacial slip is expected to occur at the nanoscale as well. Several authors have performed experiments [34-36] and molecular dynamics simulations [37-40] to investigate interfacial slip in sheared films. At low shear rates, the slip length depends strongly on velocity [36]; however, at high shear rates, such as those encountered in magnetic storage, the slip length approaches a constant value that depends on the material properties of the solid [37]. The effects of viscosity stiffening and interfacial slip are expected to be coupled in experimental measurements of the

shear response. It is possible to decouple their effects by making certain assumptions about the state of "friction" at the interface where slip occurs, and applying these to the viscosity and slip models.

An experimental technique, referred to as the fiber wobbling method (FWM), was developed in 2003 to measure the dynamic shear force at high shear rates with precise gap control [30], and was based on a modified surface force apparatus (SFA) [41, 42]. Unlike the SFA, which used atomically smooth mica surfaces as substrates, the FWM utilizes a vibrating spherical probe to shear a liquid parallel to a rough, rigid substrate such as a magnetic storage disk. Since liquid confined in nanometer-scale gaps is expected to be non-Newtonian, an effective (dynamic) viscosity, represented by a complex function of the real (in phase) and imaginary (out of phase) components, is measured in dynamic shearing experiments [31]. The real and imaginary components are termed viscosity η' and elasticity η'', respectively [41]. While elasticity – and local intermolecular interactions [35] – dominate in atomically smooth surfaces (with the SFA) [29, 33, 41], this picture is reversed when roughness is present (in the FWM): the effect of roughness seems to be that it loosens the confinement of molecules such that the viscosity dominates the elasticity [31], while meniscus forces do not appear to play a role in the response [36].

A double-ended tuning fork (DETF) resonator [43] was recently added to the FWM apparatus to simultaneously measure the vertical force. The dynamic viscosity obtained from FWM measurements was used with classical continuum theory to predict the normal (bearing) force acting on the shearing probe [44]. Agreement with the experimentally measured force indicates that continuum theory can adequately predict the lubricant behavior, under certain considerations. Specifically, experiments that utilize bulk fluid – even if that is a micron-sized droplet – correspond well to continuum theory because the bulk dominates the shear response. In contrast, the same approach has limitations in the case of molecularly thin films where breakdown of continuum occurs. This was investigated by interpreting available experimental and molecular dynamics simulations results, and proposing a model of the lubricant morphology at the interface that captures the behavior of lubricant molecules under shear. Experiments with molecularly thin layers, rather than bulk droplets, would help illustrate the potential validity of

this model when continuum breaks down. A semi-empirical, partially-submerged sphere-on-flat model was proposed that can predict the hydrodynamic normal (bearing) and shear forces in the presence of scale effects, such as the breakdown of continuum and interfacial slip, as well as confinement and high shear rates in an MTL layer [23].

A rough surface model of MTL contact was presented in recent work [24], which builds on the single asperity model [23] that accounts for dynamic shearing experiments with polymeric thin lubricants [44]. The MTL model was coupled with the existing ISBL rough surface dynamic contact model with friction [10, 45], extended to include variable surface energy according to recent experimental measurements [46, 47]. Lubricant thicknesses used in the dynamic shearing experiments were of the order of a few hundred microns. MTL layers, on the other hand, have thicknesses of few nanometers. Molecular dynamics (MD) simulations have shown that wall interaction and molecular end-group functionality affect the behavior of the lubricant layer, while lubricant confinement (separation between the solid surfaces) and shear rate were found to play a critical role in determining the lubricant's liquid- or solid-like response [29, 33]. It was proposed [23] that the forces in MTL layers could be adequately extrapolated up to the expulsion of mobile lubricant molecules from the interface because the main effects of confinement and wall interactions/end-group functionality (slip behavior) are captured in the dynamic shearing experiments [30, 31, 44].

The solid surface root-mean-square (RMS) roughness was sufficiently small in the experiments [44] – of the order of the average combined thickness of the bonded molecule layers – to be engrossed in the transition region between steady lubricant and steady solid contact; this allowed for the effective decoupling of hydrodynamic contact from the transition region where lubricant film rupture and roughness effects (i.e., asperity contact) come into play [23]. However, while displacement-control results in clearly distinguishable regimes of steady lubricant, transitional and solid contact in the experimental data, the statistical nature of contact would dominate the interface otherwise such that the response would transition directly from lubricant to solid contact in non-displacement-control settings. The MTL model proposed that the interface transitions from MTL to solid contact once the solid-solid gap becomes smaller than the minimum liquid thickness [24].

Interfacial or intermolecular adhesion is very important in nanoscale contacts such as those found at the HDI of HDDs [10, 19, 48]. In the presence of MTL layers, adhesion was successfully accounted for in models such as the Sub-boundary Lubrication (SBL) model [28], where meniscus formation is deemed energetically unfavorable due to the thinness of the lubricant film and the adhesive force was calculated based on the Lennard-Jones surface potential [49]. Experimental work showed that the surface energy of MTL layers on solid substrates is not constant but varies with penetration into the lubricant layer [46]. Hence, an adhesion formulation for non-contacting and lubricant contacting asperities – in the context of a Greenwood-Williamson (GW) formulation of roughness – was presented that accounts for variations on the surface energy. MTL layer contact with variable surface energy was combined with the ISBL contact model with friction [10, 45] into the proposed MTL dynamic contact model, which is discussed in correlation to available experimental data [46, 47].

1.3. RESEARCH OUTLINE

At the time of writing, the research presented in this dissertation has been published in peer reviewed journal articles [10, 11, 13, 23, 24], except from the content of Chapter 4 that was only recently submitted for publication [12]. Chapter 2 presents 2-DOF dynamic contact model formulations for TFC nanotechnology sliders, based on the ISBL contact model, without accounting for lubricant contact [10, 11]. The improved 2-DOF model is used in optimization studies of TFC slider design [13]. Chapter 3 contains the MTL contact model. A sphere-on-flat model was introduced first to interpret dynamic shearing experimental results [23]; this was extended for rough contacts and extremely high shear rates, and was coupled with the ISBL model to comprehensively characterize contact at the HDI [24]. Finally, a 3-DOF model is presented in Chapter 4 that accounts for the roll DOF as well as lubricant contact for TFC nanotechnology sliders [12].

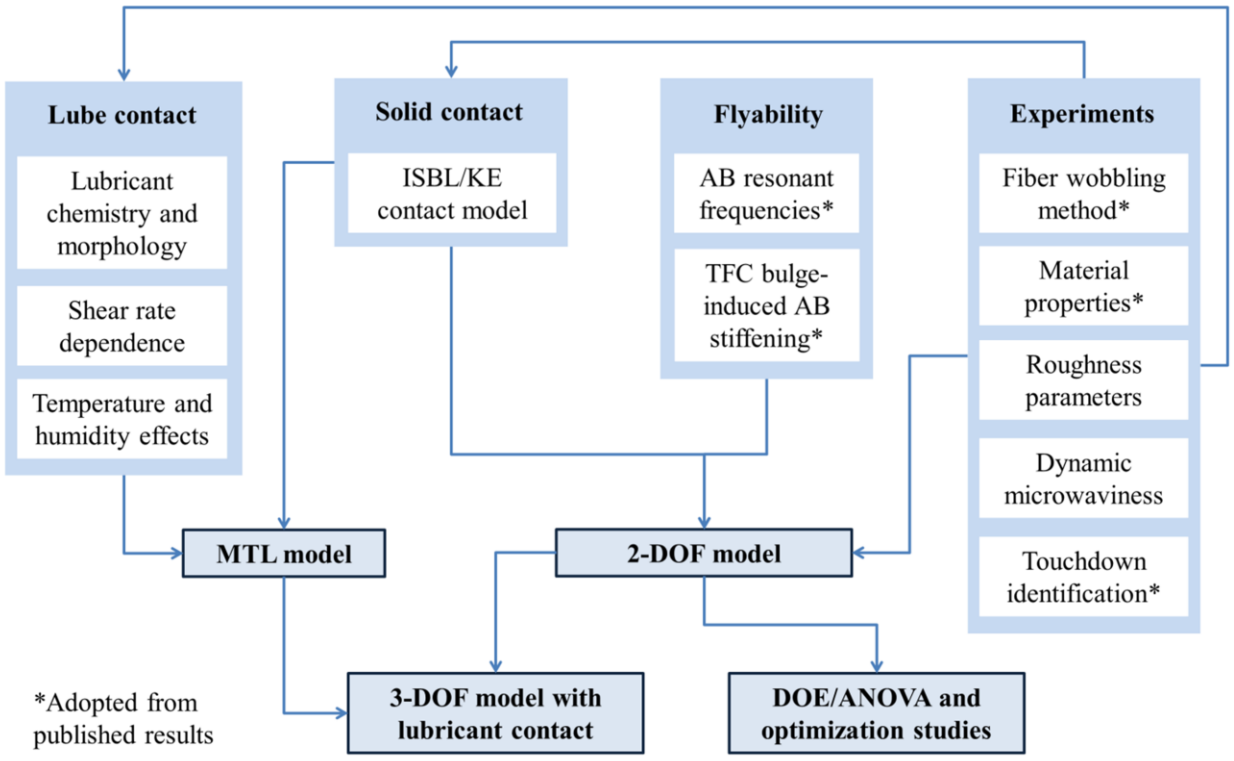


Figure 1.1: Research outline flow chart.

1.4: NOMENCLATURE

The following tables list the acronyms and symbols used throughout this dissertation. Because of the large number of symbols, special care should be taken to distinguish between those used in the dynamic contact and MTL models as detailed in Table 1.2 and Table 1.3. Specifically, lowercase h refers to the mean plane separation of surface heights in the dynamic contact models (Chapter 2, Chapter 4), but denotes film thickness in the MTL model (Chapter 3). Similarly, H refers to material hardness within the context of the dynamic contact models, or the Heaviside function for lubricant contact; R is the combined asperity radius, or the spherical probe radius respectively; ζ is the suspension damping for normal displacement, or the normalized y-coordinate; η is the combined areal density of asperities, or viscosity; ξ is the flyability optimization parameter, or the normalized x-coordinate; and, τ is the shear traction, or the shear stress on the sphere. Finally, the coefficient of friction is μ, while μ_0 in Chapter 4 refers to the limiting (maximum) viscosity, denoted as η_0 in Chapter 3.

Table 1.1: List of acronyms.

AFM	Atomic force microscopy
ABS	Air bearing surface
BV	Bouncing vibrations
CP	Critical point (in optimization studies)
COM	Center of mass
DLC	Diamond-like carbon
DMW	Dynamic microwaviness
DMT	Derjaguin-Muller-Toporov (model)
DOF	Degree of freedom
FH	Flying height
FHM	Flying height modulation
GW	Greenwood-Williamson (model)
HDD	Hard disk drive
HDI	Head-disk interface
HGA	Head-gimbal assembly
HMS	Head-media spacing
ISBL	Improved sub-boundary lubrication (model)
LE	Leading edge
PFPE	Perfluoropolyether (lubricants)
POC	POC
TD	Touchdown
TE	Trailing edge
TFC	Thermal fly-height control

Table 1.2: List of symbols used in dynamic model formulations.

A_n	Nominal area of contact	T_0	Bonded lubricant thickness
A_r	Real area of contact	w_{BASE}	TFC base width
a_{TFC}	TFC ellipsoid semi-width (also a_{TFC})	w_{TFC}	TFC ellipsoid width
b_{TFC}	TFC ellipsoid height	x_{PAD}	Contact pad offset along length
d	Mean plane separation (asper. heights)	x_R	Reader offset from ellipsoid
d_f	Front AB spring offset	x_{TFC}	TFC ellipsoid offset from TE
d_r	Read AB spring offset	x_W	Writer offset from ellipsoid
e	Suspension offset from COM	y_{PAD}	Contact pad offset along width
E_{DISK}	Disk elastic modulus (also E_2)	z	COM displacement (also z_{COM}, z_G)
E_{TFC}	Slider elastic modulus (also E_1)	z_f	Front AB spring displacement
F	Suspension preload	z_r	Rear AB spring displacement
F_c	Dynamic contact force	z_t	TE center displacement
FH_{lim}	Limiting FH	$\Delta\gamma$	Surface free energy
FH_{nom}	Nominal FH (also *nom.* FH)	ε	Equilibrium spacing
F_s	Adhesive force	ζ	Suspension normal damping ratio
h	Mean plane separation (surf. heights)	ζ_c	Solid contact damping ratio
H	Hardness	ζ_f	Front AB spring damping ratio
h_S	Recession step height	ζ_l	Lateral AB spring damping ratio
h_{TFC}	TFC actuation	ζ_r	Rear AB spring damping ratio
J	Pitch moment of inertia	ζ_θ	Suspension pitch damping ratio
k	Suspension normal stiffness	ζ_φ	Suspension roll damping ratio
k_θ	Suspension pitch angular stiffness	η	Combined asperity areal density
k_φ	Suspension roll angular stiffness	η_{DISK}	Disk asperity areal density (also η_2)
l	Slider length	η_{TFC}	Slider asperity areal density (also η_1)
l_S	Recession step length	θ	Pitch angle
l_t	Slider thickness	θ_0	Initial pitch angle
l_w	Slider width	μ	Coefficient of friction
m	Slider mass	ν_{DISK}	Disk Poisson ratio (also ν_2)
P	Contact force	ν_{TFC}	Slider Poisson ratio (also ν_1)
p_m	Mean pressure	ξ	Flyability optimization parameter
Q	Friction force	σ	Combined RMS roughness
R	Combined mean asperity radius	σ_{DISK}	Disk RMS roughness (also σ_2)
R_{DISK}	Disk mean asperity radius (also R_2)	σ_{TFC}	Slider RMS roughness (also σ_1)
R_{PAD}	Contact pad radius	τ	Shear traction
R_{TFC}	Slider mean asperity radius (also R_1)	φ	Roll angle
t	Total lubricant thickness	φ_0	Initial roll angle

Table 1.3: List of symbols used in MTL model formulation.

A	Oscillation amplitude	u_s	Slip velocity
a, b	Viscosity-gap model coefficients	u_s*	Dimensionless form of u_s
a', b'	Viscosity-shear rate model coefficients	u_w	Wall velocity (as boundary condition)
C	Molecular coverage of surface area	v	Fluid velocity in y-direction
c	Damping coefficient (for fluid "contact")	v*	Dimensionless form of v
d_0	Liquid gap	$\dot{\gamma}$	"Apparent" shear rate
f	Driving frequency of oscillation	$\dot{\gamma}_{true}$	"True" shear rate (accounting for slip)
f*	Dimensionless slip factor	ζ	Normalized y-coordinate
G'	Storage modulus	η	"Apparent" viscosity
G''	Loss modulus	η_{true}	"True" viscosity (decoupled from slip)
G*	Complex modulus	η_w	Wall friction (liquid-solid coupling)
H	Heaviside function	η_0	Maximum limiting viscosity
h	Film thickness	η_∞	Bulk viscosity
h_B	Average molecular height of bonded layer	η'	Viscosity ($\eta = \eta'$)
h_0	Solid-solid gap (minimum film thickness)	η''	Elasticity
L_s	Slip length	η*	Complex viscosity
p	Pressure	R	Sphere (probe or asperity) radius
P_{fluid}	Normal (bearing) hydrodynamic force	S	Spherical cap area
P_{solid}	Normal solid force	κ	Minimum liquid gap
P_{trans}	Normal transitional force	ξ	Normalized x-coordinate
Q_{fluid}	Shear hydrodynamic force	σ	Root-mean-square roughness of substrate
Q_{solid}	Solid friction force	τ	Shear stress on sphere surface
Q_{trans}	Shear transitional force	Ω	Geometric factor
t	Total lubricant layer thickness	$\Omega_{f\text{-}s}$	Geom. f. for fully-submerged sphere
U	Shearing velocity	$\Omega_{p\text{-}s}$	Geom. f. for partially-subm. sphere
u	Fluid velocity along x-direction	ω	Solid interference
u*	Dimensionless form of u		

CHAPTER 2 – TWO-DOF DYNAMIC CONTACT MODEL FOR TFC NANOTECHNOLOGY

2.1: TWO-DOF MODEL

2.1.1: Dynamic HDI Model with TFC

In an earlier dynamic HDI model without TFC [19], when the slider is flying without contacting the disk, a non-linear AB force F_{ar} is acting together with a linear damping force on the trailing edge (TE). An analogous AB force is acting on the leading edge (LE) of the slider with both the stiffness and damping terms being linear. Under flying equilibrium conditions, the slider dynamics are dependent upon the AB and adhesive forces as well as the suspension dynamics. When contact occurs, a contact force F_c, calculated from the roughness parameters and modeled as non-linear contact stiffness k_c and linear damping c_c, together with a friction force Q, are added to the force balance at the point of contact (POC).

The model presented in [19] was modified such that the lowest point of the TFC protrusion becomes the POC. The TFC protrusion is modeled as an ellipsoid that has a fixed base profile with its height relative to the bottom of the slider being the only changing variable. The exact shape of the TFC geometry (bulge) could be accurately predicted using, for example, finite element analysis. Using such data, one can then extract the geometry of the top surface of the bulge that is engaged during contact and use it to construct the ellipsoidal TFC model, as was done in the present work. The TFC geometry model is characterized by four parameters: a_{TFC}, h_{TFC}, w_{TFC} and x_{TFC}. For the specific TFC design used in this work, the half-width a_{TFC} was measured to be equal to 3 μm; the distance of the TFC ellipsoid from the TE x_{TFC} was equal to 8 μm; and, the width in the direction perpendicular to the plane (shown in Figure 2.1) w_{TFC} is equal to 50 μm. The TFC bulge height h_{TFC} varies between zero (no actuation) and 15 nm (maximum actuation). The TFC protrusion height is of the order of few nm as opposed to the TFC base dimensions that are of the order of few μm; hence, the TFC protrusion height is greatly exaggerated in Figure 2.1. The contact and friction forces are acting on the lowest instantaneous point of the TFC protrusion, whose position can be accurately described in terms of a fixed reference point such as the TE.

Figure 2.2 depicts the 2-DOF dynamic model of the HDI with the TFC protrusion along with the interfacial forces developed during different characteristic states. The first state, labeled as *flying condition,* is characterized by the slider flying over the disk without contact under the influence of the AB and adhesive forces. The adhesive force is acting on the TFC situated close to the TE as shown in inset a) of Figure 2.2. The second state, labeled as *contact condition*, occurs when the TFC contacts the disk based on the established contact criterion. In this case, in addition to the AB and adhesive forces, contact and friction forces are also acting on the TFC as shown in inset b) of Figure 2.2.

2.1.1.1: ISBL Interfacial (Contact- Adhesion-Friction) Model

The ISBL interfacial model including roughness, summarized in Appendix A, was presented elsewhere, e.g. [19], and is used to calculate the adhesion, contact and friction forces as well as the real area of contact using roughness, material and lubricant properties. The model does not assume a predefined friction coefficient value but instead calculates it directly from the interfacial forces. The total adhesive force is calculated from the individual asperity contributions using a statistical GW-type (includes plastic deformation) roughness model. The total adhesive force combines the contributions from non-contacting asperities, lubricant contacting asperities (lubricant layer is strongly adhered to the surface), and elastically and elastically-plastically deforming asperities.

The total normal contact force calculation considers the contribution of elastic, elastic-plastic and fully-plastic contacts. The model assumes that the lubricant layer is displaced during contact and the contact force is not affected by the presence of the thin lubricant layer, i.e. the contact force is due to the asperity deformation. Further improvements in the model should also include the lubricant contact/friction forces. The total friction force is calculated based on the contributions of elastically and elastically-plastically deforming asperities. The real area of contact is calculated from the contributions of elastically, elastically-plastically, and fully plastically contacting asperities.

2.1.1.2: AB Stiffness and Model Parameters

The complex nature of a slider AB is best described by three DOFs, i.e. vertical, pitch and roll motions, through a generalized Reynolds pressure field equation beneath the AB surface (ABS). A 2-DOF model including the vertical and pitch modes is adequate for capturing the basic dynamic AB behavior [19], which is adopted in this work. In the present model, it is assumed that the slider maintains the same FH, equal to the nominal value of 11 nm, throughout the actuation of the TFC protrusion until contact is initiated. This simplifying assumption allows for the use of a constant rear AB stiffness k_r, which can be calculated from the natural frequencies of the AB. As discussed in [18, 50] the AB dynamics are affected by the thermal effects of the TFC, which is not considered in the present work. Nevertheless, as the model is using experimental TD measurements to correlate with the model predictions, some of these complex effects are indirectly captured by the model. As the main goal of this study is to use a physics-based dynamic contact model to predict FH modulation (FHM) and friction under light contacting conditions, the present assumption is justified.

The natural frequencies of the specific AB used in the present study were found to be 119.1 kHz and 304.8 kHz for the first and second modes. Modal analysis was then used to calculate the pair of front and rear AB stiffness values that yielded the corresponding natural frequencies of the system. These, together with additional model parameters are summarized in Table 2.1.

2.1.1.3: Identification of Contact Criterion

TFC TD experiments were used to investigate the onset of contact and its definition as used in the rough surface contact model. Contact herein is defined as occurring when the separation h (measured from the mean of asperity heights of the two rough surfaces) is smaller than $n\times\sigma$, where n is determined from the TD experiments, and is typically less than 3 (σ is the equivalent root-mean-square roughness). In earlier models, the value of n was selected to be equal to 3 [19], based on theoretical considerations alone. A $3\times\sigma$ contact criterion represents 0.3% probability of contact (for a normal distribution of asperity heights), which is practically undetectable in a HDI system. The $3\times\sigma$ contact criterion has been reinstated in later models [10, 12].

Based on TD experiments with 11 nm nominally flying sliders, the measured TFC protrusion height at which contact was detected was found to be 9.8 nm. To align the measured onset of contact, with the contact criterion in the dynamic contact model, contact was defined as the value of n in the expression $n\times\sigma$ for which, for a TFC protrusion height of 9.8 nm, a "sudden" increase in normal vibration was detected, while there was no such increase for the previous actuation height of 9.6 nm. A series of dynamic simulations was performed for a fixed h_{TFC} value of 9.8 nm with n values ranging from 0 to 2.8. In the model, contact was identified when the separation becomes less than the contact criterion, i.e. when $h < n\times\sigma$. Based on these results, it was found that the contact criterion is equal to $1.2\times\sigma$. This means that, for a TFC protrusion height of 9.8 nm and a combined σ = 0.869 nm, contact first occurs when the separation becomes less than 1.043 nm, while at the previous actuation height of 9.6 nm there is no contact. A way of interpreting this contact criterion is to say that there is a 100% - 67.2% = 32.8% probability of contact (or that 32.8% of asperities experience contact, for a normally distributed roughness). This value of the contact criterion was adopted for the remainder of the simulations where h_{TFC} was varied from 0 to 15 nm.

2.1.1.4: TFC Nominal Area of Contact

Using the established contact criterion, the nominal area of contact was calculated based on the exact TFC geometry and pitch of the AB. The instantaneous lowest point of the TFC ellipsoid can come as close as $(3 - 1.2)\times\sigma = 1.8\times\sigma$ = 1.564 nm to the combined rough surface for contact to be initiated. Therefore, the nominal area at the moment of inception of contact can be calculated by hypothetically sectioning the ellipsoid volume with a horizontal plane located at 1.564 nm upward from the lowest point on the ellipsoid. To this end, the TFC ellipsoid geometry is characterized relative to the middle of the TE (a fixed point) using analytical equations. The cutting plane is also described analytically and the system of equations is solved to yield the coordinates of the nominal area of the ellipse in the three-dimensional space. Knowing these coordinates allows for the calculation of its area, while the only variable in the system is the TFC protrusion height h_{TFC}. For example, at TFC pole protrusion heights of 5, 10, and 15 nm, the corresponding protrusion curvatures and nominal contact areas are 1506, 827, 567 μm and 124, 68, 47 μm^2, respectively.

2.1.2: Experimental Measurements

All measurements were performed at mid-diameter of a 3.5-inch disk (MD = 34.25 mm). Both the dynamic microwaviness (DMW) and TD identification (contact criterion) measurements used a nominal disk speed of 5,425 RPM.

2.1.2.1: Dynamic Microwaviness

DMW is what the flying slider (in this case the TFC protrusion) will experience as a dynamic input from the rotating disk. The content of such signal includes low wavelength disk topography (waviness) and possibly system dynamics and is measured using non-contact vibration methods such as a Laser Doppler Vibrometer (LDV). An LDV (Polytec) with a laser spot size of 15 μm diameter was used to measure the disk profile as the disk was rotated at 5,425 RPM while the laser remained stationary above the disk at the MD. The velocity decoder of the LDV was set at 25 mm s^{-1}/V sensitivity and the output signal was high- passed filtered at 10 kHz, corresponding to spatial wavelengths of 1.95 mm. The highest frequency content of the DMW was 500 kHz, corresponding to spatial wavelengths of 39 μm. Precise triggering was accomplished using a separate laser nanosensor and the data were recorded at 4 MS/s over a distance of 78.55 mm. The signal was then averaged 100 times and was then integrated to obtain the displacement. The standard deviation of the measured DMW is 0.918 nm. The larger than expected amplitude is because of the 10 kHz cutoff, which allows higher amplitude larger spatial wavelengths "perfectly" tracked by the TFC protrusion. One could use a higher high-pass filter of 20 kHz without affecting the results.

2.1.2.2: Roughness Parameters

An AFM was used to measure the roughness of the disk. The scan size was 10×10 μm^2 with 512×512 points at a scan rate of 1 Hz. The roughness data were digitized and exported for extraction of the statistical parameters (root-mean-square roughness σ, average radius of curvature of asperities R, areal density of asperities η, and distribution of asperity heights). Table 2.2 lists the disk and TFC bulge extracted parameters as well as the combined or equivalent parameters.

2.1.2.3: TD Identification

Flyability measurements were performed using the same disk location and speed as the DMW measurements. A special pattern was written on a data track of the disk and the signal amplitude was measured for sequential actuation steps until TD was detected [1]. The actuation resolution was equal to 0.20 nm. TD was identified using the self-diagnosing (burn-in) mode process of the HDD at the actuation step where a sudden increase of normal vibration was detected. The signal amplitudes were then converted to head media spacing (HMS = clearance – t) values using the procedure in [1]. Using the results of the TD experiments, it was possible to calculate the difference in HMS values between zero actuation and TD. This difference, which is set equal to the TFC protrusion height, by definition includes any thermal or other effects from the TFC actuation.

2.1.3: Results and Discussion

Simulations were performed for a range of TFC protrusion heights between 0 and 15 nm. The dynamic results – clearance time histories, interfacial forces, contact pressure and shear stress – are first presented and then averaged over the steady state range and plotted against the TFC protrusion height. Time histories of the clearance for flying (TFC protrusion height of 9.6 nm) and steady, light contact (TFC protrusion height of 11 nm) operating conditions are presented in Figure 2.3. In the rough surface interacting model considered in this work, clearance is defined as the distance between the instantaneous lowest point of the TFC protrusion and the disk surface. From the previous definition of contact, i.e. $h < n\times\sigma$ for contact to occur, the clearance can be obtained as $h – n\times\sigma$ where h is the separation equal to the difference between the instantaneous values of the slider displacement z_t and the DMW z_{dt}, while $n\times\sigma$ is equal to 1.043 nm; hence, contact exists when clearance is negative (onset of contact is at zero clearance). The magnitude of the negative clearance during contact is termed interference. As seen in Figure 2.3(a), no contact is encountered; however, there is significant FHM, whereas Figure 2.3(b) shows sliding light contact without significant bouncing vibrations (BVs). The average interference is 0.6 nm, corresponding to lubricant contact only, i.e., surfing recording.

As the model can predict stable light contact, which has also been observed experimentally using

TFC technology [51], next we investigate the interfacial forces corresponding to these conditions. The contact, friction and net interfacial forces – time histories for mild, steady contact operating regime (Figure 2.3(b)) – are depicted in Figure 2.4, while the corresponding friction coefficient (friction force divided by the net normal force), mean contact pressure (net normal force divided by the real area of contact) and shear stress (friction force divided by the real area of contact) time histories, all of which are calculated form the dynamic interfacial forces, are shown in Figure 2.5. The instantaneous contact force, Figure 2.4(a), has an average value of about 1 mN, while the friction force is slightly higher, thus resulting in an average friction coefficient of about 1.2, Figure 2.5(a). It should be emphasized that this is a calculated friction coefficient based on the contacting/sliding asperities and the generated stresses and there is no pre-assumed value.

The net interfacial normal force, Figure 2.4(c) includes the contact, damping and adhesive forces and its average negative value indicate a net attractive force due to adhesion. The mean contact pressure and average shear stress at the sliding interface is of the order of 400 MPa, which is significantly lower than the values predicted for sliders without TFC technology [8]. The main reason for the lower values is that the interacting nominal and real areas of contact are lower. Specifically at 11 nm TFC actuation, the nominal contact area is 62 μm^2 and the real area of contact is only 2.7 μm^2 (4.3%).

2.1.3.1: FHM and BVs

The instantaneous dynamic separation can be used to calculate the FHM, while the slider is flying, or BV, during contact at the TFC protrusion from

$$FHM\,(\%) \text{ or } BV\,(\%) = \frac{\max(FH) - \min(FH)}{\text{Nominal } FH} \tag{2.1}$$

It is perceived that FHM should be limited to less than 10% for stable flying and reliable recording performance. Figure 2.6 depicts the FHM and BV versus TFC protrusion height. This plot was obtained from multiple time-varying displacement histories over the whole range of 15 nm TFC actuation.

At a TFC protrusion height of 4–7 nm (corresponding to clearances of 5.8 to 2.8 nm) the FHM is about 12.5% and subsequently it decreases for lower clearances until initial TD at 9.8 nm of TFC actuation (Figure 2.6). Within the next 5 actuation steps (TFC height of 9.8 to 10.8 nm) significant BVs occur exceeding 20% until stable mild contact is established for a TFC protrusion height of 11 nm (which corresponds to 0.58 nm interference, thus being in the bonded lubricant regime that is 0.75 nm thick). These simulation results correlate extremely well with the experimental measurements reported in [51], which discern three distinct regimes of the slider's flying behavior: "steady flying with adequate clearance, bouncing motion following the onset of head-disk contact, and steady sliding in the interference regime."

Based on these results, two possible *optimum* operating points could be identified: the first would be at 9 nm TFC protrusion height (0.8 nm prior to TD) where the FHM is 9% while the average clearance is 2.4 nm; the second would be at 11 nm TFC protrusion height (1.2 nm after TD), where the BV is less than 2% and the interference is 0.6 nm (Figure 2.3(b)). The two operating conditions correspond to the in-flight and in-contact recording regimes discussed by Liu *et al.* [18]. The first optimum operating point corresponding to 0.8 nm of clearance may be sufficient for Tbit/in^2 recording however FHM is significant and may be unacceptable. Such an operating point could be reached by actuating the TFC until the first significant vibrations due to TD are detected and then retracting the TFC by less than 1 nm to obtain stable flying with reduced FHM. In contrast, the viability of operating at 0.6 nm interference and less than 2% BV, which could potentially yield even greater recording densities, depends on the contact severity and thus possible wear. Next, the dynamic interfacial forces and stresses are analyzed to investigate contact severity.

2.1.3.2: Mean Contact Pressure and Shear Stress

As discussed above, at a TFC actuation height of 11 nm there is mild, steady sliding contact. The interference of 0.58 nm is similar to what reported by Yu *et al.* [4] who, using a single DOF HDI model with a potential energy-based formulation, reported that surfing recording, i.e. slider-lubricant contact as detailed by Liu *et al.* [18], corresponds to a stable equilibrium interference of 0.78 nm.

To gain insight on wear, the shear stress is calculated from the dynamic interfacial forces as the ratio of Q/A_r. Figure 2.7 presents the trend of the shear stress relative to TFC actuation height during contact, which increases with TFC actuation past TD. The same trends are exhibited by the mean contact pressure as well as the dynamic contact and friction forces, while the real area of contact remains roughly equal to 2.72 μm^2 once mild contact is established and maintained.

The average mean pressure P_m = 359 MPa (and the Hertz maximum contact pressure is $P_0 = 1.5P_m \approx 540$ MPa) while the shear stress τ = 438 MPa, which is significantly lower than the bulk DLC shear strength of 7 GPa. Therefore, with these values, which are smaller than those predicted by Suh *et al.* [47], it is safe to assume that, while the lubricant is displaced during mild contact, there is not expected significant wear of the DLC layer. This is also confirmed by the plasticity index (defined as the ratio of reduced Young's modulus to Hardness times the square root of σ/R) which is 0.52 (purely elastic contact). The clearance, FHM/BV, P_m and τ values are summarized in Table 2.3 for near contact to mild contact or surfing recording conditions.

2.2: IMPROVED TWO-DOF MODEL WITH RIGOROUS DEFINITION OF CONTACT

The nominal FH is maintained at the HDI by imposing – through design – equilibrium between an applied preload and an AB force that is generated through the movement of air under the slider's AB surface. In actuality, it is the disk surface that moves under the slider, which is in turn mounted on the head-gimbal assembly (HGA) as shown in Figure 2.8(a) and (b) and can be pivoted to access any point on the disk surface. The read/write recording elements are located near the TE of the slider, shown in Figure 2.8(c), and their location can be identified by the presence of the protective shields shown in Figure 2.8(d). To increase the recording density, the spacing between the read/write elements and the magnetic layer, termed magnetic spacing, must be reduced to 6.5 nm for 1 Tbit/in^2 recording densities [52]. With protective DLC overcoats on both the disk and slider surfaces, an MTL layer on the disk surface, and the presence of roughness, the corresponding physical head-media spacing (HMS) between the slider and the disk surface needs to be only a couple of nanometers. However, bringing the entire slider surface closer to the disk induces vibrations that could lead to catastrophic slider crashes [53]. Alternatively, TFC nanotechnology works by thermo-mechanically actuating a small volume around the read/write elements of the slider, as shown in Figure 2.8(e), to bring them closer to the rotating disk surface while allowing the slider body to fly steadily at a nominal FH of ~10 nm, thus avoiding significant FHM that would be induced by the increase in adhesive forces if FH was reduced to below 5 nm. In this manner the magnetic spacing can be reduced to below the target value of 6.5 nm without compromising system stability.

2.2.1: Dynamic contact model with friction

An accurate geometric model of the TFC bulge is necessary because, unlike the case of modeling conventional sliders, e.g. [19, 53], contact in sliders featuring TFC technology will occur on the TFC bulge rather than on the TE. It should be noted that under impulsive loading conditions, contact could occur at the corners rather than at the TFC bulge, in which case a 3-DOF model (vertical, pitch and roll motions) needs to be considered. Such operational shock impulse loading/conditions (focusing on the impact mechanics) have been recently studied, e.g., [54-56]. However, the focus of this work is on the contact at the TFC bulge for which a 2-DOF model is sufficient. In this 2-DOF system (vertical and pitch motions), there will be a different POC

(POC) for every value of the pitch angle, i.e. the POC will vary dynamically. To calculate this, parametric equations that describe the TFC bulge geometry are solved to yield the instantaneous lowest point where contact will occur. The location of the POC will also change the magnitude of the moment arm that will affect the dynamic contact and friction moments acting on the slider.

2.2.1.1: TFC Bulge Geometry

The TFC bulge can be effectively modeled as an ellipsoid as shown in Figure 2.9. It is necessary to either measure TFC during actuation experimentally or, as was done in this work, to use finite element simulations solving the heat transfer equations to extract a precise deformed profile of the slider at the location of the TFC bulge. For details on the interactions between the aerodynamic, thermal and structural fields that can be used to predict the TFC bulge profile refer to Zhou *et al.* [57]. In the plane of symmetry used in the 2-DOF model (*xz*-plane) the TFC bulge can be described as an ellipse having a semi-major axis of length a_{TFC} and a semi-minor axis of length h_{TFC}, where a_{TFC} is termed the semi-width and h_{TFC} is the overall height of the protrusion, also referred to as TFC actuation amplitude or TFC actuation for short. The center of the TE of the slider is used as a fixed point of reference for the TFC bulge configuration and the center of the TFC ellipsoid is offset from the TE by a distance x_{TFC}. The profile in the direction along the TE (*yz*-plane) is again that of an ellipse whose semi-major axis is equal to w_{TFC}. The designation of semi-major and semi-minor axes may not be apparent because Figure 2.9 is drawn using a skewed aspect ratio. Note that the TFC bulge height is of the order of a few nanometers while a_{TFC} and w_{TFC} as well as x_{TFC} are of the order of micrometers.

Parametric equations are used to describe any point on the surface of the ellipsoid as a function of two angles α and β and with the center of the TE as the origin:

$$\begin{Bmatrix} x \\ y \\ z \end{Bmatrix} = \begin{Bmatrix} x_{TFC} + a_{TFC} \cos\alpha \sin\beta \\ \frac{1}{2} w_{TFC} \sin\alpha \sin\beta \\ h_{TFC} \cos\beta \end{Bmatrix} \tag{2.2}$$

The angles α and β are defined within the intervals $[0, \pi]$ and $[\pi/2, 3\pi/2]$ respectively. In the 2-DOF model, the pitch of the slider, i.e. the angle formed between a plane running along the ABS

and the horizontal, henceforth referred to as the pitch angle θ, needs to be accounted for. This can be done using a rotation matrix multiplied from the left with the parametric equations to yield the transformed equations

$$\begin{Bmatrix} x' \\ y' \\ z' \end{Bmatrix} = \begin{bmatrix} \cos\theta & 0 & -\sin\theta \\ 0 & 1 & 0 \\ \sin\theta & 0 & \cos\theta \end{bmatrix} \begin{Bmatrix} x \\ y \\ z \end{Bmatrix} = \begin{bmatrix} \cos\theta & 0 & -\sin\theta \\ 0 & 1 & 0 \\ \sin\theta & 0 & \cos\theta \end{bmatrix} \begin{Bmatrix} x_{TFC} + \mathrm{a}_{TFC}\cos\alpha\sin\beta \\ \frac{1}{2} w_{TFC}\sin\alpha\sin\beta \\ h_{TFC}\cos\beta \end{Bmatrix}$$
$$\Rightarrow \begin{Bmatrix} x' \\ y' \\ z' \end{Bmatrix} = \begin{Bmatrix} \left(x_{TFC} + \mathrm{a}_{TFC}\cos\alpha\sin\beta\right)\cos\theta - \left(h_{TFC}\cos\beta\right)\sin\theta \\ \frac{1}{2} w_{TFC}\sin\alpha\sin\beta \\ \left(x_{TFC} + \mathrm{a}_{TFC}\cos\alpha\sin\beta\right)\sin\theta + \left(h_{TFC}\cos\beta\right)\cos\theta \end{Bmatrix} \quad (2.3)$$

Both DOF can thus be accounted for by translating the origin (TE) along the *z*-axis for normal motion and/or imposing a rotation by an angle θ corresponding to the pitch motion. It is now possible to extract the coordinates of the instantaneous lowest point of the TFC bulge where contact will occur, i.e. the POC, by minimizing these parametric equations as follows:

$$\begin{Bmatrix} x \\ y \\ z \end{Bmatrix}_{POC} = \min \begin{Bmatrix} \left(x_{TFC} + \mathrm{a}_{TFC}\cos\alpha\sin\beta\right)\cos\theta - \left(h_{TFC}\cos\beta\right)\sin\theta \\ \frac{1}{2} w_{TFC}\sin\alpha\sin\beta \\ \left(x_{TFC} + \mathrm{a}_{TFC}\cos\alpha\sin\beta\right)\sin\theta + \left(h_{TFC}\cos\beta\right)\cos\theta \end{Bmatrix}_{\alpha\in[0,\pi],\beta\in[\pi/2,3\pi/2]} \quad (2.4)$$

2.2.1.2: Dynamic Contact Model Formulation

The 2-DOF dynamic contact model of the HDI is presented next, which is based on Lee and Polycarpou [19]. The dynamic model has three characteristic states: i) the slider is flying over the disk with the aid of the AB force and with the adhesive force acting on the TFC bulge as shown in Figure 2.2(a); ii) the TFC bulge is contacting the disk at the POC, where, in addition to the AB and adhesive forces, contact and friction forces are also activated as shown in Figure 2.2(b); and, iii) the slider is flying with negligible adhesive and AB forces (applicable for FH > 15 nm; not shown).

The slider has mass m and moment of inertia *J*, and is described by its dimensions of length *l* and thickness l_t as shown in Figure 2.2. The TFC bulge is located at a distance x_{TFC} away from the

TE and has an actuation height h_{TFC} as discussed previously; note that the mass and volume of the TFC bulge are too small to influence the inertia of the slider. A preload F is applied to the slider while its attachment to the HGA is modeled through the linear stiffness and damping coefficients k and c along with the angular stiffness and damping coefficients k_θ and c_θ respectively. Initially, the slider is positioned at a pitch angle θ_0 and equilibrium with the preload is achieved through the initial AB force and moment F_{ai} and M_{ai}. The AB force is lumped into a rear and front component by using the corresponding stiffness and damping coefficient values of k_r, k_f, c_r and c_f. The rear and front AB forces are assumed to be acting on the TE and LE of the slider respectively. Contact is modeled at the POC through a highly non-linear stiffness k_c, calculated from the contact model as the ratio of the differential static contact force dP to the differential separation dh, and a constant damping coefficient c_c, which can be used to calculate the dynamic contact force F_c. The friction and adhesive forces Q and F_s are also acting on the POC and, along with F_c produce moments about the slider's COM.

Let us introduce a vector with magnitude equal to the distance between the slider's COM and POC, which is defined based on the TFC geometry and the instantaneous vertical location and pitch angle of the slider as shown in Figure 2.1:

$$\boldsymbol{r}_{COM\to POC} = -\left|\left(\boldsymbol{r}_{COM\to POC}\right)_x\right|\boldsymbol{i} - \left|\left(\boldsymbol{r}_{COM\to POC}\right)_z\right|\boldsymbol{k} \tag{2.5}$$

The unit vectors i and k correspond to the x and z directions respectively as these are drawn in Figure 2.9, while the magnitudes of the x and z-components defining this vector for a slider of length l and thickness l_t are

$$\left|\left(\boldsymbol{r}_{COM\to POC}\right)_x\right| = \left|\left(\tfrac{1}{2} l\cos\theta - \tfrac{1}{2} l_t \sin\theta\right)\right| - \left|x_{POC}\right| \tag{2.6}$$

$$\left|\left(\boldsymbol{r}_{COM\to POC}\right)_z\right| = \left|\left(\tfrac{1}{2} l\sin\theta + \tfrac{1}{2} l_t \cos\theta\right)\right| + \left|z_{POC}\right| \tag{2.7}$$

The instantaneous location of the POC relative to the origin at the TE (x_{POC}, z_{POC}) can thus be extracted from equation (2.4).

Figure 2.1 also shows the displacements used in the model, all of which are defined relative to the mean of surface heights of the rough surface. The interface between the two rough surfaces of the TFC bulge and the disk is modeled using the GW model [58] as an equivalent interface between a rigid smooth flat and a compliant rough nominally flat surface. The radius of curvature of the TFC bulge is of the order of millimeters and, given the nanoscale dimensions of the contact patch, can be safely approximated as nominally flat; hence, the GW model is applicable. The rough surface, then, will have a composite roughness profile based on the RMS roughness σ_i, mean radius of curvature of asperities R_i, and areal density of asperities η_i for each surface. The quantities σ, R and η denote the combined roughness parameters. For a Gaussian distribution of the asperity heights, statistically, 99.7% of the asperities of the equivalent rough surface will be within $\pm 3\times\sigma$ from the mean.

Since we make use of experimentally measured topographical roughness and DMW data in the model, it is meaningful to use the mean of surface heights, rather than the mean of asperity heights, as a reference for the equivalent rough surface. The distinction between the two is that, while the mean of surface heights is calculated by averaging the height of every discrete point on the surface, as is experimentally done with AFM measurements, thus capturing both peaks and valleys, the mean of asperity heights would require that an asperity on the surface is first defined as such and then the mean would be the average of the heights of each asperity. DMW is a combination, primarily of topographical roughness measured dynamically confounded with secondary effects such as spindle motor vibrations, and is used as a time-varying input to the model. DMW is accounted for by superimposing it with the roughness such that at each instant in time the mean of surface heights is translated vertically following the DMW profile – hence the reference to an instantaneous mean in the caption of Figure 2.1 – described by the time-varying displacement z_{dr}, while the roughness is captured statistically within a range of $3\times\sigma$ from that mean as shown in Figure 2.2.

As an initial condition, the displacement at the TE z_r is set equal to the nominal FH. It should be noted that the value of the nominal FH is taken to be constant (11 nm) to coincide with previously measured flyability experiments performed at a radius of 35 mm (MD) at 7,200 rpm [1, 11]. After solving the equations of motion for the initial conditions, the resulting

displacement of the COM z_G and the pitch angle θ (the two DOFs) are used to recalculate all other displacements and the new POC using slider geometry. The equations of motion of the slider are shown below in matrix form:

$$\boldsymbol{M}\ddot{\boldsymbol{s}} + \boldsymbol{C}\dot{\boldsymbol{s}} + \boldsymbol{K}\boldsymbol{s} = \boldsymbol{f_i} + \boldsymbol{f_a} + \boldsymbol{f_c} + \boldsymbol{f_s} \tag{2.8}$$

The vector $\boldsymbol{s}$ contains the two DOFs of vertical displacement and pitch angle, i.e. $\boldsymbol{s} = \{z_G, \theta\}^T$ while the mass, damping and stiffness matrices are

$$\boldsymbol{M} = \begin{bmatrix} m & 0 \\ 0 & J \end{bmatrix} \tag{2.9}$$

$$\boldsymbol{C} = \begin{bmatrix} c + c_f + c_r & lc_f - lc_r \\ lc_f - lc_r & l^2 c_f + l^2 c_r + c_\theta \end{bmatrix} \tag{2.10}$$

$$\boldsymbol{K} = \begin{bmatrix} k + k_f & lk_f \\ lk_f & l^2 k_f + k_\theta \end{bmatrix} \tag{2.11}$$

and the forcing terms are

$$\boldsymbol{f_i} = \begin{Bmatrix} -F + F_{ai} \\ M_{ai} \end{Bmatrix} \tag{2.12}$$

$$\boldsymbol{f_a} = \boldsymbol{f_{af}} + \boldsymbol{f_{ar}} = \begin{Bmatrix} k_f z_{df} + c_f \dot{z}_{df} \\ lk_f z_{df} + lc_f \dot{z}_{df} \end{Bmatrix} + \begin{Bmatrix} c_r \dot{z}_{dr} + F_{ar} \\ -lc_r \dot{z}_{dr} - lF_{ar} \end{Bmatrix} \tag{2.13}$$

$$\boldsymbol{f_c} = \begin{Bmatrix} F_c \\ -\left|\left(\vec{r}_{COM \to POC}\right)_x\right| F_c - \left|\left(\vec{r}_{COM \to POC}\right)_z\right| Q \end{Bmatrix} \tag{2.14}$$

$$\boldsymbol{f_s} = \begin{Bmatrix} -F_s \\ \left| \left(\vec{r}_{COM \to POC} \right)_x \right| F_s \end{Bmatrix} \tag{2.15}$$

corresponding to the preload and initial AB shown in equations (2.12), dynamically changing AB in (2.13), contact in (2.14), and adhesive contributions in (2.15).

The FH and the corresponding adhesion and contact separations are time varying quantities defined relative to the mean of surface heights with respect to three distinct layers of the disk morphology: solid (DLC), bonded lubricant, and mobile lubricant layers. As shown in Figure 2.10, with z_t and z_{dt} being the time varying TFC bulge displacement and disk DMW at the POC respectively, we can define FH as the time varying difference between the two, i.e. $FH(t) = z_t(t) - z_{dt}(t)$. Both displacements and the FH are defined relative to the bonded lubricant surface because this is the surface one would probe in AFM measurements of the topography, since the mobile lubricant layer is readily displaced with contact. Adhesion is calculated from the surface energy $\Delta\gamma$ of the lubricant and is therefore defined relative to the mobile lubricant layer. Conversely, because with the current contact model we assume that the lubricant is displaced and offers no resistance to the motion of the TFC bulge, contact is defined relative to the solid (DLC) layer. As stated previously, the bonded lubricant layer behaves as a semi-solid [17] and, hence, should be included in the future formulation of an improved contact model. The adhesion and contact separations can be defined relative to the FH as $FH - T_0$ and $FH + T_0$ respectively, where T_0 is the bonded lubricant thickness equal to half the total thickness t [19, 53]. Note that the adhesive force is maximized when the distance between the TFC bulge and the mobile lubricant surface becomes smaller than the equilibrium spacing ε, taken in this work as 0.098 nm [45, 59].

Since contact is statistically defined as the case when the approaching surface comes within $3\times\sigma$ from the mean of surface heights of the solid (DLC) layer, it follows that clearance is equal to the quantity $FH + T_0 - 3\times\sigma$ as shown schematically in Figure 2.10. When the clearance becomes negative then it is termed interference and designates solid contact. Note that in this work clearance is defined between the slider surface (assumed to be a smooth plane) and the top of the solid (DLC) surface. Alternatively one could define clearance to coincide with HMS, i.e., to be the physical spacing between the slider surface and the top of the lubricant layer. However with

the involvement of detectable slider/disk contact the choice of solid (DLC) contact is justified.

The dynamic contact force is zero during flying but takes the following form during solid contact, i.e. when $z_{dt} < z_t < 3\times\sigma$:

$$F_c = k_c\left(z_t - z_{dt}\right) - c_c\left(\dot{z}_t - \dot{z}_{dt}\right) \tag{2.16}$$

Based on the contact model, all the interfacial forces, namely the quasi-static contact force $P(h)$, the friction force $Q(h)$, and the adhesive force $F_s(h)$, are calculated as functions of the separation h, which is equal to the distance between the nominally flat surface and the mean of surface heights of the rough surface (refer, for example, to Figure 2.11 for a plot showing this relation for the contact and adhesive forces). Note that h and FH are quasi-static and dynamic (i.e. where the mean of surface heights moves with the DMW) measures of the same distance, respectively. The nonlinear contact stiffness k_c can be extracted from the quasi-static contact force $P(h)$ as the ratio of the change in $P(h)$ over the change in separation. Since P and Q are both functions of h, they can also be plotted as functions of each other; hence, the maximum friction force is extracted as a function of F_c by equating the quasi-static and dynamic contact forces, i.e. $P = F_c$. To obtain the interfacial forces from the contact model, the quasi-static separation h is set equal to the dynamically changing quantity FH + T_0 for the contact stiffness and FH – T_0 for adhesion.

The complex nature of a slider AB is best described by three DOFs, i.e. vertical, pitch and roll motions, through a generalized Reynolds pressure field equation beneath the ABS. ABS design, e.g. as discussed in [60], aims to produce an AB force that will allow nominal flying of the slider at the desired FH under a given preload. It has been shown [19, 25] that the 2-DOF model adopted in this work is adequate for capturing the dynamic AB behavior. In the present model, it is assumed that the slider maintains the same FH, equal to the nominal value of 11 nanometers, throughout the actuation of the TFC protrusion. This simplifying assumption allows for the use of a constant nominal rear AB stiffness $k_{r,nom}$, which can be calculated from the natural frequencies of the AB. A summary of the dynamic contact model parameters is shown in Table 2.1.

An improvement of the current model over the one presented in Vakis *et al.* [11] is that the rear AB force is modeled as a stiffening spring force with respect to the amount of TFC actuation. Specifically, the rear AB stiffness, k_r is calculated as the sum of the nominal value and an increase in stiffness relative to TFC actuation as per the work of Zheng and Bogy [7]. In their work, the AB pressure and spacing were obtained by solving the generalized Reynolds equation; the deformation of the ABS was obtained through a coupled-field analysis (electrical-thermal-structural) using finite elements analysis, while the AB cooling effects were also included through a heat transfer model [7] . While the analysis of the AB dynamics to the thermal effects of the slider is important [18, 50, 57], the approach adopted in this work, which allows for the lumping together of these factors into an effective increase in the AB stiffness, is deemed sufficient for the purpose of this model. Zheng and Bogy report a similar increase in stiffness at an elevation of 4 km, where the air density would be different than that at sea level. This added variability, which would alter the flyability and optimization results and would make implementation of the optimized design more challenging, could be readily added to the model but the authors chose to give their analysis a more simplified, general outlook.

Material properties for the currently used sliders and disks are summarized in Table 2.4 [11]. Both the TFC bulge and the disk are coated with DLC, hence the Young's modulus, Poisson's ratio and hardness values used correspond to DLC properties. However, since adhesion is defined relative to the lubricant layer, the surface adhesion energy of the lubricant is used in the model. The roughness parameters were extracted from AFM measurements of the TFC bulge and disk surfaces. The interfacial dynamic contact model with friction, which is used to calculate the adhesive, contact and friction forces as well as the real area of contact using roughness, material and lubricant properties was presented elsewhere, e.g. [19, 53], and is summarized in Appendix A.

2.2.1.3: Calculation of the Nominal Area of Contact

Contact is defined in a statistical sense as the case when the displacement of the rigid flat comes within a distance of $3\times\sigma$ from the dynamically moving mean of surface heights. The quantity σ is the combined topographical roughness that is equal to 0.495 nm for the case examined in this work (Table 2.4). This corresponds to the case when the clearance becomes negative. Then, TD

is defined as the actuation where solid contact is first identified. Note that due to this definition, TD could correspond to extremely light solid contact, which may not be experimentally detectable. For example, for 9.8 nm of actuation, contact occurs for less than 1% of the number of iterations, i.e. the clearance becomes negative for less than 1% of the simulation time. This is discussed further in the Results and Discussions section.

The abovementioned criterion for contact can be verified using simulation results of the ISBL contact model for the quasi-static contact force as a function of dimensionless separation, h^*. As seen in Figure 2.11(a), the quasi-static contact force P is 7.30 μN at $h^* = h/\sigma = 3$. Referring to Figure 2.11(b), we can assume that, since this value is only 3% of the value of P at $h^* = 2.5$, a force below 10 μN is negligible for the purposes of our model. Hence, we can define the contact criterion as $3\times\sigma$. The same can be applied to the adhesive force F_s shown in Figure 2.11(c), which is negligible at $h^* = 6$ and beyond, meaning that the effect of adhesion is significant only within a distance of $6\times\sigma$ from the mean of surface heights. Since the TFC bulge can approach the disk surface as much as $3\times\sigma$ from the mean of surface heights before contact is detected, then we can calculate a nominal area of contact, A_n, by truncating the TFC bulge at a height of $6\times\sigma - 3\times\sigma = 3\times\sigma = 1.485$ nm and using the projected area $A_n = \pi d_1 d_2$ where d_1 and d_2 are the semi-major and semi-minor axes of the resulting ellipse as shown in Figure 2.12.

The calculated nominal area values are favorably compared to simple elastic Hertzian contact patch areas. For example, at a TFC actuation of 12 nm corresponding to steady mild contact, the nominal area calculated by truncating the ellipsoid as described above is 55 μm^2. After performing the dynamic simulations, we can extract the steady-state value of the dynamic contact force at this actuation to be 1.63 mN and, using a Hertzian sphere formulation, i.e. utilizing a composite radius of curvature (1.37 mm) calculated from the radii of curvature of the ellipsoid in the *xz* and *yz* planes, we can calculate a Hertzian contact patch semi-width of 2.26 μm. From the results of Greenwood and Tripp [61] for rough spherical contacts, the rough sphere contact patch semi-width can be 1-3 times that of the smooth Hertzian case, thus yielding a range for the nominal area of contact between 16 and 144 μm^2. The calculated value of 55 μm^2 is within this range and, in fact, closer to the Hertzian solution (16 μm^2), which would be expected given the extremely smooth nature of the surfaces.

2.2.2: Results and Discussion

2.2.2.1: Dynamic Contact Results

A value of TFC actuation is selected for which the 2-DOF dynamic contact model with friction is used to generate time varying results of slider displacement and pitch, interfacial forces and real area of contact. As described previously, the nominal area of contact is calculated by truncating the TFC ellipsoid resulting from the given value of actuation at a distance of $3\times\sigma$ from its lowest point, and it is then used to dimensionalize the contact model output. The switching, non-linear system of ordinary differential equations presented in equations (2.8) to (2.15) is solved to yield the time varying dynamic results. The results for TFC actuation of 12 nm corresponding to steady-state solid contact are plotted as time histories and are shown below in Figure 2.13.

Figure 2.13 shows simulation results of the clearance and dynamic contact and friction forces versus time for a TFC actuation of 12 nm. The average steady-state value for the clearance is -0.34 nm as shown in Figure 2.13(a). This negative value, which corresponds to an interference of 0.34 nm, means that the TFC bulge is steadily contacting the solid (DLC) layer with an average penetration equal to the value of the interference. Correspondingly, the dynamic contact and maximum friction forces, shown in Figure 2.13(b) and (c), have average steady-state values of 1.63 mN and 2.43 mN respectively. Since $Q > F_c$, friction dominates the interface and the resulting coefficient of friction will have an average steady-state value larger than one as shown in Figure 2.14(a). The real mean pressure, $P_m = F_c/A_r$, and shear traction, $\tau = Q/A_r$, are also plotted versus time in Figure 2.14(b) and (c). Note that the real area of contact A_r is extracted from the ISBL model and is only a few percent of the nominal contact area. For the actuation of 12 nm examined here, the average steady-state value of A_r is 0.36 μm^2. Given that the combined areal density of asperities for the interface is 124 μm^{-2} (Table 2.4), 45 asperities are in contact. Hence, the resulting real mean pressure and shear stress values are quite large.

In the absence of an impulse excitation, the only input to the system is the DMW and through it, implicitly and in a dynamic manner, the roughness of the interface. This input causes the system to oscillate and the amount of vibration, which can be quantified as FHM during flight or BVs during contact, is determined by the instantaneous separation between the slider and disk

surfaces; it is, therefore, primarily dependent on the magnitude of the adhesion force, which for an actuation of 12 nm has an average steady-state value of 0.98 mN. Hence, for clearances larger than $6\times\sigma$, where adhesion becomes negligible, the preload and AB forces balance out and the slider flies with small FHM. Similarly, during solid contact, the adhesion force is maximized and acts to dampen the vibrations of the system, which together with the contact force result in even smaller BV amplitudes. The effect of adhesion is most detrimental during the transition from flying to contact where it may induce severe vibrations.

Treating the time histories of each actuation step as statistical quantities, steady-state mean values and standard deviations can be extracted for each actuation step. For example, the FH at 12 nm of actuation can be expressed as 0.34 ± 0.018 nm. This allows for the plotting of any quantity as a function of TFC actuation as shown in Figure 2.15. Figure 2.16 depicts the clearance (= FH + T_0 – $3\times\sigma$) as a function of TFC actuation. When clearance becomes negative, then it means that solid (DLC) contact occurs. TD is shown in the figure to occur at 9.7 nm of actuation. This is in agreement with the results of the flyability experiments reported in [11], which further supports the definition of TD from the solid (DLC) surface (as compared to a definition from the lubricant surface).

Using the steady-state values of the clearance, one can identify the regime of operation (flying, versus lube contacting versus solid contacting), as a function of actuation as well as the occurrence of TD. Specifically, if the steady-state clearance, which is measured relative to the surface of the solid (DLC), becomes negative then solid contact occurs (dark gray color regime). Hence, in Figure 2.16, the clearance first becomes zero at the boundary between the bonded lubricant (blue or lighter gray color) and the solid contact regimes (10.4 nm of TFC actuation). If the steady-state clearance is larger than zero but smaller than T_0 = 0.75 nm, then operation is within the bonded lubricant layer. If it is larger than T_0 but smaller than $2\times T_0$, then operation is within the mobile lubricant layer (yellow or very light gray color). Finally, if the steady-state clearance is larger than $2\times T_0 = t$ (= total lubricant thickness), then the slider is flying (white color).

It should be noted that the width of each regime in Figure 2.16 does not correspond to a physical dimension but shows, for example, that, on average, for actuations up to 8.5 nm the slider is

flying; between 8.8 and 9.5 nm of TFC actuation, the slider is in the mobile lubricant layer; between 9.5 and 10.4 nm the slider is in the bonded lubricant layer; and, for actuations larger than 10.4 nm the slider is contacting the DLC layer. The various regimes are extracted from the steady-state average values of the clearance. Therefore, TD occurs while the steady-state average clearance of the slider places it in the bonded lubricant layer, i.e. partial contact with the solid layer does occur at 9.7 nm of actuation due to the oscillations of the slider but the steady-state average value of the clearance is 0.49 nm (positive). This is shown in Figure 2.17(a), depicting a plot of the clearance time history for a TFC actuation of 9.7 nm where TD is detected. The corresponding dynamic contact force time history is shown in Figure 2.17(b). This becomes non-zero in the few instances where the clearance becomes negative. Since light contact or "surfing" recording is defined as operation within the lubricant layer then, for the slider design considered this occurs for TFC actuations between 8.8 and 10.4 nm.

It is possible to extract quantitative information from the clearance plot that can help describe the approach, jump-to-contact and contact behaviors of the slider. Understanding and quantifying these behaviors allows for the accurate characterization of the slider design in terms of flyability and contact. A design requirement is that the slider should approach the disk as smoothly as possible while minimizing the jump-to-contact and contact severity. For this, refer to Figure 2.18, which is a close-up of the clearance versus actuation plot for TFC actuations between 7 and 12 nm. Les us define four slopes: the *approach slope* (A); the *TD slope* (B); the *lubricant contact slope* (C); and, the *solid contact slope* (D) as shown in Figure 2.18.

The approach slope (A) is equal to -1.00, which means that, in the absence of sufficient adhesion, there is a one-to-one correspondence between actuation and clearance. Specifically, if the TFC bulge is actuated by 1 nm during flying then the clearance will be reduced by 1 nm while equilibrium is achieved between the preload and AB forces. The jump-to-contact slope (B), however, is dependent on TFC geometry and is a measure of the jump-to-contact behavior of the interface. From Figure 2.18, this slope is found to be equal to -4.35 nm of clearance per nm of actuation. Ideally, the magnitude of this slope should be as close to the approach slope (A) as possible because this would ensure that the slider can get sufficiently close to the disk without any jump-to-contact. A theoretical scenario where the two slopes would be equal, i.e. A = B, is

when adhesion is zero or negligible. It should then be possible to reduce slope B to within ±100% of slope A if the nominal area of contact is sufficiently reduced. An interesting feature is that the slope of lubricant contact (C) is equal to the approach slope (A), meaning that within the lubricant the adhesion is constant and equal to the maximum value and is merely scaled by the decreasing nominal contact area. However, an improved adhesion model should account for the variation of the surface energy with penetration into the lubricant layer. After TD the contact slope is -0.22 nm of clearance per nm of actuation, indicating stiff contact. This slope becomes even smaller with increasing TFC actuation as shown in Figure 2.18.

An important quantity can be defined at the intersection of the approach and jump-to-contact slope lines and indicates the minimum clearance attainable before sudden jump-to-contact. Let us call this the critical point and the relevant actuation critical TFC actuation, $h_{TFC,cr}$. For the default TFC geometric design investigated here $h_{TFC,cr}$ is equal to 8.6 nm. However, this actuation may not necessarily correspond to the optimum point of operation, especially if the magnitude of the vibrations is prohibitively large. As shown in Figure 2.19, at 8.6 nm of actuation where the clearance is equal to 2.39 nm, the FHM, defined as the ratio of the variation in FH over the nominal FH, is equal to 14.01%. During contact this ratio is termed BV. The plot of FHM/BV against TFC actuation plot is shown in Figure 2.19.

To minimize FHM below 10% we would have to operate at smaller actuation of 8.5 nm where the clearance is 2.54 nm and the FHM is 8.20%. This clearance corresponds to an HMS of 2.54 nm – 1.5 nm ≈ 1 nm where 1.5 nm is the total lubricant thickness. Assuming burnishing of the DLC layer on the slider, the minimum DLC layer thickness on the disk surface to avoid corrosion and oxidation can be equal to 2 nm [62]. Since the slider can accurately follow the DMW, only the roughness needs to be accounted for in the budget ($3\times\sigma \approx 1.5$ nm). Then, the resulting magnetic spacing when operating at the suggested optimum TFC actuation of 8.5 nm becomes: 1 nm (HMS) + 1.5 nm (total lubricant thickness) + 2 nm (DLC) + 1.5 nm ($3\times\sigma$) = 6.0 nm, which is within the target magnetic spacing of 6.5 nm for 1 Tbit/in^2 systems. Therefore, it would be theoretically possible to achieve the target of 1 Tbit/in^2 recording densities with flying recording and currently available TFC slider nanotechnology. However, accounting for operating (and manufacturing) tolerances would require that actuations say ±0.5 nm from the critical point,

corresponding to 2-3 actuation steps with currently available actuation resolution, would not result in significantly larger FHM or BV. Practical operation at 8.5 nm, and hence within the target for 1 Tbit/in^2 systems, would become possible only if the spike in FHM at 8.6 nm was eliminated. One way to achieve this is through optimization of the TFC bulge geometry.

When considering light contact or "surfing" recording, it seems that the vibrations present for the current TFC geometric design are prohibitive for operation within the lubricant layer. For example, a possible operating point within the mobile lubricant layer would be at 9.5 nm of actuation where the FHM is 9.29% and the clearance is 0.67 nm. However, the large spike in FHM that occurs at 8.6 nm of actuation would preclude stable operation at actuations larger than 8.5 nm as discussed previously. An improved TFC geometric design would preferably feature reduced FHM up to the point of TD thus enabling light contact or "surfing" recording.

2.2.1.2: Assessment of Contact Severity

The steady-state average mean contact pressure is shown in Figure 2.20(a). At 12 nm TFC actuation, it is equal to 4.47 GPa (compare with the DLC hardness of 13 GPa, Table 2.4). Note that the fluctuations in the mean pressure induced by the BV (between TD and TFC actuation of 11.5 nm) as shown in Figure 2.20(b) can result in maximum pressures that exceed the hardness and could result in yielding.

Figure 2.21(a) shows the steady-state average shear (surface) traction versus TFC actuation. The shear traction at the same actuation of 12 nm is 6.68 GPa, which is larger than the corresponding mean contact pressure. For elastic-plastic contact, the location of maximum shear stress will be below the surface if the coefficient of friction is smaller than 0.3 or on the surface if it is larger than 0.3 [63]. In the HDI, the friction coefficient has steady-state values much larger than 0.3 even for heavy solid contact; for example, the steady-state friction coefficient is 1.49 for 12 nm of actuation as shown in Figure 2.14(a). Hence, the maximum shear stress will occur on the surface. While the steady-state value of the shear traction might be within the limits required to avoid plastic deformation in the DLC layer, the large variation due to vibrations after TD, as shown in Figure 2.21(b), could cause damage to the disk. Specifically, the hardness of DLC is taken to be approximately equal to 1.8 times its yield strength [64], so its yield strength can be

calculated to be 7.2 GPa, which is larger than the maximum shear traction of 6.69 GPa at 12.2 nm of actuation as shown in Figure 2.21(a). Contact severity could be investigated by examining the shear traction variation near-contact and during contact. To quantify this severity with respect to TFC actuation, we examine the percentage of intermittent versus steady solid contact, defined as the percentage of time during which solid contact occurs. This can be calculated as the number of instances where the magnitude of negative clearance, i.e. the interference, becomes smaller than T_0 over the duration of the simulation. This percentage is expected to increase from about zero during TD to 100% during steady solid contact. Figure 2.22 shows the percentage of solid contact with respect to TFC actuation in the vicinity of TD.

Referring to Figure 2.22, at TD (TFC actuation of 9.7 nm) there is only 0.3% of solid contact corresponding to 0.071 μN of steady-state average dynamic contact force, while 100% of solid contact is reached at 11.4 nm and corresponds to 923.72 μN of steady-state average dynamic contact force. One could argue that TD could not be experimentally measured at 9.7 nm based on these extremely light contact conditions (note that 0.2 nm after TD the average steady-state dynamic contact force reaches 1 μN). Examining the shear traction as an indicator of the contact severity, one can observe that the largest variation occurs at 9.8 nm of actuation where the steady-state average shear traction of 3.24 GPa is well within the bulk strength of DLC (7.2 GPa as discussed previously), but, due to the presence of large vibrations, can reach up to 85.21 GPa in magnitude. It should be noted that this is intermittent contact that occurs only 0.82% of the time. It is beyond the scope of this work to analyze the different contact (TD) detection methodologies. However, it would seem that such high shear tractions as those present at 9.8 nm of actuation, albeit intermittent, could be responsible for the experimental detection of TD at 9.8 nm [4]. In addition, contact with the bonded lubricant layer, which appears to behave as a viscoelastic solid at the TD speeds involved, could be detectable.

It was stated previously that light contact or "surfing" recording for this specific slider design would occur for actuations between 8.8 and 10.4 nm. However, based on the above discussion, the functional "surfing" recording regime should be limited between mobile lubricant contact initiation and TD (since solid contact at 9.7 nm is imperceptible) and contact beyond this point should be avoided.

2.3: OPTIMIZATION FOR NEAR-CONTACT RECORDING

The distance between the read/write elements and the disk magnetic layer, termed magnetic clearance, must be reduced to below 6.5 nm for 1 Tbit/in^2 recording densities [52]. When accounting for the thicknesses of the various protective overcoat and lubricant layers, the physical spacing between the slider and disk termed spacing budget becomes even smaller. Contact recording, with the slider physically contacting the protective DLC overcoat of the disk during operation, could yield the minimum attainable clearance. However at present, it is not a viable solution because contacting the DLC overcoat could result in significant wear; furthermore, bringing the entire slider surface closer than few nanometers to the disk could induce dynamic instabilities that could cause catastrophic head crashes [53]. Wear on the disk, through either design or instability-induced head crashes, is undesirable because it could affect the integrity of the magnetic layer and result in loss of data.

Given the small manufacturing and operating tolerances at the HDI, achieving reliable light (lubricant) contact recording would still depend on eliminating the large vibrations that exist at sub-5-nm clearance. Eliminating vibrations, while reducing the clearance through optimization of TFC geometry, requires accurate modeling of the HDI. A dynamic contact model with friction, specific to the TFC geometry was developed by Vakis *et al.* [11], which allows for the calculation of the dynamically changing clearance between the read/write elements and the disk and the interfacial contact, friction and adhesive forces. TFC geometry was used in conjunction with the contact model formulation to identify the limits over which the interface is under the influence of perceptible interfacial forces and, hence, calculate the nominal area of contact which affects both near- and at-contact operation. Experimentally measured dynamic microwaviness, topographical roughness and material properties were used as inputs to the dynamic contact/friction model without any empirical coefficients [11].

The ISBL contact model [19], which uses physics-based formulations for adhesion, contact and friction forces with respect to the separation between an equivalent smooth flat and a rough surface, was used in this work and is summarized in Appendix A. Similar models have also been proposed and have been used to investigate adhesion, contact and friction at the HDI, e.g. accounting for rough, elastic-plastic, multi-layered media, numerically solving the AB equations,

or using power laws to model contact [22, 65, 66]. A lumped parameter 2-DOF nonlinear dynamic HDI model is coupled with the ISBL adhesive contact model to calculate the time varying interfacial forces of adhesion, contact and friction as well as the real area of contact [10]. The interfacial forces are used to obtain the mean contact pressure and shear stress, which determine stable flyability and long term wear, as well as the coefficient of friction, which is not constant for the interface, but varies dynamically with the contact and friction forces. Simulation results identifying the onset of contact were found to compare favorably to experimental results [11]. The dynamic results are analyzed as functions of TFC actuation to identify the regimes of operation. The slider's approach to the disk surface along with the behavior of adhesion at small separations is quantified and an optimum point of operation is identified for the TFC geometry.

The dynamic contact model with friction is used to perform a parametric study of the geometry of the bulge (or TFC protrusion) [10]. This study, which makes use of design-of experiments/analysis-of-variance (DOE/ANOVA) methodologies [67], is four-dimensional in that it features three geometric parameters being varied between three levels (-1, 0 and +1) while a fourth geometric parameter is being varied between four levels of TFC actuation corresponding to fully flying, transitionally flying, transitionally contacting and fully contacting operation. The parametric study yields predictive models that can be used to determine the best combinations of TFC geometric parameters that would improve flyability, i.e. would minimize the clearance and vibrations. To quantify flyability, a parameter is proposed that couples the effects of clearance and vibrations.

Due to the complex nature of the parametric study results, it is difficult to identify a global optimum of the flyability parameter. Hence, an optimization study was also performed to identify a globally optimized design. A global minimum was found for the flyability parameter and an optimum TFC bulge geometry is suggested. The performance of the optimized design is then compared to the initial design and evaluated for improved flyability. The proposed methodology could be readily used to investigate ultra-low flying and contacting HDIs.

2.3.1: Spacing Budget for Tbit/in^2 Recording Densities

The disk and slider surfaces need to be protected by DLC overcoats that, practically can be as

thin as 2 nm since corrosion and oxidation is observed at smaller thicknesses [62]. An MTL layer is also applied on top of the DLC layer and its thickness is about 1.5 nm. Of the total lubricant layer, about half is bonded to the DLC layer while the other half is mobile. Also, the disk and slider surfaces possess roughness with RMS roughness on the order of few Angstroms. Using the GW statistical roughness approach [58], the interface of the two rough surfaces can be modeled as a rigid, smooth and flat surface that comes into contact with a compliant, rough, nominally flat composite rough surface. Typical ultra-high density disk and slider samples have RMS roughness values of few angstroms, resulting in a composite roughness of around 0.5 nm.

Figure 2.23 is a schematic representation of a HDI where the slider accurately follows the dynamic modulation of the disk. This modulation, termed dynamic microwaviness (DMW), is a measure of the large wavelength topographical roughness in a dynamic sense and is confounded with secondary effects such as vibrations of the spindle motor [19]. At any point in time the TFC bulge will be located a certain distance, or HMS, away from the disk surface as shown is Figure 2.23. The target HMS can be calculated using the following equation:

$$HMS_{\text{Target}} = (\text{target magn. clear.}) - t_{DLC,Disk} - t_{DLC,TFC} - t - 3\times\sigma \qquad (2.17)$$

For 1 Tbit/in^2, the target magnetic clearance is 6.5 nm, and the DLC overcoats on the disk ($t_{DLC,disk}$) and slider ($t_{DLC,TFC}$) necessary to prevent oxidation and corrosion are 2 nm each [62], i.e. $t_{DLC,Disk} = t_{DLC,TFC} = 2$ nm. The total lubricant thickness (t) is 1.5 nm, while the combined roughness is ~ 0.5 nm, yielding a value for $3\times\sigma$ equal to ~1.5 nm. Note that for a Gaussian asperity distribution, 99.7% of asperities will be located within $3\times\sigma$ from the mean. Therefore under this scenario, the target HMS for 1 Tbit/in^2 recording densities can be found from equation (2.17) to be - 0.5 nm. Since the HMS is measured from the top of the lubricant layer, negative HMS corresponds to penetration within the lubricant layer. Given that half of the lubricant layer is mobile (with thickness T_0), the TFC bulge will displace the mobile lubricant layer as long as the HMS is kept within the range of 0 to -T_0. This regime of operation is defined as light (lubricant) contact or "surfing" recording. Note that for 1 Tbit/in^2 areal density it is likely that the HMS will be positive (via smaller DLC thickness, for example); however, light sustained contact recording will be necessary with higher areal densities beyond 1 Tbit/in^2.

2.3.2: Results and Discussion

2.3.2.1: Dynamic Contact Simulations

Each simulation solves a switching non-linear system of ordinary differential equations and yields the displacements and interfacial forces as outputs. The derived dynamic quantities of mean pressure $P_m = F_c/A_r$ and shear traction $\tau = Q/A_r$ can be calculated along with the dynamically changing coefficient of friction $\mu = Q/F_c$. The only input to the system is the DMW, which implicitly includes the effects the topographical roughness. DMW causes the system to vibrate with a magnitude that depends on the separation between the surfaces. The vibration magnitude can be expressed as the ratio of the total FH range over the nominal value. The maximum FH is calculated by taking the average of the five largest FH values in the time history; similarly, the minimum FH is calculated from the five smallest FH values. As stated previously, the nominal FH, which is equal to 11 nm, is used as an initial condition in the solution of the dynamic problem. The terminology of FHM and BV is used to differentiate between vibrations during flying or contacting, respectively.

If the separation between the two surfaces is larger than $6\times\sigma$ the preload and AB forces balance out in the absence of significant adhesion and the slider flies with relatively small FHM. During solid contact the adhesion force suppresses the vibrations of the system resulting in BV that are smaller than FHM. Adhesion induces severe vibrations during the transition from flying to contact because the adhesion force, which is formulated based on the Lennard-Jones surface potential, has a large dependence with separation [19]. As soon as the separation becomes equal to or smaller than the equilibrium spacing of 0.098 nm the adhesion force reaches a maximum that scales with the nominal contact area.

Figure 2.24(a) shows a schematic of the clearance (= FH + $T_0 - 3\times\sigma$) as a function of TFC actuation for the case of the initial TFC geometry. Figure 2.24(b) is the respective schematic for an optimized (or "ideal") design, where transition from flying to contacting is "smooth" or stable. Two slopes can be defined that describe flyability performance in terms of the clearance. One is the *approach slope* (A) and the other is the *TD slope* (B). At their intersection we can define a reference point, named the *critical point* (CP). The approach slope has a value of -1

meaning that a nanometer of TFC actuation corresponds to a decrease in clearance by one nanometer. This holds true until the effect of adhesion becomes significant (at the CP). Once adhesion dominates the interface the slider is suddenly pulled towards the disk surface resulting in TD. This jump-to-contact behavior is quantified by the TD slope of -4.35 nm/nm for the initial design. The absolute value of slope (B) is thus more than 4 times that of slope (A). The preferred or ideal behavior of an optimized design should yield similar slopes for the approach and TD such that the sudden jump-to-contact is avoided. In reality the adhesive force, no matter how small in magnitude, will result in some jump-to-contact however, in an optimized design we can expect for (A) to be similar to (B). The critical TFC actuation $h_{TFC,cr}$ (at the CP) is equal to 8.6 nm with a clearance of 2.39 nm for the initial design, meaning that adhesion becomes significant once the TFC bulge is actuated beyond 8.6 nm or clearance is reduced below 2.39 nm.

Negative clearance corresponds to solid contact. TD occurs at 9.7 nm of actuation for the initial design, which is in agreement with flyability experiments [11]. The operational regime of solid contact, shown in gray (darkest hue) in Figure 2.24(a), is identified at the point where the steady state average clearance becomes negative. This does not coincide with TD as the steady state average clearance at TD is positive, indicating that on average the TFC bulge is "flying" within the lubricant layer but starts contacting the solid layer on the downward strokes of its motion. In a similar manner, the operating regimes of bonded lubricant contact (blue or lighter hue) and mobile lubricant contact (yellow or lightest hue) are identified based on the steady state average value of the clearance. Specifically, a steady state average clearance between zero and 0.75 nm corresponds to bonded lubricant contact while a range of 0.75 to 1.5 nm corresponds to mobile lubricant contact. If the steady state average clearance is larger than 1.5 nm then the slider is flying. A schematic of the FHM or BV against TFC actuation for the initial design is shown in Figure 2.25(a); the optimized design schematic is shown in Figure 2.25(b).

The initial TFC geometry yields large FHM (larger than 10%) in the vicinity of the CP. This precludes operation in the lubricant layer as large vibrations could compromise system reliability especially when accounting for manufacturing and operational tolerances. Operation at an actuation of 8.5 nm where the clearance is 2.54 nm results in 8.20% FHM; however, the proximity of this operating point to the regime of large vibrations about the CP is not sufficient

for reliable operation. In addition, the clearance corresponds to an HMS of 2.54 nm – 1.5 nm ≈ 1 nm where 1.5 nm is the total lubricant thickness. Based on the available budget for 1 Tbit/in^2 recording densities (discussed in section 2), the initial design is not sufficient to achieve the target HMS of -0.5 nm. The increase in FHM in the vicinity of the CP for the initial TFC geometric design does not allow for operation within the lubricant layer. The optimized TFC geometry should result in reduced FHM up to the point of TD thus enabling light contact or "surfing" recording as shown in Figure 2.25(b).

2.3.2.2: Parametric Study Results

Parametric studies of the TFC geometry were performed for flyability performance using the flyability parameter ξ. The results are summarized in the form of two-dimensional contour plots shown in the following figures. Each of these plots corresponds to a constant TFC actuation, starting from fully flying (h_{TFC} = 5 nm), to transitionally flying (h_{TFC} = 9 nm), transitionally contacting (h_{TFC} = 12 nm), and, finally, fully contacting (h_{TFC} = 16 nm) regimes.

To visualize the results, one of the remaining three geometric parameters, a_{TFC}, w_{TFC} or x_{TFC}, must be kept at a constant level of -1, 0, or +1 in each plot. For example, examining Figure 2.26, one can observe that it contains three plots of the dimensionless flyability parameter ξ in the space of w_{TFC} and x_{TFC}, each corresponding to one of the three levels of a_{TFC} (-1, 0, and +1 from left to right). Note that all three plots correspond to only one level of TFC actuation, in this case h_{TFC} = 5 nm. Also note that the negative values of ξ were plotted with denser contours so as to show the regimes where there is solid contact. The choice as to which parameter to keep constant in each set was made based on the residual plots of the errors. It was found that, for plotting TFC actuations of 5 and 16 nm (Figure 2.26 and Figure 2.29), keeping the semi-width a_{TFC} constant yielded predictive model equations (and contours) with random distributions of residual errors, whereas keeping either w_{TFC} or x_{TFC} constant for the same actuations showed undesirable bias in the models. Similarly, keeping the offset from the TE x_{TFC} constant yielded the best results for actuations of 9 nm and 12 nm (Figure 2.27 and Figure 2.28).

Each set of contours is represented by a non-linear equation (of the form shown in equation 2) that corresponds to a predictive model specific to the value of the constant parameter and

actuation. These predictive equations are shown, for example for the case of 9 nm of TFC actuation (Figure 2.27), in Table 2.7. Also shown is the cumulative residual error of each equation. It should be noted that, while a 5th order model was used for the residual analysis, this proved to be unnecessary since the important effects between the parameters were only confounded up to the 4th order (e.g. up to the term $b_{1122}x_1^2x_2^2$).

For the fully flying regime (Figure 2.26), it can be observed that increasing the value of a_{TFC} very slightly, decreases ξ while it also increases the effect of w_{TFC} as evidenced by the very small increase in the slope of the contours. The most significant factor affecting flyability during full flight (when compared to the effects of a_{TFC} and w_{TFC} in Figure 2.26) is the offset from the TE x_{TFC}: increasing x_{TFC} increases ξ slightly. During the fully contacting regime (Figure 2.29), the situation is reversed in that x_{TFC} does not affect ξ at all and becomes the most unimportant parameter. A maximum for ξ seems to exist in this regime, which moves to the left, i.e. it is centered at a smaller value of w_{TFC} with increasing a_{TFC}. As expected, TFC geometry does not affect flyability when flying sufficiently away from the disk, i.e. at actuations smaller than $h_{TFC,cr}$, but values for the semi-width a_{TFC} and depth w_{TFC} slightly smaller than the zeroth level – corresponding to smaller nominal areas – seem to minimize the severity of contact.

In Figure 2.27 (transitional flying), it can be observed that the contact zone, represented by the denser contours, is larger for smaller offsets. Hence, if we want to avoid solid contact we would need to maximize x_{TFC}. Referring to Figure 2.27(c), which corresponds to x_{TFC} = 11 μm, we can choose a TFC geometry with a_{TFC} = 4 μm and w_{TFC} = 70 μm that would minimize ξ but keep it positive. Then, when examining the same point in Figure 2.28(c), corresponding to the transitional contacting regime, we can observe that it lies on a maximum and maintains approximately the same value for ξ.

The complex nature of these results makes it difficult to readily select an optimum design. The safest conclusion would seem to be that decreasing the nominal area of contact should yield optimum flyability. Taking into account the results of the fully flying study (Figure 2.26) suggests keeping a moderate level for a_{TFC} while reducing w_{TFC} and x_{TFC}. Hence, a candidate for the optimized TFC geometric design is: a_{TFC} = 3 μm, w_{TFC} = 10 μm, and x_{TFC} = 5 μm. These values are used as initial guesses in the simulated annealing algorithm to perform the global

optimization.

2.3.2.3: Flyability Results for the Optimized Design

Analysis of the parametric plots and the predictive models could shed light into the physics of the problem. However, such analysis alone is not sufficient to clearly identify an optimum geometry, i.e. the values of a_{TFC}, w_{TFC} and x_{TFC} where ξ reaches a global minimum. Hence, simulated annealing was used to optimize the geometry. The initial guesses for the geometric parameters were 3, 10 and 5 μm for a_{TFC}, w_{TFC} and x_{TFC} respectively. The optimization was performed for a constant TFC actuation, h_{TFC}, of 9.7 nm corresponding to the initial design's TD actuation. The algorithm converged to a global minimum of $\xi = 3.69\times10^{-6}$ and the resulting optimized design was: $a_{TFC} = 4.86$ μm, $w_{TFC} = 16.50$ μm, and $x_{TFC} = 6.35$ μm.

Figure 2.30 is a plot of the convergence of the SA algorithm during optimization. Figure 2.30(a) and Figure 2.30(b) show plots of the optimized values of the geometric parameters and the optimized value of the flyability parameter ξ respectively. Figure 2.30(c) and Figure 2.30(d) show similar plots for the initial values of the geometric parameters and ξ. While ξ is large, the SA algorithm uses randomly selected "neighboring" points (values) for the three geometric parameters and calculates the flyability parameter ξ resulting from the selection. As ξ becomes successively smaller the "neighbors" are selected in a more biased manner until the global optimum is found. The stability and sensitivity of the solutions were examined by perturbing each parameter about the optimized value while keeping the other two constant. For example, while keeping a_{TFC} and w_{TFC} at the optimized levels of 4.86 μm and 16.50 μm, x_{TFC} was perturbed from the optimized value of 6.35 μm by a few steps with a step size of 50 nm. The numerical solutions are stable for all parameters, while they appear to be more sensitive to a_{TFC}.

Dynamic contact simulations were performed for the optimized TFC geometric design to produce results that could be compared to the initial design. Figure 2.31 is a plot of clearance versus TFC actuation. Aside from the approach (A) and TD (B) slopes, two additional slopes are used to characterize the transition to solid contact: the *lubricant contact slope* (C); and the *solid contact slope* (D). The flyability performance of the optimized design in terms of clearance has significantly improved. Specifically, the jump-to-contact behavior was successfully minimized

as shown by the very small slope (B) and the small length of the jump-to-contact line in Figure 2.31(b). Correspondingly, the approach and lubricant-contact slopes have remained equal and, because of the reduced jump-to-contact, are almost continuous. Hence, up to the point of solid contact (gray color regime) the slope of -1 indicates that there is a 1nm reduction in clearance per nm of actuation and the effect of adhesion is practically negligible. The contact stiffness is consistent with the initial design as shown by slope (D). The critical actuation is maintained at $h_{TFC,cr}$ = 8.6 nm, while lubricant contact begins at 9.0 nm and TD has been moved to 9.9 nm of actuation. Overall, referring to Figure 2.31, the mobile (yellow or lightest hue) and bonded lubricant regimes (blue or darker hue) have become slightly smaller for the optimized design.

FHM and BV are also significantly reduced with the optimized design. The spike in FHM that was seen at an actuation of 8.6 nm for the initial design has now disappeared; in fact, at the same actuation the FHM is only 6.67% for the optimized design. This allows for operation within the lubricant layer, i.e. light contact or "surfing" recording, with FHM fluctuating around 10% in the range up to TD where it reaches a value of 11.42%. Accounting for manufacturing and operational tolerances, an optimum operating range, shown in Figure 2.32(b), can be defined between CP and TD. A single optimum point can be selected at the center of this range – where the FHM is kept at about 10% – at a TFC actuation of 9.3 nm. The resulting clearance tolerance of ±0.8 nm, or roughly ±4 actuation steps (for a 0.2 nm/step actuation resolution), between CP (clearance of 2.23 nm) and TD (clearance of 0.55 nm) allows for robust and stable actuation control. Table 2.8 provides a summary of the flyability performance of the initial and optimized designs. Time histories of the dynamic simulation results for the optimized design are shown in Figure 2.33 and Figure 2.34 for the steady solid contact case of 12 nm of TFC actuation.

As shown in Figure 2.34(a) the friction coefficient has an average value that is greater than one, indicating that the friction force is larger than the dynamic contact force. This also means that the maximum shear stresses occur on the surface [63] where the shear traction plotted in Figure 2.34(c) can be used to characterize the contact severity. The steady state average value of the shear traction at a TFC actuation of 13 nm is 6.64 GPa. This is smaller than the yield strength of DLC, which can be calculated from its hardness to be 7.2 GPa [64]. The average steady state mean pressure for the same actuation is 4.88 GPa and is smaller than the DLC hardness of 13

GPa. Even though these results suggest that the DLC layer will not yield at steady solid contact, the presence of vibrations beyond TD, which create large maxima for the mean pressure and shear traction, could cause sufficient wear to the DLC layer that would compromise the magnetic layer's integrity and result in loss of data. Further optimization studies could focus on minimizing the shear stresses on the surface and thus wear.

The clearance between CP and TD – except for the small jump-to-contact slope – is linearly reduced with actuation from 2.23 to 0.55 nm. These values correspond to an HMS range between 0.73 and -0.95 nm. At the optimum point of 9.3 nm actuation, the HMS is -0.31 nm while the FHM is 9.19%. These are close to the target values for 1 Tbit/in^2. In fact, accounting for some mild burnishing of the TFC bulge DLC layer, the resulting HMS range from this optimized design should be adequate for extremely-high-density recording.

2.4: SUMMARY

Dynamic simulations were performed using the initial dynamic contact with friction HDI model that accounts for the TFC geometry with input from experimental measurements of DMW and disk roughness parameters [11]. The contact criterion was established in the model based on information from experimental TD measurements. Based on the simulation results, for Tbit/in^2 recording densities, two possible optimum operating regimes were identified: The first involves the actuation of the TFC until TD is detected and retracting it by less than a nanometer so that the FHM is acceptable and sub-nm clearance is achieved. The second possibility is to actuate the TFC further than TD – but within the lubricant regime – until mild contact or surfing is obtained with BV less than 2%. The contact regime is such that disk wear is expected to be minimal and surfing recording is achieved.

Next, an improved 2-DOF dynamic contact model with friction was introduced, applicable to the case of TFC sliders for the purpose of accurately characterizing slider flyability and the severity of contact at the interface [10]. A methodology was presented for the calculation of the nominal area of contact of TFC sliders and improved modeling of the rear AB force was introduced that yields simulation results that are in good agreement with previously reported experimental TD measurements. Clearance was described as a function of actuation in terms of critical and optimum TFC actuations, as well as approach, jump-to-contact, lubricant and solid contact slopes. These were coupled with analysis of the state of vibrations at the interface, allowing for a comprehensive characterization of flyability before, during and at the initiation of solid contact. Furthermore, discrete regimes of operation were identified that can be used to evaluate slider performance in terms of the steady-state average clearance, vibrations and stresses as functions of actuation.

A method was introduced to visualize and quantify near-contact and contact behaviors by analyzing the clearance, vibrations, shear traction and percentage of solid contact with respect to TFC actuation. A discussion of what constitutes severe contact was presented and was used to quantify the contact conditions during and close to TD. Based on this discussion, light contact or "surfing" recording was defined as the operation within the mobile and bonded lubricant layers up to TD. The dynamic simulation results are summarized in Table 2.5.

From the analysis of vibrations existing within the "surfing" recording regime for the TFC slider geometry analyzed in this work, a possible optimum operating point was identified at 8.5 nm of actuation for flying recording. This could yield the desired clearance and vibration characteristics for 1 Tbit/in^2 systems but accounting for manufacturing and operational tolerances would make practical implementation very hard. Hence, further optimization of the TFC geometry could improve flyability. Because of potential wear issues in the severe vibration regime of operation, solid (DLC) contact should be avoided altogether.

Recording densities of 1 Tbit/in^2 can be achieved through the optimization of TFC geometry. Hence, a critical point was identified (CP), rigorously defined using the slopes of the clearance as a function of actuation plots, as well as the actuation where solid contact is initiated, i.e. the TD point, and it was suggested that the range of actuations between these two landmarks constitutes the optimum operating range [13]. Flyability was characterized by analyzing the clearance and vibrations present, while an optimum operating actuation was identified at the center of the range. Based on the analysis of vibrations existing within the "surfing" recording regime for the initial TFC geometry it was shown that a non-optimized design cannot yield the desired clearance and FHM or BV characteristics for Tbit/in^2 systems.

Parametric studies were performed whereby the TFC geometric parameters were varied and a flyability parameter, ξ, was proposed as a measure of flyability performance. The use of this flyability parameter allows for the coupling of the clearance and vibrations such that both can be minimized simultaneously. The smallest possible magnitude of ξ (i.e. as close to zero as possible and positive) would result in the slider surfing on the bonded lubricant layer with reduced vibrations. Decreasing the nominal area of contact by decreasing the values of a_{TFC} and w_{TFC}, improves flyability by decreasing the effect of the adhesive force close to the CP, effectively limiting jump-to-contact behavior. When deciding on an initial guess for the optimum TFC geometry, a_{TFC} was kept at a moderate level based on the parametric study results.

Coupling the parametric with the optimization studies enabled the identification of an optimized geometric design whose flyability performance was analyzed and compared with the initial design. The numerical solution was more sensitive to the TFC ellipsoid semi-width (a_{TFC}). Using the previously established methodology of characterizing flyability, it was found that the

optimized design resulted in reduced clearances and vibrations that would enable operation in the light (lubricant) contact or “surfing” recording regime.

2.5: FIGURES

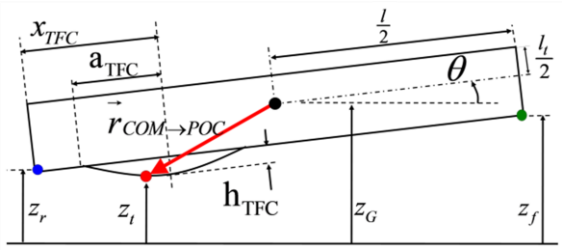


Figure 2.1: Schematic of the slider with TFC bulge used in the improved 2-DOF model, showing the moment arm from the COM to the POC and the displacements as measured from the instantaneous (in time) mean of surface heights (not to scale).

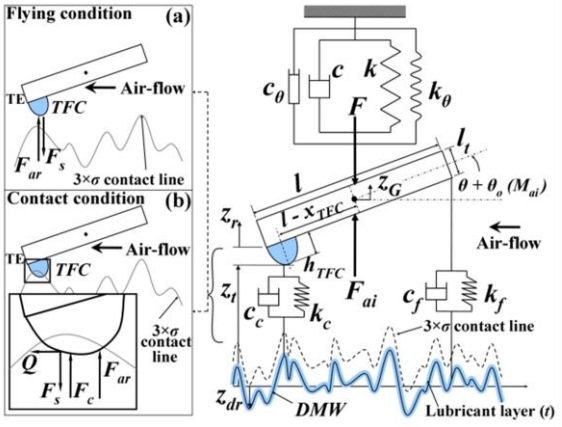


Figure 2.2: Free body diagram of the initial 2-DOF dynamic contacting system. Inset a) shows the flying condition and inset b) shows the $n\times\sigma$ contacting condition. Note: initial model defines contact at $n\times\sigma$.

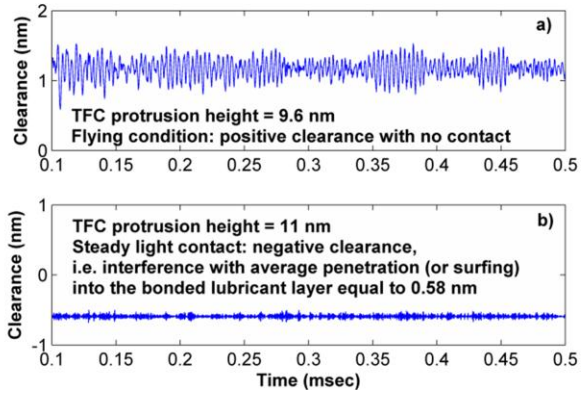


Figure 2.3: Time histories of TFC clearance: (a) TFC pole tip height of 9.6 nm, (b) TFC pole tip height of 11 nm.

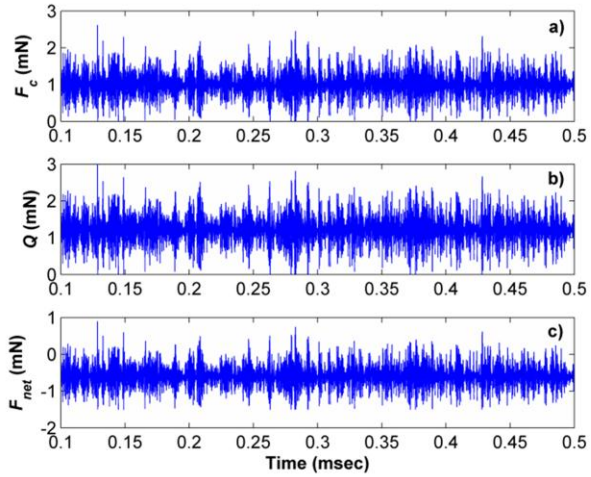


Figure 2.4: Dynamic interfacial forces for 11 nm TFC protrusion: (a) contact force, (b) friction force, (c) net normal force.

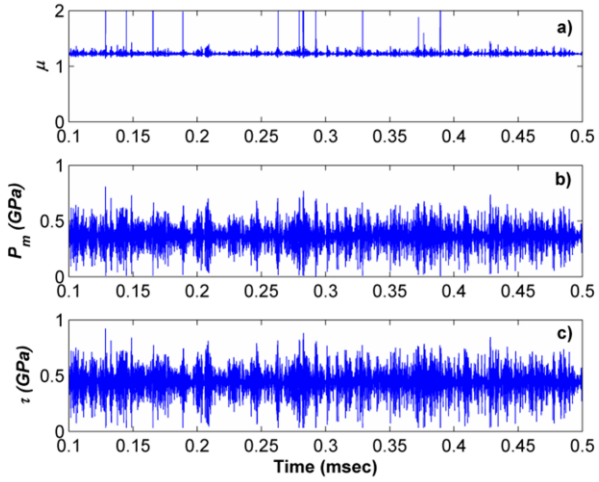


Figure 2.5: Dynamic interfacial parameters for 11 nm TFC protrusion: (a) friction coefficient, (b) mean pressure, (c) shear stress.

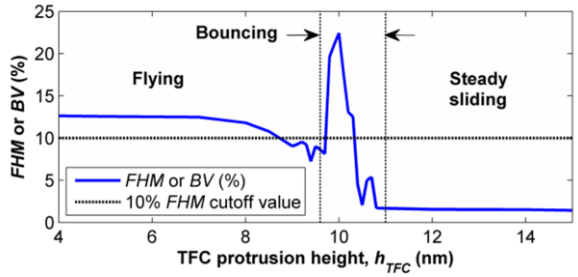


Figure 2.6: FHM or BV versus TFC protrusion height showing flying, bouncing, and steady sliding surfing regimes.

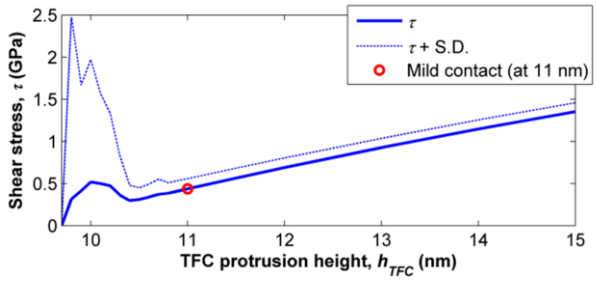


Figure 2.7: Shear stress versus TFC protrusion height from the onset of contact to the contacting regime.

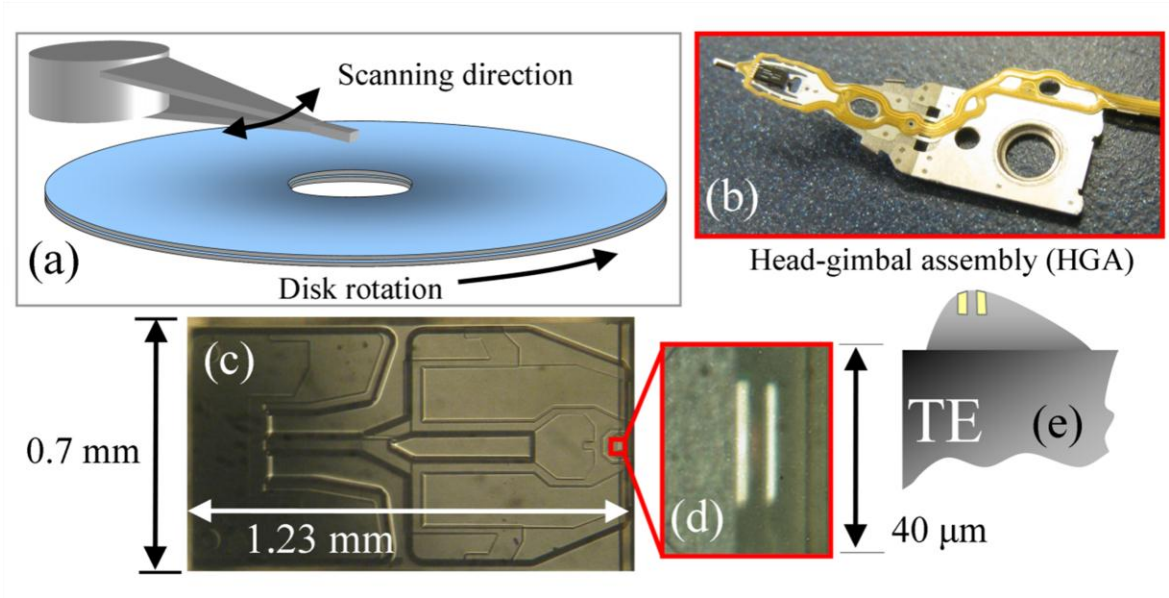


Figure 2.8: Typical HDD HDI. (a) Schematic of a HDI where the HGA can position the slider over any location on the disk surface; (b) photograph of a typical HGA; (c) photograph of a typical slider ABS; (d) slider TE zoom-in micrograph of the location of the read/write elements and TFC protrusion; (e) schematic of the TFC bulge (not to scale).

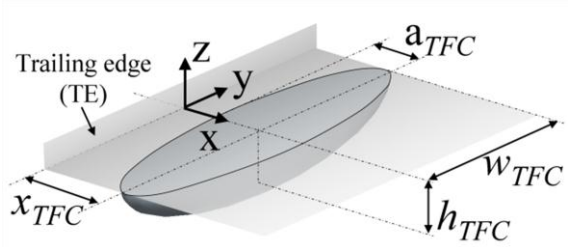


Figure 2.9: Modeling the TFC bulge as an ellipsoid (not to scale). Four parameters are used to characterize the TFC bulge dimensions and its location relative to the origin at the TE: a_{TFC} is the semi-width, h_{TFC} is the height, w_{TFC} is the depth, and x_{TFC} is the offset from the TE.

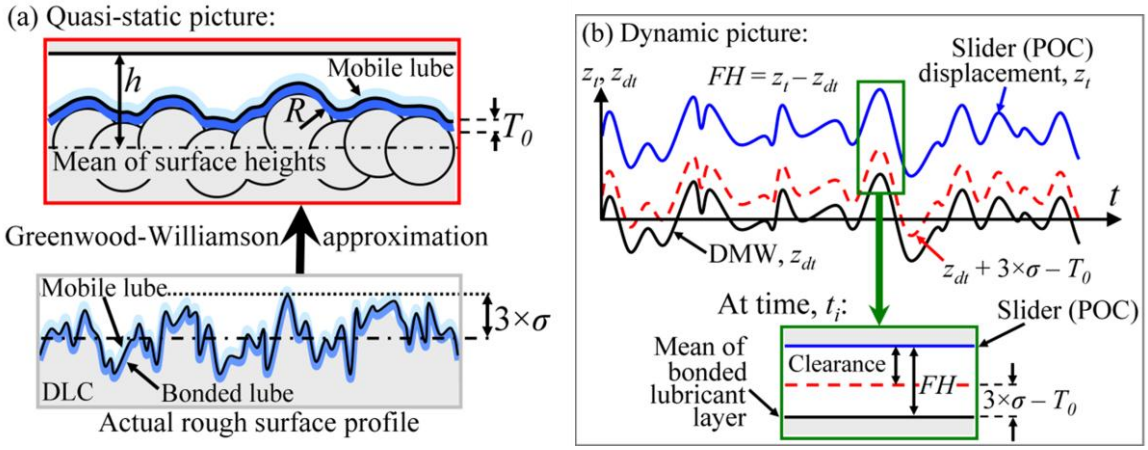


Figure 2.10: HDI schematic showing the coupling of roughness and DMW in the sense of a quasi-static versus dynamic interface: (a) the GW model can be used to approximate the interface between two rough surfaces as that of a rigid smooth flat and a compliant rough nominally flat surface; (b) clearance is measured between the slider surface and the mean of the solid (DLC) layer on the disk, which is represented by the equivalent rough surface, i.e. clearance = $FH + T_0 - 3\times\sigma$. Note that HMS = clearance + $2\times T_0$.

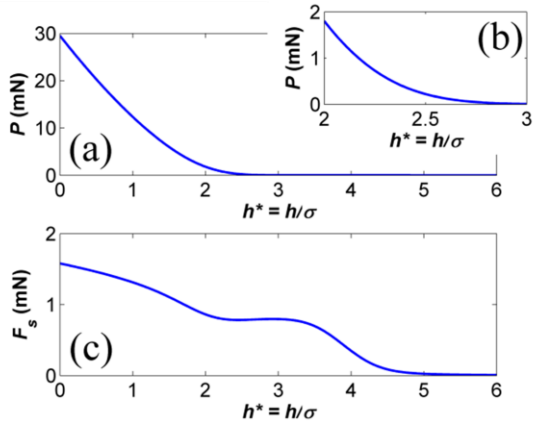


Figure 2.11: Simulation results of the quasi-static contact and adhesion forces against dimensionless separation $h^* = h/\sigma$. The static contact force (a) is undetectable at $h^* = 3$ (b) while the same is true for the adhesion force at $h^* = 6$ (c). Note that h and FH are quasi-static and dynamic representations of the same distance respectively.

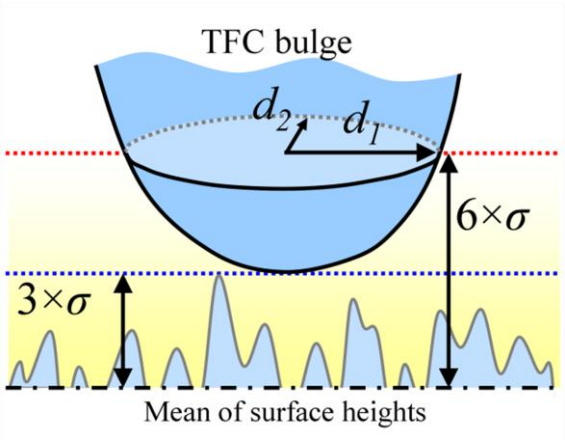


Figure 2.12: Calculation of the projected nominal area of contact by truncating the TFC bulge (ellipsoid) just before contact (not to scale). The truncation yields an ellipse of dimensions d_1 and d_2.

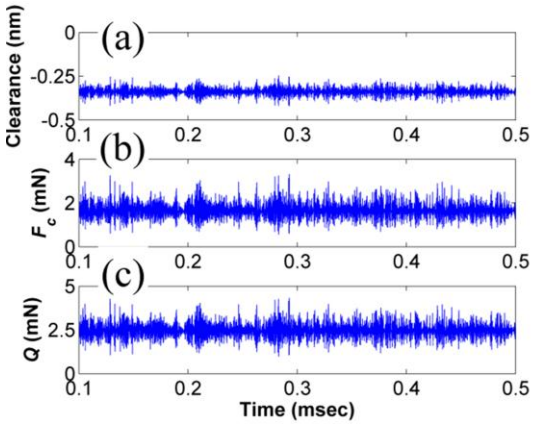


Figure 2.13: Simulation time histories: (a) clearance (= FH + T0 – 3×σ); (b) dynamic contact force; and, (c) dynamic maximum friction force for a TFC actuation of 12 nm corresponding to steady contact.

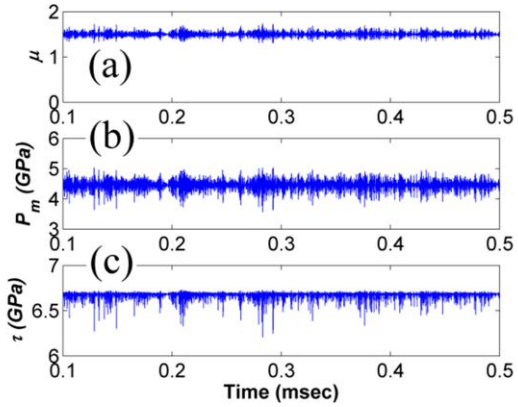


Figure 2.14: Simulation time histories: (a) coefficient of friction; (b) mean pressure; and, (c) shear traction for a TFC actuation of 12 nm corresponding to steady contact.

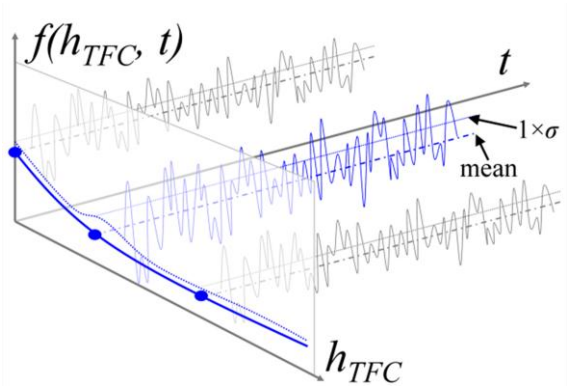


Figure 2.15: Representation of time histories for successive TFC actuation steps as functions of TFC actuation.

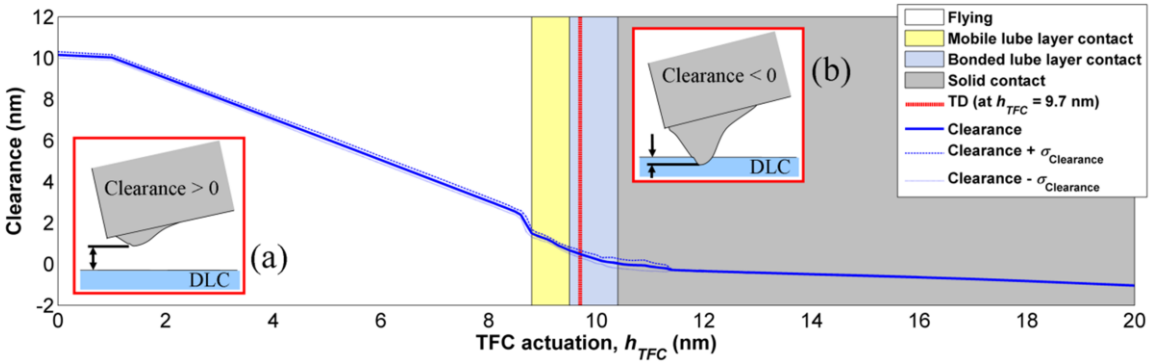


Figure 2.16: Clearance (± one standard deviation) versus TFC actuation. Inset (a) shows the flying state of the slider while inset (b) shows the solid contacting state for TFC actuations larger than 9.7 nm where TD occurs.

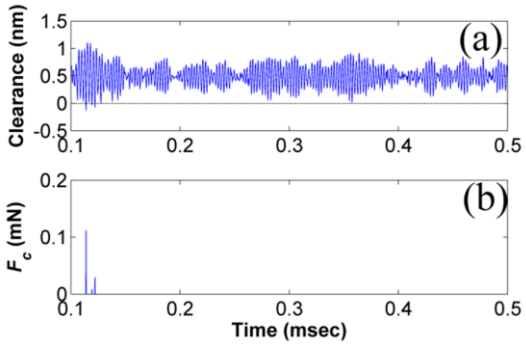


Figure 2.17: Simulation time histories: (a) clearance; and, (b) dynamic contact force at TD (9.7 nm of actuation). The dynamic contact force becomes non-zero when the clearance becomes negative (interference).

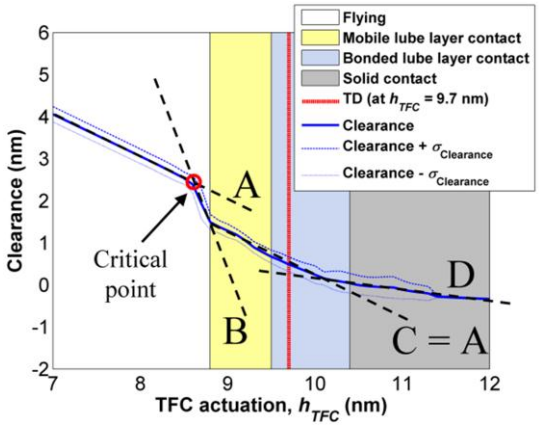


Figure 2.18: Close-up of clearance versus TFC actuation. Note the slopes A, B, C and D as well as the critical point.

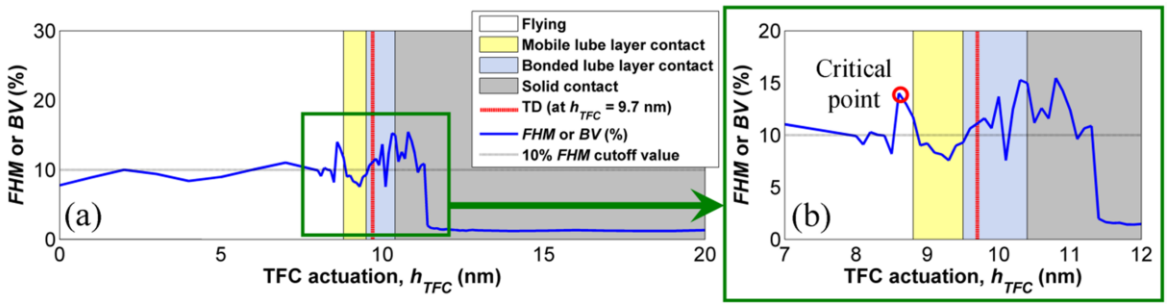


Figure 2.19: FHM or BV versus TFC actuation (a). Inset (b) is a close-up in the TFC actuation between 7 and 12 nm where larger vibrations are present; the critical point is also shown.

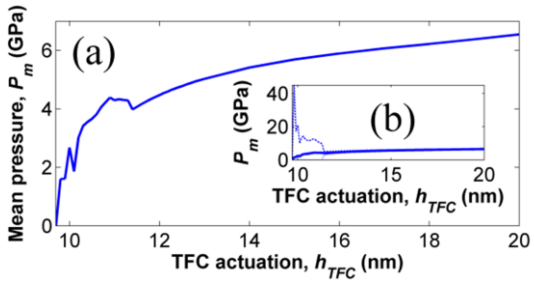


Figure 2.20: Mean real contact pressure versus TFC actuation (a). Inset (b) shows the variation from the average steady-state value.

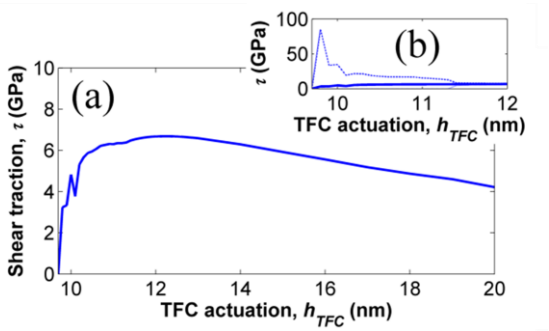


Figure 2.21: Shear traction versus TFC actuation (a). Inset (b) shows the variation from the average steady-state value.

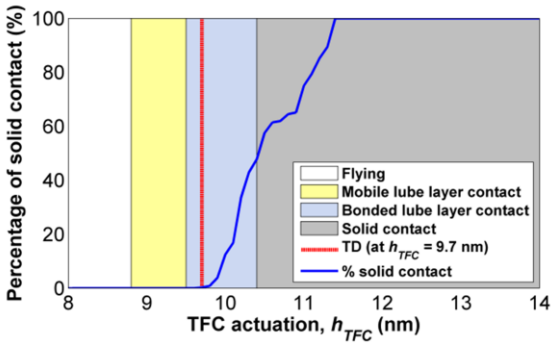


Figure 2.22: Percentage of intermittent solid (DLC) contact versus TFC actuation near and during contact.

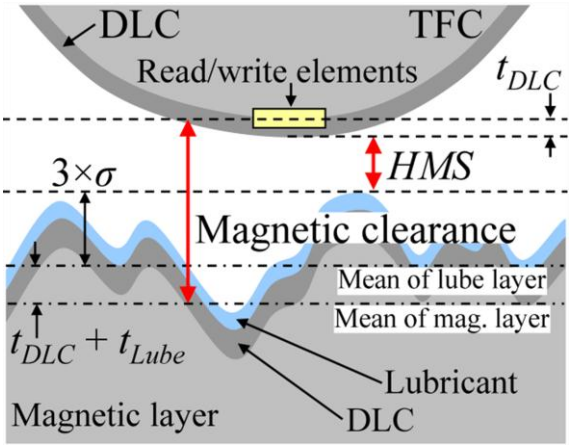


Figure 2.23: Schematic of the HDI. The TFC bulge can accurately track the DMW and the roughness of both the head and the disk are combined on the disk surface.

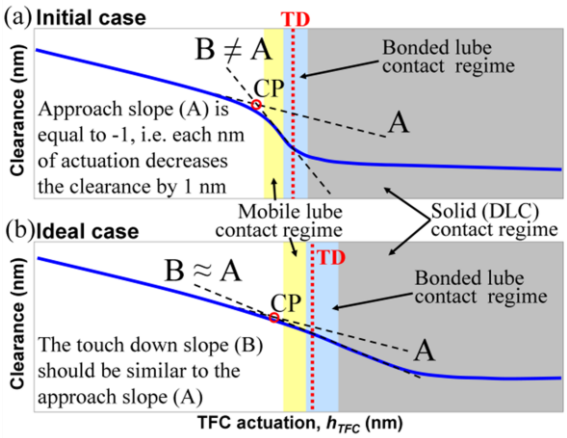


Figure 2.24: Schematic of clearance versus TFC actuation for the initial (a) and optimized (b) cases. Note the regimes of operation (lubricant versus solid contact), the TD, the approach (A) and lubricant contact (B) slopes, and the critical point (CP).

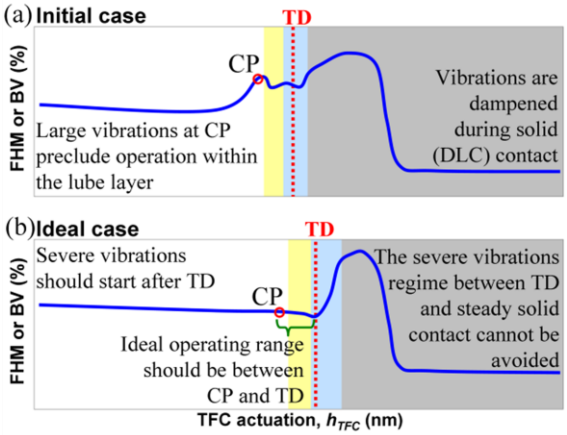


Figure 2.25: Schematic of FHM or BV versus TFC actuation for the initial (a) and optimized (b) cases.

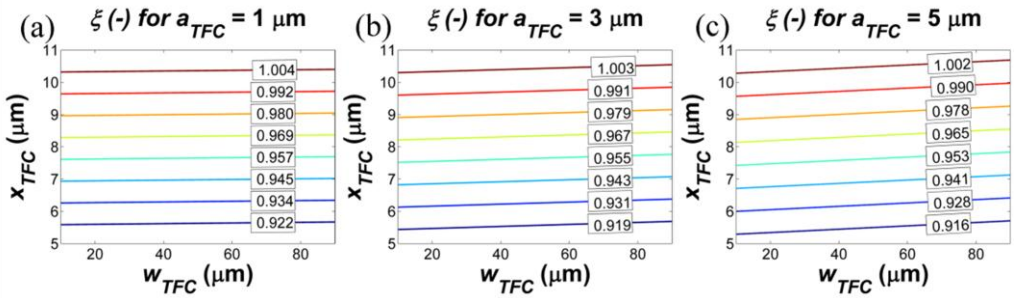


Figure 2.26: Parametric plots of the flyability parameter ξ for the fully flying condition (h_{TFC} = 5 nm): (a) a_{TFC} = -1; (b) a_{TFC} = 0; and, (c) a_{TFC} = +1.

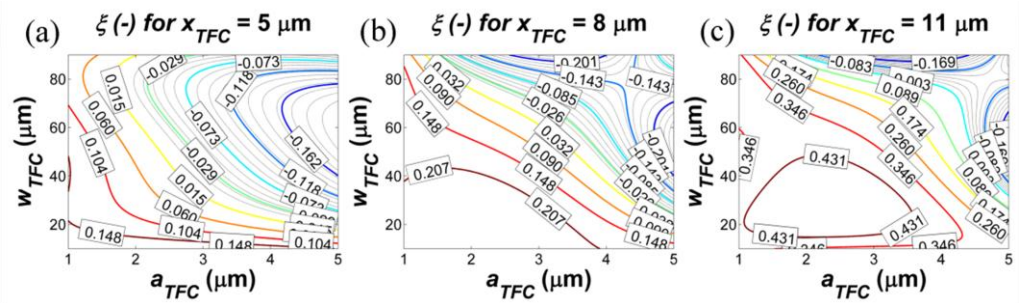


Figure 2.27: Parametric plots of the flyability parameter ξ for the transitionally flying condition (h_{TFC} = 9 nm): (a) x_{TFC} = -1; (b) x_{TFC} = 0; and, (c) x_{TFC} = +1.

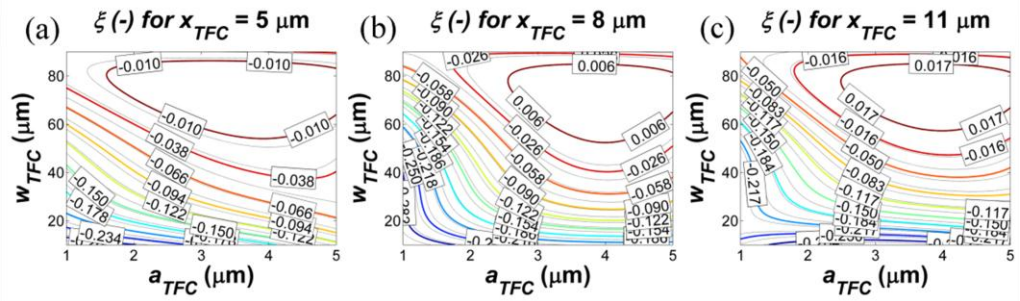


Figure 2.28: Parametric plots of the flyability parameter ξ for the transitionally contacting condition (h_{TFC} = 12 nm): (a) x_{TFC} = -1; (b) x_{TFC} = 0; and, (c) x_{TFC} = +1.

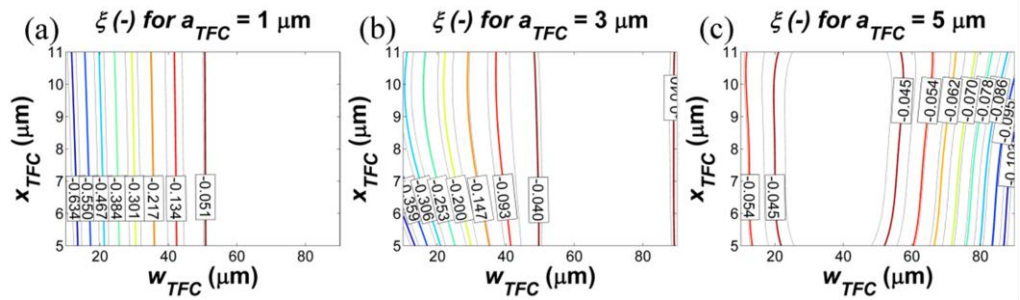


Figure 2.29: Parametric plots of the flyability parameter ξ for the fully contacting condition (h_{TFC} = 16 nm): (a) a_{TFC} = -1; (b) a_{TFC} = 0; and, (c) a_{TFC} = +1.

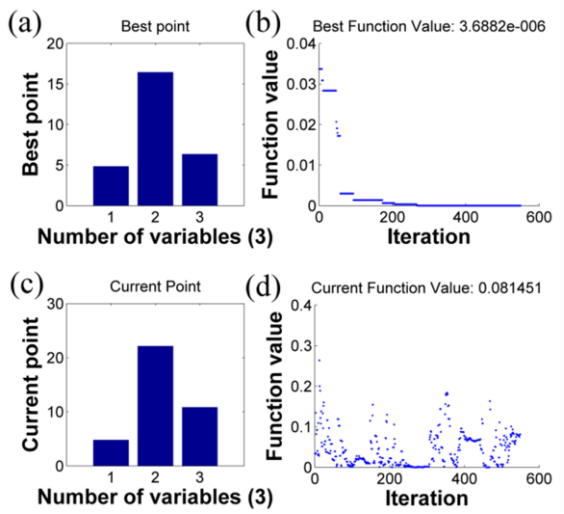


Figure 2.30: Convergence plots of SA algorithm best and current parameter values during optimization: (a) best values of geometric parameters; (b) best value of the flyability parameter ξ; (c) current values of geometric parameters; and, (d) current value of ξ. Plots (c) and (d) show the candidate 'neighboring' set currently tested for optimality by the algorithm.

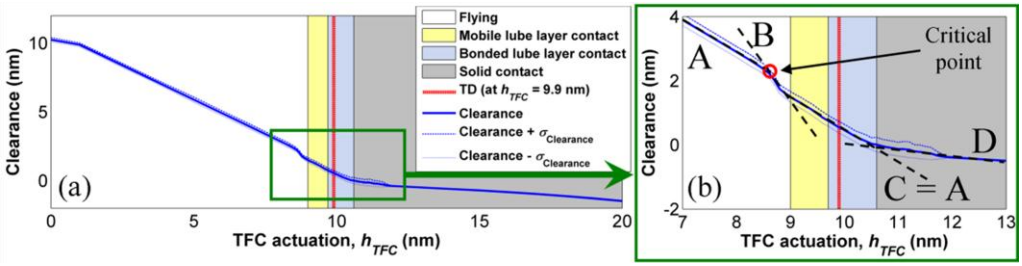


Figure 2.31: Plot of clearance versus TFC actuation for the optimized design simulations (a). Insert (b) is a close-up in the TFC actuation range between 7 and 13 nm.

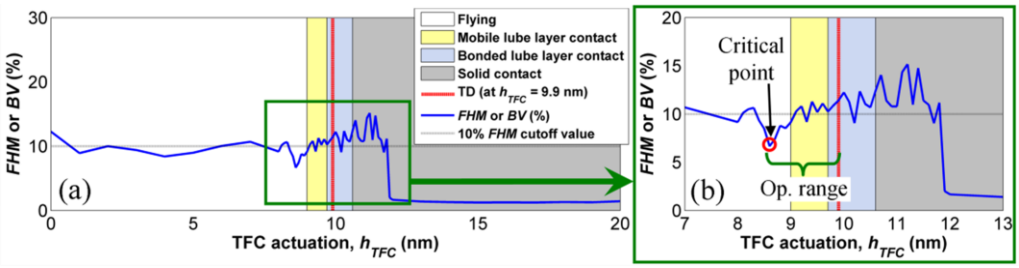


Figure 2.32: Plot of FHM or BVs versus TFC actuation for the optimized design simulations (a). Insert (b) is a close-up in the TFC actuation range between 7 and 13 nm. The suggested operating range is shown between $h_{TFC,cr}$ and TD.

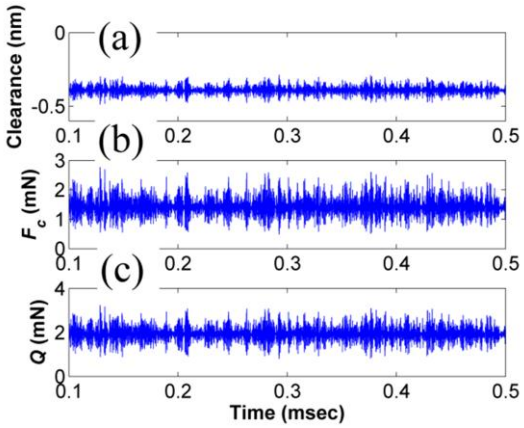


Figure 2.33: Time histories of simulations of: (a) clearance (= $FH + T_0 - 3\times\sigma$); (b) dynamic contact force; and, (c) dynamic maximum friction force for a TFC actuation of 12 nm corresponding to steady contact for the optimized design.

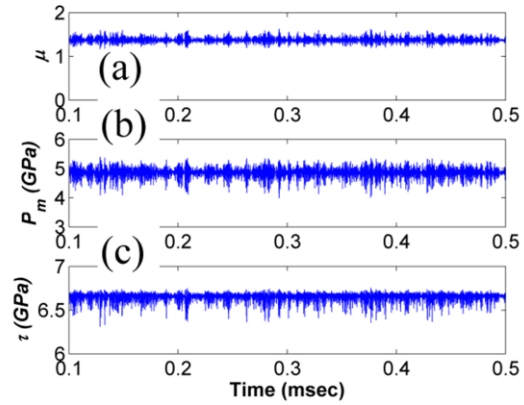


Figure 2.34: Time histories of simulations of: (a) coefficient of friction; (b) mean pressure; and, (c) shear traction for a TFC actuation of 12 nm corresponding to steady contact for the optimized design.

2.6: TABLES

Table 2.1: Dynamic model parameters used in 2-DOF models.

Symbol	Parameter	Value	Unit
a_{TFC}	TFC protrusion half-width	3	μm
h_{TFC}	TFC protrusion height	1-15	nm
w_{TFC}	TFC protrusion width	50	μm
x_{TFC}	TFC protrusion offset from TE	8	μm
nom. FH	Nominal flying height	11	nm
m	Slider mass	0.8932	mg
J	Slider moment of inertia	1.19×10^{-13}	Kg m^2
l	Slider length	1.23	mm
l_t	Slider thickness	0.30	mm
θ_o	Initial pitch-angle	100	μrad
F	Suspension preload	14.7	mN
k	Suspension stiffness	10	N/m
k_θ	Suspension angular stiffness	1.6×10^{-4}	N/m
ζ	Suspension damping ratio	0.01	-
ζ_θ	Suspension angular damping ratio	0.001	-
ζ_c	Contact damping ratio	0.005	-
k_f	Front air bearing stiffness	0.1794×10^{6}	N/m
k_r	Rear air bearing stiffness	0.8100×10^{6}	N/m
ζ_f	Front air bearing damping ratio	0.0075	-
ζ_r	Rear air bearing damping ratio	0.0075	-
t	Total lubricant thickness	1.5	nm
T_o	Bonded lubricant thickness	0.75	nm
ε	Equilibrium spacing	0.098	nm

Table 2.2: Disk and TFC material properties and roughness parameters used in initial 2-DOF model.

Symbol	Parameter	Value	Unit
E_{DISK}	Disk (DLC) Young's modulus	280	GPa
ν_{DISK}	Disk (DLC) Poisson ratio	0.24	-
E_{TFC}	TFC Young's modulus	280	GPa
ν_{TFC}	TFC Poisson ratio	0.24	-
H	Disk (DLC) hardness	13	GPa
$\Delta\gamma$	Surface adhesion energy	0.055	N/m
σ_{DISK}	Disk RMS roughness	0.34	nm
R_{DISK}	Disk mean radius of asperity curvature	0.43	μm
η_{DISK}	Disk areal density of asperities	220	μm^{-2}
σ_{TFC}	TFC RMS roughness	0.80	nm
R_{TFC}	TFC mean radius of asperity curvature	32.74	μm
η_{TFC}	TFC areal density of asperities	1.77	μm^{-2}
σ	Combined RMS roughness	0.87	nm
R	Combined mean radius of asperity curvature	0.43	μm
η	Combined areal density of asperities	212.42	μm^{-2}

Table 2.3: Summary of initial 2-DOF model dynamic results.

b_{TFC} (nm)	Condition	Clearance (nm)	FHM or BV (%)	P_m (MPa)	τ (MPa)
9.6	Flying	1.04	8.6	-	-
9.8	Touch down	0.70	19.6	257	317
10	Largest BV	-0.03	22.4	438	519
10.4	Mildest contact	-0.59	4.54	240	298
11	Steady contact	-0.58	1.68	359	438

Table 2.4: Disk and TFC material properties and roughness parameters used in improved 2-DOF model.

Symbol	Parameter	Value	Unit
E_{DISK}	Disk (DLC) Young's modulus	280	GPa
v_{DISK}	Disk (DLC) Poisson ratio	0.24	-
E_{TFC}	TFC Young's modulus	280	GPa
v_{TFC}	TFC Poisson ratio	0.24	-
H	Disk (DLC) hardness	13	GPa
$\Delta\gamma$	Surface adhesion energy	0.055	N/m
σ_{DISK}	Disk RMS roughness	0.34	nm
R_{DISK}	Disk mean radius of asperity curvature	0.43	μm
η_{DISK}	Disk areal density of asperities	220	μm^{-2}
σ_{TFC}	TFC RMS roughness	0.80	nm
R_{TFC}	TFC mean radius of asperity curvature	32.74	μm
η_{TFC}	TFC areal density of asperities	1.77	μm^{-2}
σ	Combined RMS roughness	0.87	nm
R	Combined mean radius of asperity curvature	0.43	μm
η	Combined areal density of asperities	212.42	μm^{-2}

Table 2.5: Summary of steady-state average dynamic simulation results with improved 2-DOF model.

h_{TFC} (nm)	Condition	Clearance (nm)	FHM or BV (%)	P_m (GPa)	τ (GPa)
8.5	Optimum point	2.54	8.20	-	-
8.6	Critical point	2.39	14.01	-	-
9.7	Touch down	0.49	11.10	1.18	2.59
10.5	50% solid contact	-0.0065	11.17	3.66	5.95
12	Steady contact	-0.39	1.48	4.47	6.68

Table 2.6: 3^3 full factorial design with 4 levels of actuation.

Symbol	Parameter	Level			Unit
		-1	0	+1	
a_{TFC}	TFC ellipsoid semi-width	1	3	5	μm
w_{TFC}	TFC ellipsoid depth	10	50	90	μm
x_{TFC}	TFC offset from TE	5	8	11	μm

Regime description	Symbol	Value	Unit
Fully flying	h_{TFC}	5	nm
Transitionally flying	h_{TFC}	9	nm
Transitionally contacting	h_{TFC}	12	nm
Fully contacting	h_{TFC}	16	nm

Table 2.7: Representative predictive model results and residual errors for ξ (-) at h_{TFC} = 9 nm.

$$\xi = b_0 + b_1x_1 + b_2x_2 + b_{11}x_1^2 + b_{12}x_1x_2 + b_{112}x_1^2x_2 + b_{122}x_1x_2^2 + b_{2222}x_2^4 + b_{1122}x_1^2x_2^2$$

Coefficients	Level -1	Level 0	Level +1
b_0	-0.0402	0.0962	0.367
b_1	-0.170	-0.217	-0.264
b_2	-0.110	-0.227	-0.277
b_{11}	0.0174	-0.132	-0.304
b_{12}	-0.0229	-0.0251	-0.0894
b_{112}	0.0425	0.145	0.190
b_{122}	0.125	0.164	0.158
b_{2222}	0.117	-0.101	-0.320
b_{1122}	0.00687	0.264	0.514
Residual error	8.442×10^{-17}	2.901×10^{-16}	6.567×10^{-16}

Table 2.8: Summary of flyability (clearance and vibrations) results for initial and optimum designs.

Condition	h_{TFC} (nm)	Clearance (nm)	HMS (nm)	FHM or BV (%)
Initial design (a_{TFC} = 3 μm, w_{TFC} = 50 μm, x_{TFC} = 8 μm)				
Critical actuation	8.6	2.39	0.89	14.01
Optimum actuation	8.5	2.54	1.04	8.20
Touch down (TD)	9.7	0.49	-1.01	11.10
Steady contact	12	-0.34	-1.84	1.48
Optimum design (a_{TFC} = 4.86 μm, w_{TFC} = 16.50 μm, x_{TFC} = 6.35 μm)				
Critical actuation	8.6	2.23	0.73	6.67
Optimum actuation	9.3	1.19	-0.31	9.19
Touch down (TD)	9.9	0.55	-0.95	11.42
Steady contact	12	-0.39	-1.89	1.68

CHAPTER 3 – MTL CONTACT MODEL

3.1: SPHERE-ON-FLAT MODEL OF MTL CONTACT

3.1.1: Proposed Physical Model

Before any consideration of lubricant contact, it is important to characterize the lubricant morphology as accurately as possible. The main challenge is the expected breakdown of continuum theory at the nanoscale: are continuum quantities such as "shear rate" valid with few lubricant molecules present at the interface? We address this fundamental question by examining experimental and molecular dynamics simulation data to propose a model of lubricant morphology that captures the limits of continuum theory. Using this model, allows for the prediction of hydrodynamic forces up to the point where continuum breaks down. A qualitative description of lubricant behavior is offered beyond that point and up to the inception of solid contact.

MTL films, such as those used in magnetic storage should have good retention and replenishment characteristics: both characteristics are achieved by using a mixture of bonded and mobile molecules. While at low speeds replenishment of the lubricant seems to be the critical factor in avoiding wear, at high speeds, surface mobility needs to be augmented by a strongly adhered bonded lubricant layer that helps resist asperity penetration (solid-solid contact). A strongly bonded layer coupled with a mobile layer of high viscosity is important at high speeds [68].

Perfluoropolyether (PFPE) lubricants such as Fomblin Zdol2000 and Zdol4000 have polar (hydro*xy*l) end groups that cause some molecules to adsorb onto the magnetic disk surface and become immobile. Surface-induced vitrification and van der Waals interactions are thought to contribute to the formation of a "glassy" layer, approximately one radius of gyration in thickness, in the liquid near a solid surface [41]. In addition, chemical treatments of the lubricant with ultraviolet-rays or annealing as well as the adsorptive nature of the substrate can increase the fraction of molecules that are bonded to the substrate in this "glassy" state where the polymer segments at a certain distance from the solid surface appear to be effectively tethered to that

surface [41, 69]. The remaining molecules are mobile, i.e. free to diffuse, and as they do they slide by, but cannot cut across one another, creating entanglements; these are further enhanced by a restricted geometry [41]. In a monolayer, both bonded and mobile molecules exist within the same plane and the mobile molecules have to spread in the spaces not covered by the bonded molecules, which conform to the solid surface texture [69].

The effect of the adsorbed layer is to move the plane of shear into the liquid, localized at the mid-plane of the film [34, 70]. Beyond a limiting value of the normal load where the film has transitioned into a "glassy" state, the film appears to be nearly rigid and shear is confined to the wall-film interface in what is frequently called "plug-like flow" [70]. With reduced shear rate, PFPE lubricants show viscous behavior since they have more time to conform to the external flow. However, very fast sliding at room temperature may not lead to lubricant depletion because the shear rate may be too fast for the molecules at the boundaries to catch up to external perturbations [32].

The transition to solid-like behavior in thin polymeric lubricant films under high shear rates has also been observed in molecular dynamics simulations [32]. While "shear thinning" behavior is observed with increasing shear rate where functional end groups slow down the dynamics, confinement plays a more dominant role in lubricant rheology [32]. Simulations have shown that chain molecules, rather than crystallizing, change their configuration and orientation markedly as they approach the glass transition; this structure seems to become insensitive to chain length when the film thickness is much smaller than the radius of gyration in a bulk melt [70]. Confinement also retards the lubricant film relaxation process and increases its viscosity; this effect is more pronounced for lubricants with functional ends [32].

The average molecular height of the bonded layer h_B depends on the coverage of the surface area and can be measured experimentally through ellipsometry. The molecular height for a coverage ratio less than one ($C < 1$ a.u.) is less than the monolayer height, which for Zdol4000 is equal to 2.3 nm; in such a case the layer is termed a submonolayer [69]. For example, if the coverage ratio is 0.8 a.u. then the molecular height is $h_B \approx 1.5$ nm, and is less than the monolayer height resulting in the formation of a submonolayer. Note that $C = 0.2$ a.u. is the saturated value of the coverage ratio such that the molecular height of the bonded layer without any treatment, i.e., the

smallest possible bonded layer thickness, is equal to $h_{B,min} = h_B$ (C = 0.2 a.u.) ≈ 1 nm [69].

It is reasonable to assume that some of the mobile lubricant molecules will bond to the shearing surface when lubricant contact is established, creating a second submonolayer, which, in the absence of treatment, will have a thickness of $h_{B,min}$. Fukuzawa *et al.* used non-polar Fomblin z03 PFPE lubricant (molecular weight = 4000 a.m.u.) in their viscosity measurements [44]. Since the non-polar lubricant has polymer chains with non-functional ends, only the smallest possible number of molecules will bond to the substrate corresponding to the saturated coverage ratio of C = 0.2 [69]. Then, the molecular height will be $h_B = h_{B,min}$ = 1 nm. In other cases where the coating material is not DLC, the minimum molecular height will depend on the chemistry between the lubricant molecules and the shearing surface's material. As the gap between the solid surfaces decreases, mobile molecules will be expelled from the interface until, in the limiting case, the two bonded layers will come into contact and will shear past each other. The bonded molecules in the bottom layer will be blocked in their motion because they cannot cut across the molecules tethered to the shearing surface [41]. The minimum solid-solid gap corresponding to this scenario will be equal to the sum of the two layers' thicknesses, i.e., $h_{0,min} = h_B + h_{B,min}$ = 2 nm. Beyond this point, where arguably the definition of shear rate would stop being valid, experimental results seem to show that the interface "breaks down" and one transitions from lubricant-solid to solid-solid contact through the rupture of the lubricant film. Rupture refers to the destruction of bonded layers through chain scission and breaking of bonds, a process through which previously bonded molecules are expelled from the interface allowing for the inception of solid contact.

Figure 3.1 is a schematic representation of the lubricant polymer chains being sheared between two solid surfaces with the top surface moving at a constant velocity U. The mean shear rate in the presence of interfacial slip is customarily determined by fitting a straight line to the average velocity profile in the central part of the channel [37, 39]. This is analogous to using a "hydrodynamic film thickness" where the effective thickness of the immobilized layers is subtracted from the solid-solid distance [71]. We propose that for shear rate to exist as such within the film and in accordance with existing models [37], the presence of at least two monolayers or submonolayers is necessary. In that case, the shear rate within the fluid film will

be equal to the difference in average velocity of the top and bottom layers over the minimum liquid gap. Defining the average layer velocity at the center of each layer's thickness requires the use of the liquid gap d_0, which can be calculated from the solid-solid gap (minimum film thickness) h_0 as

$$d_0 = h_0 - \kappa \tag{3.1}$$

The minimum liquid gap κ depends on the lubricant morphology and chemistry and is defined relative to the minimum solid-solid gap as

$$\kappa = \frac{1}{2}\left(h_B + h_{B,min}\right) \tag{3.2}$$

When deriving the hydrodynamic forces, the liquid gap, given in equation (3.1), is used in place of the solid-solid gap and is valid for the range of $\kappa \leq d_0 \leq t - \kappa$, where t is the total lubricant thickness. For example, in a lubricant of total thickness of 3 nm and a minimum liquid gap of 1 nm, the hydrodynamic forces exist for 1 nm $\leq d_0 \leq$ 2 nm. In terms of the solid-solid gap, this is equivalent to the range of 2 nm $\leq h_0 \leq$ 3 nm, while transition to solid contact occurs for $0 < h_0 \leq$ 2 nm.

Figure 3.2 shows a schematic representation of the different regimes of contact. Itoh *et al.* [31] reported data of the probe amplitude and phase from fiber wobbling experiments with profiles similar to those depicted in Figure 3.2 and postulated that intermittent solid contact starts at the inflection point in the plot of the amplitude gradient (dA/dh_0) – moving from right to left. They then suggest that steady solid contact occurs at a distance of $3\times\sigma$ – where σ is the combined root-mean-square (RMS) roughness of the solid-solid interface for a Gaussian distribution of asperity heights – to the left of the inflection point. However, the reported combined RMS roughness is small ($3\times\sigma$ = 1.89 nm) and does not cover the entire range of transition. It is not entirely clear what happens in this transitional region. What seems to be clear from the experimental results is that there are two regimes to the right and left of the transition that correspond to steady lubricant and steady solid contact, respectively, as shown in Figure 3.2. Therefore, we propose that the transition region represents the approaching and shearing of the two bonded layers as well as the

transition from intermittent to steady solid contact. Specifically, the transition region contains the following two "events" that may or may not be happening concurrently:

1. Rupture of the adsorbed lubricant layers through the destruction/expulsion of bonded molecules from the interface, as explained previously; continuum behavior breaks down in this region.

2. Transition from intermittent to steady solid contact.

Hence, with decreasing probe-substrate gap (from right to left) the probe comes into steady lubricant contact and reaches the maximum of the hydrodynamic forces just before it transitions through intermittent/asperity contact and lubricant film rupture into steady solid contact. For $h_{0,min} = 2\kappa = 2$ nm, the width of the transition region is equal to $2\kappa+3\sigma \approx 4$ nm, which agrees with the experimental data reported in [31]. As described previously, roughness plays a role in the shear response of the FWM experiments in that the shear response is no longer quantized with respect to separation (as is the case for experiments utilizing atomically smooth surfaces), while the viscosity becomes larger than elasticity for rough surfaces. Since the FWM data is "capped" up to the breakdown of continuum, the effect of roughness is diminished given that $2\kappa > 3\sigma$, and a smooth sphere-on-flat model can be used to analyze the experimental results.

Given that the viscosity reaches its maximum value when the minimum film thickness is 2κ, the hydrodynamic forces, which also reach a maximum at this point, become equal to the solid forces over the transition gap. It is not the purpose of the current work to describe exactly the behavior of the lubricant in the transition gap, since the goal is to predict the hydrodynamic forces present up to the breakdown of continuum, i.e., for $h_0 > 2\kappa$. It is possible that compressive stiffness increases until the bonded molecules are confined to a thickness comparable to their radius of gyration [41]. On the other hand, assuming simply that resistance to shear and compression ceases in the transition gap, the transitional forces can be modeled through linear equations:

$$P_{trans} = \frac{P_{fluid,max} - P_{solid,min}}{2\kappa} h_0 \tag{3.3}$$

$$Q_{trans} = \frac{Q_{fluid,max} - Q_{solid,min}}{2\kappa} h_0 \tag{3.4}$$

$P_{fluid,max}$ and $Q_{fluid,max}$ are the hydrodynamic forces at the limiting maximum viscosity and shear rate. $P_{solid,min}$ and $Q_{solid,min}$ are the normal and frictional forces at the inception of solid contact. The range of solid-solid gaps where these equations hold is $0 < h_0 \leq 2\kappa$, whereas hydrodynamic forces are valid for the range $2\kappa \leq h_0 \leq$ t. At and beyond the inception of solid contact, i.e., for negative solid-solid gap h_0, we describe the forces as functions of interference ω (note that solid forces are zero for $\omega \geq 0$).

Using one of the available interfacial models for a sphere-on-flat geometry [72], the normal and frictional forces can be calculated at the inception of solid contact based on material parameters. Let the hardness, Young's modulus and Poisson's ratio of DLC be 18 GPa, 180 GPa and 0.24 respectively [73]. Since both the sphere and the substrate are coated with DLC, the reduced modulus can be calculated to be 95.5 GPa. Then, $P_{solid,min}$ = 1.5 μN and $Q_{solid,min}$ = 120 μN for ω = 1 Å (the same forces are 40 μN and 1120 μN for ω = 1 nm). It will be shown later that the hydrodynamic forces can be of the same order of magnitude as the solid forces at the inception of solid contact. The authors have incorporated these transitional forces in a generic rough surface model [24], expanding on previous work [10, 11, 13, 19].

The "true" average shear rate in the lubricant film is [37]

$$\dot{\gamma}_{true} = \frac{U - u_s}{d_0} \tag{3.5}$$

The slip velocity us is defined later. However, in the absence of knowledge of slip behavior, the "apparent" shear rate measurable in experiments is based on the displacement of the shearing surface and is defined as

$$\dot{\gamma} = \frac{U}{d_0} \tag{3.6}$$

The maximum shear rate occurs when the minimum solid-solid gap is equal to 2κ corresponding to a minimum liquid gap $d_{0,min} = h_{0,min} - \kappa = \kappa$.

3.1.2: Modeling Viscosity and Interfacial Slip

3.1.2.1: Apparent Lubricant Viscosity Model

Several experimental measurements of dynamic viscosity as a function of gap or shear rate have been published for polymeric melts. Early studies used the SFA with the fluid being sheared between atomically smooth mica surfaces [29, 41, 74]. The FWM [30, 31, 44], based on the same principle as the SFA, uses high shearing frequencies of 100 Hz to few kHz to accurately measure the shear force with a vibrating, spherical-shaped optical fiber probe that is smaller than the one used in a typical SFA [31]. Earlier experiments utilized a lubricant droplet with thickness of 1 μm and 102 μm radius probe [30]; in such an apparatus, the spherical probe is only partially submerged in the lubricant film. In later experiments, the lubricant droplet was sufficiently thick for the probe to be fully submerged in the lubricant [31, 44].

For gaps smaller than 500 nm, PFPE lubricant viscosity increases monotonically to a maximum value about 30 times larger than the bulk-state viscosity in FWM experiments [31]. An increase in elasticity (not synchronized with the increase in viscosity) is observed when opposed adsorbed layers touch each other. However, elasticity also includes the compliance of the apparatus in dynamic shearing experiments and does not represent solely the elastic compression/shearing of the adsorbed polymer layers [71]. In ideally smooth and flat geometries, shear response is linear below a certain lubricant film deformation amplitude. Overall, the transition from linear to nonlinear response is associated with significant changes in the structure of the confined molecules and its mechanism is slippage along an interface [33]. Linearity can be assured in dynamic shearing experiments by using small oscillation amplitudes and by limiting the interpretation of experimental results up to the breakdown of continuum theory, beyond which the shear response becomes nonlinear. In the FWM, the sphere displacement is measured directly with optical methods and the dynamic viscosity is extracted by solving the resulting linear ordinary differential equation for the damping term [30]. During lubricant contact, this is equal to the shear force acting on the sphere

$$Q_{fluid} = c\dot{x} = \eta \Omega U \tag{3.7}$$

The average linear velocity of the probe is $U = 2fA$, where F is the driving frequency, A is the vibration amplitude of the probe, η is the dynamic viscosity, and the damping coefficient is $c = \eta\Omega$. The geometric term Ω used by Fukuzawa *et al.* was derived from the work of Goldman *et al.* [75] and is valid for a fully submerged sphere. The fully-submerged formulation is not applicable in magnetic storage applications where slider features are larger than the lubricant thickness; hence, a new geometric term for the case of a partially submerged sphere is introduced later in the present work for that purpose.

Dynamic viscosity η^* is a complex quantity that describes the system response in terms of the out-of-phase viscous term η' and the in-phase elastic term η'':

$$\eta^* = \eta' - i\eta'' \tag{3.8}$$

It is related to the commonly used dynamic modulus G^* [29, 41, 74] through the vibration frequency such that $G^* = 2\pi f\eta^*$; the storage modulus $G' = 2\pi f\eta''$ (in-phase) and the loss modulus $G'' = 2\pi f\eta'$ (out-of-phase) are the components of G^* [76]. The maximum shear rate that occurs prior to the inception of solid contact is found from equation (3.6) to be 2×10^5 s^{-1}. Note that in order to estimate the "true" shear rate, i.e. the shear rate within the fluid, it is necessary to know the slip behavior as well.

The viscosity-liquid gap data adapted from Fukuzawa *et al.* [44], shown in Figure 3.3(a), can also be expressed as the viscosity-shear rate data shown in Figure 3.3(b) where the shear rate is calculated from equation (3.6). Using the dynamic viscosity data up to the gap where it reaches its bulk value (~500 nm) would enable the comprehensive description of lubricant viscoelasticity, for example by using Prony series representation of the viscosity-shear rate data [76]. Based on the above-mentioned experimental measurements [44], the limiting viscosity-gap behavior of the lubricant can be described as follows:

1. As the gap d_0 approaches the limiting value of κ = 1 nm, or equivalently, as the shear rate becomes very large, the dynamic viscosity (both η' and η'') shows a significant increasing

trend. When the liquid gap is $d_0 = \kappa+$ just prior to the inception of solid contact the viscosity reaches a maximum limiting value η_0. This value can be extracted from experimental data; for example, from the measurements of Fukuzawa *et al.*, η_0 = 0.31 Pa s. Beyond the maximum limiting shear rate of 2×10^5 s^{-1} where this occurs, the viscosity remains constant at η_0.

2. At the other end of the spectrum, as the liquid gap becomes very large corresponding to very low shear rates, the viscosity approaches its bulk value η_∞ = 0.06 Pa s [44].

3. Therefore, the dynamic ("apparent") viscosity is bounded between the bulk and maximum values. The shear rate of interest in magnetic storage is of the order 1×10^{10} s^{-1} as reported in the literature [32]. Hence, the viscosity during HDD operation can be assumed to be constant and equal to the limiting viscosity η_0.

We propose that the viscosity-shear rate behavior can be adequately modeled from experimental data through a second-order polynomial such that

$$\eta = \eta(d_0) = ad_0^{\,2} + bd_0 + \eta_0 \tag{3.9}$$

To express the viscosity as a function of shear rate rather than the gap, the above equation can be reformulated as

$$\eta = \eta(\dot{\gamma}) = a'(\dot{\gamma})^{-2} + b'(\dot{\gamma})^{-1} + \eta_0 \tag{3.10}$$

$$a' = aU^2 \tag{3.11}$$

$$b' = bU \tag{3.12}$$

For the experimental measurements of Fukuzawa *et al.* discussed above [44], the modified coefficients are: a' = 7.014×10^6 Pa s and b' = -2.090×10^3 Pa. Only the viscous component of the dynamic viscosity is used in the hydrodynamic force formulations; therefore, from this point on

and for the sake of simplicity the dash is dropped from the notation such that $\eta = \eta'$. Furthermore, it should be stressed again that η is the "apparent" viscosity that includes the coupled effects of both stiffening and slip.

3.1.2.2: Lubricant Interfacial Slip Model

To account for deviation from classical hydrodynamics, a dimensionless factor can be introduced to append the classical equations [34-36, 77]. The extent of the deviation from the classical prediction increases with increased velocity under constant film thickness [36]. The degree of slip increases both with the viscosity and the shear rate, while it also depends on the cohesive force at the interface: for example, a hydrophobic surface is expected to give rise to partial slip [34]. In fact, the contact angle drastically affects the boundary condition [39]. It has been shown experimentally that, while in a completely wetting system in the absence of polymer the degree of slip increases as the surface roughness increases, the opposite is true in the presence of polymer [34]. In experiments with equivalent surfaces having variable roughness, it was observed that the critical shear rate and stress for the initiation of partial slip increased nearly exponentially with increasing roughness [35].

Numerous boundary conditions were proposed in phenomenological models that allow for finite slip at the liquid-solid interface, but these fail to provide a universal picture of the momentum transport there [40]. Slip will depend, among others, on the strength of the liquid-solid coupling (wall friction, η_w), the thermal roughness of the interface, and the commensurability of the wall and liquid densities [40]. At high shear rates, the slip length increases rapidly with the shear rate and appears to diverge as the shear rate approaches a critical value [40]. For flows in the vicinity of the critical shear rate, small changes in the surface properties can lead to large fluctuations in the apparent boundary condition; hence, the same liquid molecules sheared against different substrates will experience varying amounts of slip and vice versa [40]. Beyond the critical shear rate, the wall can no longer impart additional momentum to the liquid layer, reaching an asymptotic value of the slip length, which increases monotonically with increasing chain length [38]. Scaling the slip length by its asymptotic limiting value and the shear rate by its critical value collapses the data onto a master curve; therefore, the Navier model describes only the low-shear-rate limit of slip behavior [40]. This behavior was shown to be more generally applicable

to polymeric systems [38].

Molecular dynamics simulations that predict unbounded slip length at high shear rates use rigid walls where the wall atoms have no thermal motion; if, instead, the wall atoms are allowed to oscillate about their positions in response to collisions with liquid molecules, momentum transfer is accounted for and the slip length is bounded [37]. This simulation result is verified by dynamical modeling and continuum fluid dynamics: specifically, the slip length is nearly constant and close to zero at low shear rates and increases sharply to reach a constant value that depends on the value of the wall friction η_w. If the wall friction is zero then the slip length becomes unbounded at high shear rates [37].

It should be noted that, in keeping with the model presented herein, slip will not occur at the fluid-solid interfaces per se, but rather at the interface between the bonded and mobile layers as those were described previously. Since the top and bottom interfaces are similar, the slip behavior at each can be assumed to be the same. Hence, the net slip behavior can be modeled, through the slip velocity as a function of gap or shear rate, as occurring only at the top submonolayer-mobile layer interface: we shall refer to this interface as the "top wall." The classical definition of the slip velocity is that it is equal to the slip length multiplied by the local shear rate U/d_0 [37]. Here we incorporate the aforementioned friction constant at the top wall η_w that describes the strength of the solid-liquid interface and the slip length as a function of the liquid gap to propose the following form for the slip velocity

$$u_s = \frac{UL_s}{\eta_w d_0} \tag{3.13}$$

It is more convenient to use the dimensionless slip velocity defined as

$$u_s^* = \frac{u_s}{U} = \frac{L_s}{\eta_w d_0} \tag{3.14}$$

When the friction at the wall η_w is infinite, then the slip velocity is zero as is expected with the no-slip condition. If the friction is zero then the slip velocity becomes unbounded (infinite).

Furthermore, when the slip velocity becomes larger than the shearing velocity, the slip practically becomes unbounded. Let us then propose the following boundary condition at the top wall (wall velocity):

$$u_w = H\left[1-u_s^*\right]\left(1-u_s^*\right)U \tag{3.15}$$

The Heaviside step function is used such that

$$H\left[1-u_s^*\right] = \begin{cases} 0, \text{ if } u_s > U \\ 1, \text{ if } u_s \le U \end{cases} \tag{3.16}$$

A dimensionless slip factor f^* can be defined that scales the classical Reynolds equation for the flow and hence the normal force acting on the sphere. This is shown later to be

$$f^* = H\left[1-u_s^*\right]\left(1-u_s^*\right) = \frac{u_w}{U} \tag{3.17}$$

The factor f^* has the following limiting behavior: at the limit of one, the equations revert to the no-slip condition; the non-physical limit of zero corresponds to unbounded slip. Characteristic values of the slip and wall velocities as well as f^* are given for various cases in Table 3.1.

The Heaviside function accounts for unbounded slip by "turning off" the velocity at the wall. The predicted normal force that can be exerted on the sphere in the case of unbounded slip is infinite as can be seen from the value of f^*. Obviously, this cannot be realized in practical applications. Therefore, f^* is valid in the range $0 < f^* \le 1$. It should be noted that, through algebraic manipulation of equation (3.5), the "true" shear rate accounting for slip can be expressed as

$$\dot{\gamma}_{true} = f^* \frac{U}{d_0} \tag{3.18}$$

Molecular dynamics simulations [37] show that for shearing speeds larger than about 8 m/s, the

slip length becomes constant and equal to about 3 nm; the no-slip condition appears to be valid for speeds smaller than 2 m/s. Based on the approach of Zhu and Granick [36], it would be possible to extract the slip behavior of the lubricant from experimental measurements of the hydrodynamic normal force; however, those authors assumed a constant value for the viscosity whereas the viscosity stiffens as well under the effects of confinement and high shear rate. This is why, after fitting the theoretical prediction of the normal force to the experimental data, Zhu and Granick attributed any deviation from the experiments to interfacial slip alone [36]. We propose, instead, that both viscosity stiffening and slip are present at the interface.

Fukuzawa *et al.* measured in their experiments the normal load during shearing and compared it to the theoretical prediction of classical solution without slip; they found that the classical solution is in good agreement with the experimental data [44]. We further propose that any differences between the experimental and theoretical data arise from violation of the boundary conditions used in the formulation of the normal force as will be discussed later. The general agreement between the reported experimental and theoretical data is not surprising since the "apparent" viscosity measured in the experiments and used in the calculation of the normal force includes both the effects of viscosity stiffening and interfacial slip. In order to investigate slip specifically, it is necessary to decouple its effects from those of viscosity stiffening. To this end, simultaneous measurements of both hydrodynamic – normal and shear – forces or molecular dynamics simulations specific to the studied system/lubricant morphology are necessary. A qualitative method to decouple viscosity stiffening and interfacial slip is later introduced that requires making certain assumptions on the strength of the solid-liquid interface, i.e., the value of the wall friction η_w.

3.1.3: Hydrodynamic Forces

3.1.3.1: Reynolds Equation for a Sphere-on-Flat Accounting for Slip

Only the viscous response, i.e. the viscosity η', which is 90° out of phase with the sinusoidal input and in phase with the rate of deformation, is used in the hydrodynamic force calculations [41]. To derive the hydrodynamic forces, a sphere-on-flat formulation is used, as shown in Figure 3.4. A rigid smooth sphere of radius R moves with constant velocity *U* along the *x*-

direction parallel to a rigid smooth plane; the assumption of rigidity is used only during fluid contact. This is done in lieu of the classical elastohydrodynamic approach [78, 79] so as to yield easily usable, closed-form solutions of the hydrodynamic forces that can be integrated into existing rough surface dynamic contact models [48]; solid deformations are indeed negligible during hydrodynamic contact (of the order of p_m) when the substrate is DLC. It should be noted that the formation of ripples (moguls) under the effect of air stress on the lubricant layer [80, 81] is neglected in the present work and we assume that the lubricant layer is of constant thickness everywhere. Ripples can be modeled within the context of a dynamic contact model [10], for example, by dynamically varying the lubricant thickness under the slider at the HDI.

The approach of the solid surfaces at the lowest point of the sphere is termed the minimum film thickness or solid-solid gap h_0 [78]. Based on the preceding discussion, the minimum film thickness can be replaced by the liquid gap d_0 using equation (3.1). In the sphere-on-flat configuration, shown in Figure 3.4, the total effective bonded layer, comprising half of each bonded layer, is placed on the substrate to simplify the analysis and the solid-solid and liquid gaps are shown relative to the overall lubricant thickness. The following solutions are valid only when the total fluid film thickness t is much smaller than the sphere radius, i.e. $t \ll R$.

The following list of assumptions is used in the derivation of the Reynolds' equation describing the pressure distribution in the lubricant:

1. The fluid is isoviscous along its thickness and its viscosity depends only on the degree of confinement, i.e. $\eta = \eta(h_0)$. The latter can be achieved by using a very small oscillation amplitude to ensure the linearity of the response and isolate the effect of confinement (rather than that of the shear rate) [33].

2. The sphere and elastic half-plane are rigid during lubricant contact. This was reported to hold true in the literature [31].

3. The gap between the sphere and the plane surface is much smaller than the sphere radius, i.e. $h_0 \ll R$. Due to the problem definition where we have specified that $t \ll R$ and $h_0 < t$ for fluid contact to occur, this assumption is valid.

4. Because the gap is small compared to the sphere and substrate dimensions, the pressure is assumed to be constant across the film thickness, i.e. $\partial p/\partial z = 0$.

5. The flow is laminar. Indeed, the Reynolds number is very small for the length-scale of the problem even at very high shear rates [38].

6. Inertial and surface tension forces are negligible relative to viscous forces. This has been reported to hold [36], not least because the probe displacement in the vertical direction can be precisely controlled.

7. Shear stress and velocity gradients are only significant across the film thickness.

8. The materials of the sphere and substrate are the same or sufficiently similar such that the slip behavior is the same at both solid-fluid interfaces. This is true, for example, in magnetic storage where both the slider (sphere) and disk (substrate) are coated with DLC [10, 11, 13].

The velocities in the liquid, denoted u and v in the x- and y-directions respectively, can be obtained by integrating the forces acting on an infinitesimally small element of dimensions $dx \times dy \times dz$ with respect to z. The necessary boundary conditions are: $u(0) = v(0) = v(\mathrm{h}) = 0$, and $u(h) = u_w$, where h is the film thickness with the origin of the coordinate system located under the bottom of the sphere a distance κ away from the substrate (as shown in Figure 3.4) such that

$$h = d_0 + \frac{x^2}{2R} + \frac{y^2}{2R} \tag{3.19}$$

The viscosity used in the following equations is the "true" viscosity that is assumed to be decoupled from interfacial slip and only includes the effects of viscosity stiffening due to confinement and high shear rates. The following velocity distributions are obtained after integrating the force balance equations twice and applying the boundary conditions:

$$u = \frac{1}{2\eta_{true}} \frac{\partial p}{\partial x}\left(z^2 - zh\right) + \frac{z}{h} H\left[1 - u_s^*\right]\left(1 - u_s^*\right)U \tag{3.20}$$

$$v = \frac{1}{2\eta_{true}} \frac{\partial p}{\partial y}\left(z^2 - zh\right) \tag{3.21}$$

The pressure gradient term in u corresponds to Poiseuille flow and the velocity term corresponds to Couette flow with an adjustment for slip. Using conservation of mass, the Reynolds equation can be obtained and corresponds to the classical solution given in the literature [78] appended for slip:

$$\frac{\partial}{\partial x}\left(h^3 \frac{\partial p}{\partial x}\right) + \frac{\partial}{\partial y}\left(h^3 \frac{\partial p}{\partial y}\right) = 6H\left[1 - u_s^*\right]\left(1 - u_s^*\right)\eta_{true} U \frac{\partial h}{\partial x} = 6\eta U \frac{\partial h}{\partial x} \tag{3.22}$$

Comparison with the classical solution leads to the definition of the dimensionless slip factor introduced previously in equation (3.17), i.e. $f^* = H[1 - u_s^*]\,(1 - u_s^*)$. Furthermore, the "apparent" and "true" viscosities are correlated through the equation

$$\eta = H\left[1 - u_s^*\right]\left(1 - u_s^*\right)\eta_{true} = f^*\eta_{true} \tag{3.23}$$

3.1.3.2: Pressure and Velocity Distributions

The classical solution of the Reynolds equation to obtain the normal (bearing) force is based on the work of Kapitza [78]. Including the slip factor yields the following equation for the pressure distribution:

$$p = -\frac{6 f^* U \eta_{true}}{5} \frac{x}{h^2} = -\frac{24 f^* R^2 U \eta_{true} x}{5\left(2h_0 R + x^2 + y^2\right)^2} \tag{3.24}$$

The full forms of the velocity distributions can be obtained by plugging the pressure gradients $\partial p/\partial x$ and $\partial p/\partial y$ calculated from the above equation into equations (3.20) and (3.21). The normalized velocities can be found as $u^* = u/U$ and $v^* = v/U$, while the x- and y-coordinates can

be normalized as $\xi = x(2h_0R)^{-1/2}$ and $\zeta = y(2h_0R)^{-1/2}$, respectively [78]. Using the half-Sommerfeld boundary condition, i.e. disregarding the pressure distribution for positive ξ and using only the positive pressure (for $\xi < 0$) gives a reasonable estimate of the load-bearing capacity [78]. Even though the half-Sommerfeld conditions violate mass continuity at $\xi = 0$ [78], they can capture the magnitude of the normal force sufficiently accurately and are used in this work. The effect of slip is to decrease the magnitude of the pressure by scaling the distribution. The normalized velocity in the ξ-direction immediately under the sphere ($\xi = \zeta = 0$) is shown in Figure 3.5. Here we can clearly see the two boundary conditions corresponding to no-slip and finite slip: under the effect of interfacial slip, the velocity in the fluid is less than the velocity of the sphere. The thin lines represent the simplified solutions for the velocity distributions where the pressure gradient is neglected; we denote these solutions with the subscript "Couette."

3.1.4: Forces Acting on the Sphere

Half-Sommerfeld conditions are used as boundary conditions of the integration to yield a closed form expression for the normal (bearing) force

$$P_{fluid} = \int_{-\infty}^{+\infty} dy \int_{-\infty}^{0} p\,dx \tag{3.25}$$

The result of the integration given in classical hydrodynamic theory [78] has now been appended for interfacial slip through the slip factor f^*:

$$P_{fluid} = \frac{6\pi}{5} f^* \eta_{true} U \sqrt{\frac{2R^3}{d_0}} \tag{3.26}$$

The shear stress on the surface of the sphere can be calculated as

$$\tau = \eta_{true} \left.\frac{\partial u}{\partial z}\right|_{z=h} = \frac{4RU\eta_{true}}{5} f^* \frac{2d_0R + 7x^2 + y^2}{\left(2d_0R + x^2 + y^2\right)^2} \tag{3.27}$$

The shear force can be calculated by integrating the shear stress over the surface of the sphere

submerged into the lubricant layer. The area of the submerged spherical cap is

$$S = 2\pi \int_{R-(t-d_0)}^{R} R dy = 2\pi R\left(t-\kappa-d_0\right) \tag{3.28}$$

Hence, the shear force is

$$Q_{fluid} = 2\pi \int_{R-(t-\kappa-d_0)}^{R} \tau\big|_{x=\sqrt{R^2-y^2}} R dy \tag{3.29}$$

The full solution is

$$Q_{fluid} = \frac{8\pi U\eta_{true}}{5} f * \frac{\left(t-\kappa-d_0\right)}{\left(2d_0+R\right)^2}\left[2{d_0}^2 - R^2 + 4d_0\left(R-t+\kappa\right) - 6R\left(t-\kappa\right) + 2\left(t-\kappa\right)^2\right] \tag{3.30}$$

Neglecting the pressure gradient in equation (3.20) results in a velocity that includes only the Couette term. Then, calculating the velocity gradient at $z = h$, multiplying with viscosity to find the shear stress, and integrating over the spherical cap surface to find the shear force as was done with equations (3.27) to (3.30), yields the following simplified expression:

$$Q_{fluid,Couette} = 4\pi U\eta_{true} f * R\frac{t-\kappa-d_0}{2d_0+R} \tag{3.31}$$

Hydrodynamic forces can be normalized by dividing through with $U\eta_0 R$ where η_0 is the maximum limiting viscosity at the minimum liquid gap. Figure 3.6 is a comparison of the dimensionless shear force with and without the Poiseuille term (i.e. non-zero and zero pressure gradient respectively). It can be observed that neglecting the pressure gradient and calculating the shear force using a Couette flow approximation [74] underestimates the shear force by two orders of magnitude. While this effect can be expected to diminish away from the bottom of the sphere (i.e. for $\xi = \zeta \neq 0$) as well as at higher shear rates where the Couette term will dominate the Poiseuille term, it cannot be neglected when interpreting the experimental data. Note that the limit of the shear force when the liquid gap d_0 tends to $t - \kappa$ is zero.

Henceforth, the following equations, shown in terms of the measured dynamic "apparent" viscosity $\eta = f^*\eta_{true}$, can be used to calculate the normal and shear forces:

$$P_{fluid} = \frac{6\pi}{5}\eta U\sqrt{\frac{2R^3}{d_0}} \tag{3.32}$$

$$Q_{fluid} = \frac{8\pi U\eta}{5}\frac{\left(t-\kappa-d_0\right)}{\left(2d_0+R\right)^2}\left[2{d_0}^2 - R^2 + 4d_0\left(R-t+\kappa\right) - 6R\left(t-\kappa\right) + 2\left(t-\kappa\right)^2\right] \tag{3.33}$$

3.1.5: Applicability of Force Formulations to Shearing Experiments

The shear force was given earlier as

$$Q_{fluid} = \eta\Omega U \tag{3.7}$$

The geometric factor for a partially-submerged sphere is obtained from equation (3.33) as

$$\Omega_{p-s} = \frac{8\pi}{5}\frac{\left(t-\kappa-d_0\right)}{\left(2d_0+R\right)^2}\left[2{d_0}^2 - R^2 + 4d_0\left(R-t+\kappa\right) - 6R\left(t-\kappa\right) + 2\left(t-\kappa\right)^2\right] \tag{3.34}$$

Correspondingly, the geometric factor used by Fukuzawa *et al.* [44] is based on the work of Goldman *et al.* [75] for a fully-submerged sphere:

$$\Omega_{f-s} = \frac{16\pi}{5}R\ln\left(\frac{d_0}{R}\right) \tag{3.35}$$

Figure 3.7 presents a comparison between the two geometric factors. It can be observed that a fully-submerged formulation corresponds to a geometric factor that is more than three orders of magnitude larger than the partially-submerged equivalent. This is expected, since the shear force acting on a fully-submerged sphere being dragged through a liquid is expected to be larger than if the sphere were only "surfing" on the liquid surface. Since the partially-submerged formulation requires that the film thickness be smaller than the sphere radius, it does not

converge to the fully-submerged sphere. Therefore, special care should be taken to match the experimental conditions to the appropriate shear force formulation.

In their experiments, Fukuzawa *et al.* used a droplet of lubricant as the "reservoir" where the probe is vibrated; the droplet thickness was either about 1 μm in earlier work [30] or sufficient to fully submerge the spherical probe in later experiments [31, 44], i.e. of the order of 200 μm. In either case, the formulation used for the hydrodynamic forces should take into account the fact that the lubricant film does not extent sufficiently in the lateral direction for the full- or half-Sommerfeld boundary conditions [78] to be valid. Specifically, even in the case of a fully-submerged probe and given that the droplet roughly takes the shape of a hemisphere, the diameter of this hemisphere will only be twice the probe diameter, i.e. of the order of 400 μm. As shown previously, full- or half-Sommerfeld conditions require limits of integration for the pressure in the film that tend to infinity in the lateral directions: the limits of integration for the full-Sommerfeld conditions are $-\infty$ and $+\infty$, while half-Sommerfeld conditions require integration between $-\infty$ and zero. Perhaps more importantly, the same consideration holds for the use of the fully-submerged shear force formulation, which requires that the lubricant be treated as a semi-infinite fluid [75]. Hence, the methodology used in Fukuzawa *et al.* [44] is expected to be under-predicting the viscosity. This is because a larger mass of lubricant would provide larger shear resistance than a droplet of the same order of magnitude as the probe.

3.1.6: Estimate of the Hydrodynamic Forces at Higher Shear Rates

The presented model can be used to predict the forces acting on a sphere of any radius R (while $R \gg t$) moving in a lubricant of thickness t with a constant velocity U. As explained previously, expressing the viscosity measurements as functions of shear rate rather than gap allows for the extraction of the "apparent" viscosity at any velocity since we postulate that, for a given lubricant morphology/chemistry, the maximum "apparent" viscosity is bounded in the upper limit by η_0. Therefore, even at shear rates larger than the corresponding limiting shear rate, the "apparent" viscosity will assume this constant limiting value.

In the case of magnetic storage with velocities of ~30 m/s the shear rates in the lubricant will be much greater than those found in the experiments of Fukuzawa *et al.* A simple calculation of the

minimum shear rate for the same lubricant morphology of with total thickness t = 3 nm, and $d_{0,max} = t - \kappa$ = 2 nm, shows this to be ~1×10^{10} s^{-1}, similar to what is reported in the literature [32]. In contrast, the maximum shear rate observed in the shearing experiments for $d_{0,min} = \kappa$ = 1 nm and U = 200 μm/s is much smaller at 1.4×10^{5} s^{-1}. Therefore, in magnetic storage applications we postulate that the maximum viscosity in the lubricant layer is equal to the limiting value of η_0 = 0.31 Pa s.

In magnetic storage, contact at the HDI can be approximated as that between a smooth flat and an equivalent rough surface; the asperities on the latter can be assumed to be spheres with a radius of ~500 nm [10, 11, 13]. Using the presented sphere-on-flat formulation, the resulting hydrodynamic forces acting on a single asperity will be as shown in Figure 3.8. Lubricant contact is valid only up to the total lubricant film thickness of 3 nm, and, equivalently, up to $d_{0,max}$ = 2 nm. Both forces are increased relative to the reported experimental values [44] by about two orders of magnitude stemming from a five order of magnitude increase in shearing velocity from 200 μm/s to 30 m/s. Even though the forces are linearly dependent on the shearing velocity, the correspondence is not one-to-one due to the effect of the viscosity, which is capped at the value of η_0 at higher shear rates. Note that using the bulk value of the viscosity results in significant under-prediction of the hydrodynamic forces as shown in Figure 3.8. In fact, the shear force is practically zero (data lies on the x-axis) if the bulk viscosity is used.

For a given set of material parameters for DLC, the minimum solid forces were calculated to be $P_{solid,min}$ = 1.5 μN and $Q_{solid,min}$ = 120 μN for ω = 1 Å, and 40 μN and 1,120 μN for ω = 1 nm as shown earlier. These magnitudes are comparable to the hydrodynamic forces developed for the sliding speeds encountered in HDDs. Therefore, previous models where the lubricant was assumed to offer no resistance to shearing and was simply displaced during contact [10, 11, 13] need to be corrected to account for lubricant contact. More importantly, it seems possible that the bearing capacity of the MTL could benefit the interface by protecting the DLC coating from light contact.

3.1.7: Decoupling Viscosity Stiffening and Interfacial Slip

Simultaneous measurement of the normal and shear forces with the dynamic “apparent” viscosity

can be used to decouple viscosity stiffening from interfacial slip. However, in the absence of such data, another way to decouple the two effects is to use molecular dynamics simulation data. For example, Martini *et al.* report that the slip length L_s for velocities larger than ~8 m/s is constant at ~3 nm [37]. Even though simulations pertaining to the exact lubricant morphology/chemistry are necessary for a more accurate estimate of the slip length, we shall assume that L_s = 3 nm is valid in this work for the purpose of demonstrating the procedure.

The dimensionless slip factor f^* can be calculated from equations (3.14) and (3.17). As a first approximation, the wall friction η_w can be assumed to be unity. Knowing f^* allows for the extraction of the "true" viscosity from equation (3.23) and the "true" shear rate from equation (3.18). These calculations result in f^* becoming zero – corresponding to unbounded slip – at $d_0 \approx$ 2.5 nm and η_{true} tending to infinity at the same liquid gap value. This is an artifact arising from the arbitrary assumption that the wall friction is unity. The minimum liquid gap of $d_{0,min}$ = 1 nm corresponds to a maximum ratio of slip length to liquid gap L_s/d_0 = 3. Since unbounded slip is unrealistic, we can constrain f^* such that it is larger than zero at the minimum liquid gap by tuning the wall friction η_w accordingly; taking η_w = 3 results in the slip factor becoming zero. Figure 3.9(a) shows plots of the "true" viscosity and slip factor as functions of gap for the given parameter values of L_s = 3 nm, $d_{0,min}$ = 1 nm and η_w = 3.

The plots of Figure 3.9(a) represent the lower limit of the wall friction where the "true" viscosity again tends to infinity as f^* tends to zero. As is shown in Figure 3.9(b), if the wall friction η_w is increased to a value of 5, the maximum "real" viscosity becomes only 2-3 times larger than the maximum "apparent" viscosity and the slip factor ranges between ~0.4 and unity. In the upper limit of $\eta_w \rightarrow \infty$ (not shown), the "true" and "apparent" viscosities become the same and f^* is everywhere 1, resulting in the no-slip boundary condition: only viscosity stiffening happens in this case.

It is obvious that the exact values of the "true" viscosity and interfacial slip as functions of the liquid gap are very sensitive to the interaction between the bonded molecules and the substrate, i.e. to the value of the wall friction η_w. Based on the proposed models and methodology, the following appears to hold for the wall friction: $L_s/d_{0,min} \leq \eta_w < \infty$. Therefore, we can say that lubricants confined in molecularly thin gaps and sheared at high speeds either exhibit the

confounded effects of both stiffening and slip as the wall friction tends to the lower limit of $L_s/d_{0,min}$, or stiffening overtakes slip as the wall friction tends to infinity.

3.2: SLIDING CONTACT OF ROUGH SURFACES WITH MTL LAYERS

3.2.1: MTL on Rough Substrates

Polymeric lubricant sputtered onto hydrogenated carbon overcoats would be expected to smooth out the solid substrate (carbon) surface due to surface tension. Various effects, such as thermally excited capillary waves [82] and "lubricant moguls" [80, 83], as well as the lubricant thickness itself [84] contribute to the experimentally measured roughness and need to be accounted for within the context of lubricant contact. The ISBL model [10, 45] addresses some of these issues by utilizing experimental measurements of roughness under both static and dynamic conditions. The GW model is used to model roughness in the ISBL model and approximates rough surface contact as that between a rough surface of equivalent roughness and a rigid, nominally flat surface [58]. For a discussion on the applicability and limitations of the GW approximation and similar approaches used to model roughness the reader is referred to the extensive literature available on the subject [85-89]. In static measurements of roughness, the sharp AFM tip experiences a meniscus force when brought into proximity with the lubricant layer because of lubricant transfer to the tip [82]; this effect would be larger for thicker films and would affect adhesion. For molecularly thin films, meniscus formation is deemed unfavorable and a Lenard-Jones-type surface potential is used to calculate adhesion; nevertheless, the resulting formulation for the adhesive force on one asperity is equivalent to that of the meniscus force [28, 45, 49]. Lubricant density was found to reach that of air at a distance of about 3σ away from the average lubricant thickness [82]. This validates the approach of the ISBL model [10, 45] – also adopted in the present work – that the lubricant layer of average thickness t follows the rough topography of its substrate, 99.7% of which would be encompassed within 3σ from the mean of surface heights [10].

Figure 3.10 shows a schematic of the topography of a rough solid substrate coated with an MTL layer. The bonded lubricant layer thickness is defined as the solid-solid gap where the lubricant forces reach their maxima and beyond which continuum breaks down (for smaller gaps). In Figure 3.10, the combined roughness (from the two solid surfaces) is placed on the bottom substrate as are, similarly, both bonded lubricant layers. This critical gap can be calculated from available data on specific lubricant chemistry/morphology and quantified in terms of the

minimum film thickness κ [23]. A second rough surface that comes into contact with lubricant deposited on a rough substrate is expected to pick up and bond with some of the lubricant molecules. Since each of the rough surfaces would feature a layer of bonded molecules having an average thickness of κ, the closest that the two surfaces could come together before the rupturing of the bonded layers and solid contact would be 2κ. Depending on the treatment of the original substrate, the thickness of the bonded layer could be different on each surface; for a discussion on the calculation of κ in this case, the reader is referred to previous work by the authors [23]. Therefore, during lubricant contact and in terms of average thicknesses, the total lubricant layer of thickness t will contain a bonded lubricant layer of thickness 2κ and a mobile lubricant layer of thickness $t - 2\kappa$. This approach is similar to the one used in the ISBL model [10, 45], except that the bonded layer thickness is not taken arbitrarily to be half the total layer thickness.

Even though the distinction is not very clear in reality, for the purposes of our model we use the bonded lubricant layer as the reference surface. The bonded lubricant layer then has the same roughness as the solid substrate but its mean of surface heights is shifted up by 2κ. The mobile lubricant molecules are assumed to share the same roughness characteristics except from the RMS roughness, which would be larger by virtue of thermally excited capillary waves; hence, the mobile lubricant layer surface would have a mean shifted from that of the solid substrate by an amount t equal to the total average lubricant thickness and an RMS roughness shifted from that of the solid and bonded layers by few Angstroms [82]. This latter shift (of the RMS roughness) is adequately captured in the measurements of the dynamic microwaviness (DMW), i.e., the dynamic modulation of the rotating disk. Therefore, no real deviations are necessary from the ISBL model formulation [10, 45] except to define the bonded layer thickness $T_0 = 2\kappa$. For example, the minimum liquid gap for perfluoropolyether (PFPE) lubricants could be of the order of the molecules' radius of gyration, $r_g = 0.3$ nm [41]. Then, the average bonded layer thickness would be $T_0 = 2r_g = 0.6$ nm, which would be roughly half the average total lubricant thickness for a typical magnetic storage disk ($t = 1.5$ nm). This is similar to the assumption made in the ISBL model [10, 45].

3.2.2: Stiffness of MTL Layers

Displacement-control in dynamic shearing experiments [44] results in three distinguishable

contact regimes: steady lubricant contact, steady solid contact and transition between the two. The latter regime is thought to confound the initiation of solid (asperity) contact and the rupturing of the bonded lubricant layers [23].

Figure 3.11 is a schematic of the transitional contact regime, separated into bonded lubricant layer rupture (2κ) and solid asperity contact (3σ) phases, where the plotted quantity could be either force or stiffness. While this decoupling is unrealistic since both events could be occurring simultaneously in displacement-control experiments, it is useful in differentiating between lubricant and solid contact. Let h be the separation between the means of surface heights of the two solid surfaces. Solid contact occurs when $h < 3\sigma$ where σ is the combined RMS roughness of the interface; note that the separation during solid contact is also termed interference [10]. Correspondingly, hydrodynamic forces are meaningful in the range of solid-solid gaps $2\kappa \leq h_0 < t$ [23]. This range can be expressed in terms of the mean plane separation as $3\sigma+2\kappa \leq h < 3\sigma+t$. The intermediate range of $3\sigma \leq h < 3\sigma+2\kappa$ contains the rupture and expulsion of the bonded lubricant layers and could not be clearly defined, neither in experiments or simulations. In the absence of displacement-control, one would argue that the bonded lubricant layers would offer no resistance once ruptured and would be expelled from the interface until solid asperity contact occurred. However, to avoid discontinuities, we can assume that the bonded lubricant layers would resist compression and shear up to certain point beyond which the strength of the layer goes to zero just before the inception of solid asperity contact. Therefore, in the range of $3\sigma \leq h < 3\sigma+2\kappa$ a linear approximation can be used for the lubricant layer strength.

The preceding discussion raises new questions: What is the "strength" of the lubricant layer? Is this "strength" independent of shear rate? Under certain experimental conditions, lubricant forces are maximized when the solid-solid gap becomes equal to 2κ (or $d_0 = d_{0,min} = \kappa$) and would depend on lubricant morphology and chemistry [23]. This critical gap corresponds to the maximum experimental value of the viscosity $\mu = \mu_0$ (changed from the notation of the sphere-on-flat model so as not to be confused with the coefficient of friction) and, in turn, to a critical shear rate equal to the ratio U/κ where U is the average linear shearing velocity. But, what happens for shear rates larger than the experimentally observed critical shear rate? For example, the shearing velocities in magnetic storage would be of the order of tens of m/s while the

experimental value is 0.2 mm/s [44]. This would result in shear rates that are at least five orders of magnitude larger than what can be attained in the experiments. What would then be the lubricant behavior is unclear; some discussion on these critical issues follows.

Researchers have reported that under very high shear rates and confinement, MTLs exhibit solid-like behavior [31, 32, 41, 69, 70, 90]. Moreover, in a solid-like lubricant film, hysteresis or loss of energy would be small to nonexistent [76]. Therefore, it should be reasonable to model an MTL film under high shear rates as having normal and shear stiffnesses that are functions of the shear rate with zero damping. To investigate this, let us extrapolate the lubricant forces beyond the critical (experimentally observed) shear rate by substituting for the liquid gap in the original expressions for the normal and shear forces P_{lube} and Q_{lube} acting on a fully-submerged sphere sliding parallel to a rigid substrate [23, 44]:

$$P_{\text{lube}} = \frac{6\pi}{5}\mu\sqrt{2UR^3\dot{\gamma}} \tag{3.36}$$

$$Q_{\text{lube}} = \frac{16\pi}{5}\mu UR\ln\left(\frac{U}{\dot{\gamma}R}\right) \tag{3.37}$$

These forces are dependent on the viscosity μ, the shearing velocity U, the sphere radius R, and the shear rate $\dot{\gamma}$. In the absence of available data, let us assume that the viscosity is equal to the maximum experimental value for shear rates larger than the critical, i.e., $\mu = \mu_0$. The experimental parameters are: maximum viscosity μ_0 = 0.31 Pa s; shearing velocity U = 200 μm/s; radius of spherical shearing probe R = 102 μm [44]. Then, the critical shear rate is $U/\kappa = 2\times10^5$ s^{-1} for κ = 1 nm [23]. The maximum experimental normal and shear forces are 10.77 μN and 0.73 μN respectively. These can be denoted as P_0 and Q_0 for future reference; they can also be calculated as functions of the minimum liquid gap κ rather than the shear rate as

$$P_0 = \frac{6\pi}{5}\mu_0 U\sqrt{\frac{2R^3}{\kappa}} \tag{3.38}$$

$$Q_0 = \frac{16\pi}{5}\mu_0 UR\ln\left(\frac{\kappa}{R}\right) \tag{3.39}$$

Lubricant forces are plotted as functions of the shear rate for the given experimental conditions in Figure 3.12. Using equations (3.36) and (3.37), the shear rate is varied over six orders of magnitude between 10^5 and 10^{11} s^{-1} beyond the critical experimental value. For simplicity, the viscosity is taken to be equal to μ_0 for the entire range since the shear rates of interest are closer to 10^{10} s^{-1} as found in magnetic storage. The forces at the critical shear rate of 2×10^5 s^{-1} are equal to P_0 and Q_0 while both forces increase with increasing shear rate. While the shear rate is lower than the critical value, the lubricant layer should be able to sustain shearing and compressive forces until the limiting solid-solid gap of 2κ. For larger shear rates, we would indeed expect an increase in both forces over a smaller range of solid-solid gaps, which would be limited by the film thickness regardless. Therefore, the trends shown in the extrapolated forces for larger shear rates as shown in Figure 3.12 are physically possible.

Upon closer inspection of equations (3.36) and (3.37) as well as the trends of Figure 3.12, it appears that simple expressions can be fitted to the extrapolated forces over the range of shear rates investigated. This is shown in Figure 3.13 where the normal force is shown in a log-log plot (a) and the shear force (same as in Figure 3.12) is shown in a log-linear plot (b). The fitted expressions are given as functions of the shear rate and the maximum experimental conditions:

$$P_{\text{lube}} = P_0\left(\frac{\dot{\gamma}}{\dot{\gamma}_0}\right)^m \tag{3.40}$$

$$Q_{\text{lube}} = n\log\left(\frac{\dot{\gamma}}{\dot{\gamma}_0}\right) + Q_0 \tag{3.41}$$

The fitting coefficients m and n are calculated from the slopes of the log-log and log-linear plots of the normal and shear forces respectively. They can be calculated using the equations

$$m = \frac{\log\left(\frac{P_{\text{lube},2}}{P_{\text{lube},1}}\right)}{\log\left(\dot{\gamma}_2 / \dot{\gamma}_1\right)} \tag{3.42}$$

$$n = \frac{Q_{\text{lube},2} - Q_{\text{lube},1}}{\log\left(\dot{\gamma}_2 / \dot{\gamma}_1\right)} \tag{3.43}$$

The fitting coefficients are 0.5 and 1.46×10^{-7} respectively for the given experimental parameters. When the shear rate is equal to the maximum experimental value, their ratio becomes unity and equations (3.40) and (3.41) simplify to $P_{lube} = P_0$ and $Q_{lube} = Q_0$. Equations (3.40) and (3.41) can be expressed again as functions of the liquid gap d0 by substituting the shear rate as U/d_0 for the new shearing velocity under investigation. Then the normal and shear stiffnesses are calculated as

$$k_P = \left|\frac{\partial P_{\text{lube}}}{\partial d_0}\right| = \underbrace{mP_0\left(\frac{U}{\dot{\gamma}_0}\right)^m}_{\text{constant}}\left(\frac{1}{d_0}\right)^{m+1} \tag{3.44}$$

$$k_Q = \left|\frac{\partial Q_{\text{lube}}}{\partial d_0}\right| = \underbrace{\frac{n}{\ln(10)}}_{\text{constant}}\left(\frac{1}{d_0}\right) \tag{3.45}$$

Substituting once again the liquid gap d_0 with the shear rate gives the following expressions for the normal and shear stiffnesses:

$$k_P = \frac{mP_0}{U\dot{\gamma}_0^{\,m}}\dot{\gamma}^{m+1} \tag{3.46}$$

$$k_Q = \frac{n}{U\ln(10)}\dot{\gamma} \tag{3.47}$$

It should be stressed that equations (3.40)–(3.47) are valid only for shear rates larger than the maximum experimental shear rate of 2×10^5 s^{-1}. Hence, for the same value of κ = 1 nm, the shearing velocity U should be larger than the experimental value of 200 μm/s to achieve larger shear rates. On the other hand, if the minimum liquid gap was smaller than the experimental value, for example equal to the radius of gyration $\kappa = r_g$ = 0.3 nm, then the critical shear rate of 2×10^5 s-1 would be exceeded for shearing velocities larger than 60 μm/s. In magnetic storage, HDDs operate at speeds between 7,200 and 10,000 RPM. For a 2.5 inch disk diameter, the linear velocities could be as high as 30 m/s on the outer diameter. Taking a moderate value for the velocity, say 15 m/s, we can use equations (3.46) and (3.47) to calculate the normal and shear stiffnesses as functions of the shear rate as shown in Figure 3.14.

Only a small range of shear rates is of interest in MTLs. For example, the minimum and maximum shear rates occurring in a lubricant layer of thickness t = 1.5 nm and minimum liquid gap of $\kappa = r_g$ = 0.3 nm can be calculated using the following equations:

$$\dot{\gamma}_{\min} = \frac{U}{t-\kappa} \tag{3.48}$$

$$\dot{\gamma}_{\max} = \frac{U}{\kappa} \tag{3.49}$$

The shear rate is defined as the ratio of shearing velocity to the liquid gap, which is the effective thickness of the mobile lubricant molecules at the interface.

For the given operating conditions and lubricant morphology, the shear rate of interest would range between 1.5×10^{10} and 6×10^{10} s^{-1}. Correspondingly, the stiffnesses would range between 1.23×10^6 to 9.83×10^6 N/m and 52.98 to 211.94 N/m for the normal and shear components respectively as shown in Figure 3.15(a) and (b). Experiments measuring the contact stiffness on magnetic disks have reported that, for normal loads smaller than 100 mN, the measured stiffness is limited at 3×10^5 N/m [91]. While these experiments were performed under static conditions, the reported normal stiffness is not far from the value we calculate here, if it indeed corresponds to that of the lubricant and is not confounded with early asperity contact as well. Perhaps more

importantly, it would appear that lubricant stiffness under compression would be comparable to the solid contact stiffness for sufficiently high shear rates and the MTL could offer some protection to the substrate.

When aiming to integrate the normal and shear stiffnesses into a model such as the ISBL contact/friction model, it would be desirable to express them as functions of the liquid gap d_0 as shown in Figure 3.16. Corresponding to the minimum and maximum shear rates calculated using equations (3.48) and (3.49), the liquid gaps of interest in a molecularly thin film with total average thickness t = 1.5 nm and minimum liquid thickness κ = 0.3 nm are within the range $\kappa \leq d_0 < t - \kappa$, i.e., 0.3 nm $\leq d_0 <$ 1.2 nm. Hydrodynamic forces are not defined outside of this range. The stiffnesses would go to the solid values for $h = 3\sigma$ over the range of $3\sigma \leq h < 3\sigma+2\kappa$ and solid contact would occur for $h < 3\sigma$.

3.2.3: Rough Surface Solid and MTL Contact Model with Friction

3.2.3.1: Model Formulation for Variable Surface Energy

The ISBL model [45] addresses the contact with friction of two nominally flat surfaces by coupling finite element solutions of dry, unlubricated frictional contact [92] with the original SBL model [28]. In addition to the contact and friction forces, the finite element-based model of Kogut and Etsion (KE) includes the adhesive contributions for non-contacting as well as elastically and elastically-plastically contacting asperities [92]. The SBL model's formulation of adhesion during lubricant contact was combined with the KE model in the ISBL model [45], but does not account for the variation of surface energy with lubricant penetration that was recently observed in experimental measurements [46]. Hence, we introduce a variable surface energy intro the adhesion formulation according to the following equation:

$$\Delta\gamma = \Delta\gamma\left(h_0\right) = c_1 \exp\left(-c_2 t\right) + c_3 \tag{3.50}$$

Fitting coefficients c_1, c_2 and c_3 can be extracted from experimental measurements: these are 42.84 mN/m, 2.41 nm^{-1} and 14.54 mN/m respectively. Figure 3.17 shows the total surface energy as a function of the total lubricant thickness [46]. The exponential form of equation (3.50)

yielded better fitting than a polynomial fit.

The adhesive force during lubricant contact can be adapted from the ISBL model as [45]

$$F_{s,lube} = 2\pi RN\left[\int_{-\infty}^{d-t} J_{nc} + \int_{d-t}^{d} J_{lc}\right] \tag{3.51}$$

The integrands for non-contacting and lubricant-contacting asperities are

$$J_{nc} = \frac{4}{3}\min(\Delta\gamma)\left[\left(\frac{\varepsilon}{\varepsilon - t - d - z}\right)^2 - 0.25\left(\frac{\varepsilon}{\varepsilon - t - d - z}\right)^8\right]\phi(z)\,dz \tag{3.52}$$

$$J_{lc} = \left\{c_1 \exp\left[-c_2(d - z)\right] + c_3\right\}\phi(z)\,dz \tag{3.53}$$

A total of *N* asperities having radius R are distributed with Gaussian distribution φ (*z*) about the mean. The distance between the means of asperity heights of the two rough surfaces is *d*, and *t* is the average lubricant layer thickness. The equilibrium spacing ε is defined as the spacing where adhesion is maximized. Adhesion for non-contacting asperities is based on the Lennard-Jones surface potential and uses the minimum surface energy measured at the lubricant layer surface. The formulation for the adhesive force on lubricant-contacting asperities is equivalent to the meniscus force [49]; however, meniscus formation is deemed energetically unfavorable [28, 45]. The surface energy term is updated to account for its variation with penetration within the lubricant layer. The remaining integrands in the contact, friction and adhesive force formulations pertaining to solid contact remain as in the KE/ISBL model [45, 92]. The roughness and material parameters used in the simulations are summarized in Table 3.2 [46].

Figure 3.18(a) shows an adjusted plot of the surface energy as a function of the dimensionless separation (i.e., normalized with the combined RMS roughness σ). The variable surface energy model of equation (3.50) is expressed as a function of the separation rather than the lubricant thickness. The maximum surface energy corresponds to the dimensionless equilibrium spacing ε (shown as the vertical dotted line in the figure) and equation (3.50) describes its behavior for $h > \varepsilon$. For separations smaller than the equilibrium spacing, the surface energy is constant at its

maximum whereas the adhesive force increases as more asperities are brought into solid contact as shown in Figure 3.18(b). Since the surface energy is not constant at its maximum (as was used in previous models), the total adhesive force is lower in magnitude while it reaches the expected maximum more abruptly at $h = \varepsilon$.

3.2.3.2: Total Contact, Friction and Adhesive Forces

The ISBL model can be used to calculate the contact and friction forces P and Q as functions of the separation h [10, 45]. Beginning with the normal contact force and to calculate the dynamic contact force, the contact stiffness of the original ISBL model is

$$k_c = \left| \frac{\Delta P}{\Delta h} \right| \tag{3.54}$$

The derivation of the quasi-static contact force P can be found in the literature [45, 53]. The stiffness of equation (3.54) is valid for $0 < h < 3\sigma$. During lubricant contact, the normal stiffness was derived previously and is given by equation (3.46). It is valid for the range of separations $3\sigma+2\kappa \leq h < 3\sigma+t$. In terms of the mean plane separation, the shear rate can be expressed as

$$\dot{\gamma} = \frac{U}{d_0} = \frac{U}{h - 3\sigma - \kappa} \tag{3.55}$$

Therefore, equation (3.46) can be expressed as

$$k_P = \frac{mP_0}{U\dot{\gamma}_0^{\,m}} \left(\frac{U}{h - 3\sigma - \kappa} \right)^{m+1} \tag{3.56}$$

The transitional stiffness over the intermediate range of $3\sigma \leq h < 3\sigma+2\kappa$ can be calculated as

$$k_{c-P} = \left| \frac{k_P\left(\dot{\gamma} = \dot{\gamma}_{\max}\right) - k_c\left(h = 3\sigma\right)}{2\kappa} \right| h \tag{3.57}$$

The stiffness in this intermediate range will vary from the maximum normal lubricant stiffness at the maximum shear rate to the value of k_c at $h = 3\sigma$. Similarly, the shear and friction forces can be combined over the applicable range of separations. Let us denote the frictional stiffness as k_{fr}. This will be

$$k_{fr} = \left| \frac{\Delta Q}{\Delta h} \right| \tag{3.58}$$

The frictional stiffness k_{fr} will be valid over the range $0 < h < 3\sigma$. The shear stiffness, given in equation (3.47), is correspondingly valid for $3\sigma+2\kappa \leq h < 3\sigma+t$ and is given, in terms of separation as

$$k_Q = \frac{n}{\ln(10)} \left(h - 3\sigma - \kappa \right)^{-1} \tag{3.59}$$

Finally, the transitional stiffness valid over the intermediate range will be given by

$$k_{fr-Q} = \left| \frac{k_Q \left(\dot{\gamma} = \dot{\gamma}_{\max} \right) - k_{fr} \left(h = 3\sigma \right)}{2\kappa} \right| h \tag{3.60}$$

Numerically, the transitional stiffnesses can be added to their solid counterparts such that the maximum lubricant stiffnesses will lead to the stiffnesses at the inception of solid contact. This is shown in Figure 3.19: the lubricant and transitional stiffnesses are combined over the range of separations larger than 3σ; the solid stiffnesses are shown for separations smaller than 3σ; finally, the combined stiffnesses are plotted over the entire range of separations leading from lubricant to solid contact. Note that the overall behavior of the stiffnesses resembles the trend shown in Figure 3.11, while the lubricant stiffnesses are zero beyond the total average lubricant thickness.

The normal lubricant stiffness is 4-5 orders of magnitude larger than the shear lubricant stiffness. Nevertheless, the total stiffnesses comprising solid and lubricant contributions are more comparable as shown in Figure 3.19: the maximum normal stiffness during lubricant contact (at $h^* = 3.73$) is 9.19×10^6 N/m; the lateral stiffness at the same dimensionless separation is 1.20×10^6

N/m. This occurs because lubricant stiffness dominates the normal stiffness while solid stiffness dominates the lateral stiffness at that value of dimensionless separation. The lateral component becomes insignificant during "pure" lubricant contact. It should be noted that, while the choice of a nominal area of 2,500 μm^2 is too large for today's systems yielding very large solid forces, this, along with the material and roughness parameters, were adopted from Yeo *et al.* [46] for consistency with their surface energy data and comparison with their friction measurements.

3.2.4: Results and Discussion

Using the proposed MTL dynamic contact model, normal and lateral stiffnesses were calculated and are comprised with contributions from lubricant and solid contact over a range of penetrations into the solid substrate. Penetration ω is defined relative to the solid substrate as the case when the mean plane separation becomes smaller than 3σ [10, 19, 45]. Hence, positive penetration denotes solid contact while negative penetration denotes lubricant contact for $|\omega| < t$ and non-contact beyond that value. These regimes of contact were also shown in Figure 3.11.

The modeled normal and lateral stiffnesses are plotted in Figure 3.20(a) and (b) as functions of penetration. The shaded portion corresponds to the lubricant thickness of 1.5 nm and highlights lubricant contact, referred to as "surfing" recording [10, 13]. While the normal stiffness of the lubricant is substantial relative to the solid, the lateral stiffness starts from being comparable in magnitude close to the transition from solid to lubricant contact and gradually becomes insignificant (4-5 orders of magnitude smaller than the normal stiffness) during "purely" lubricant contact. This situation would presumably change for polar PFPE lubricants that would exhibit a stiffer response.

From the stiffnesses, we can calculate the forces for a range of penetrations. For positive penetrations, i.e., solid contact, the forces are those predicted by the ISBL model. The present MTL dynamic contact model adds non-zero contact and friction forces within the lubricant thickness as shown in Figure 3.21(a) and (b). A small range of solid (positive) penetrations was chosen to represent the "inception" of solid contact.

Similarly to Figure 3.20 and the discussion pertaining to the stiffness results, it becomes evident

from the plots of the normal and friction forces of Figure 3.21(a) and (b) that the presence of an MTL layer affects the normal contact force but has a negligible contribution to friction. However, this is expected to not be the case for smaller contacts, such as those found in today's HDDs, where the solid forces would be significantly smaller. Nevertheless, the presence of MTL layers seems to be beneficial in that it offers some bearing to normal loading but does not prohibitively increase friction.

The detrimental effect of using MTL layers is adhesion. As shown in Figure 3.21(c), the total adhesive force for variable surface energy increases monotonically from non-contact to lubricant and solid contact with penetration and is non-zero and significant even for non-contact. Since the surface energy increases with increasing MTL penetration and does not remain constant at the maximum value as was previously assumed, there is higher potential for operation close to or within the mobile lubricant layer as proposed in previous work [10, 13]. Lower adhesive forces close to the lubricant layer surface could reduce the jump-to-contact behavior, allowing for smaller operating clearances with reduced vibrations.

In the absence of molecular thin lubrication, non-zero contact and friction forces are expected when the separation between the means of the two rough surfaces becomes smaller than 3σ encompassing nearly all the asperities, especially after mild burnishing. The presence of lubricant practically means that non-zero contact and friction forces exist for a larger range of separations equivalent to $3\sigma+t$, increased by the average thickness of the MTL layer. The presence of lubricant effectively decreases the net clearance between two rough surfaces by an amount t and, more significantly, results in smaller resistance to shear within lubricant contact. Hence, it can be said that the disk lubricant effectively reduces the strength of contact junctions as was found in experiments [47].

The exact effect of MTL layers on friction is expected to vary with lubricant chemistry and environmental conditions. For example, adsorbed species will dictate lubricant thickness, coverage and mobility [93, 94]; in turn, these properties will affect the minimum liquid gap κ, which we associate with the radius of gyration of the lubricant molecule in the present model, and the maximum viscosity μ_0. Films of smaller thickness are expected to exhibit larger adhesive forces due to the proximity of the solid substrate and increase friction. Humidity, for example in

the case of Zdol on amorphous carbon overcoats, results in increased lubricant mobility [95]. Similarly, increasing temperature increases mobility while de-bonding is observed near a critical temperature that is higher for clustered end groups [96]. Re-bonding should occur through lubricant reflow, which would depend on mobility; desired MTL behavior could be geared towards either of the two behaviors [97]. Overall, the effects of chemistry and environmental conditions are expected to be captured in the experimental results to be used as inputs in the model. However the larger contributor to friction at the interface is solid asperity interaction [46].

3.2.4.1: Generalization of Proposed Model

Available experimental methods [44] cannot presently achieve the shear rates occurring in magnetic storage applications. Hence, while the extrapolation used in the proposed model is far from the experimental data, the proposed approach is the first to provide usable data on MTL stiffness based on physical formulations of lubricant contact. In the absence of further experimental data, some assumptions were made regarding MTL properties and the results are shown in Figure 3.22. Specifically, the four cases plotted in the figure are:

- Case 1: This is used as the reference case and uses parameters extracted from published experimental work [44] and assumes that the minimum liquid gap is equal to the radius of gyration of 0.3 nm. Previous figures utilize these parameters.

- Case 2: This is used to examine the effect of increasing humidity and temperature, which results in increased lubricant mobility. Here we assume that the maximum viscosity obtained in experiments with controlled humidity and temperature is 50% smaller than the reference case.

- Cases 3 and 4: These are used to examine lubricant stiffening under the effect of increased bonding and/or different lubricant chemistry. To achieve this, we assume that the minimum liquid gap and maximum viscosity observed in experiments are both 50% larger than in the reference case. We also assume that the bonded layers can be compressed to one radius of gyration as before; however, for case 3, the radius of

gyration is the same as in the reference case while, for case 4, this is increased by 50% to 0.45 nm.

The results of Figure 3.22 show that increasing humidity and temperature (case 2) would reduce the maximum bearing force of the lubricant relative to the reference case (1). Conversely, increased bonding (cases 3 and 4) would increase the stiffness and the bearing force. Interestingly, increasing the molecular radius of gyration (by altering lubricant chemistry as shown for case 4) reduces the load bearing capacity of the lubricant since the mobile layer is depleted at smaller penetration: such a lubricant layer cannot sustain as large a shear rate compared to the reference configuration. Is should be noted that the hydrodynamic shear force remains negligible for all these cases and is not plotted.

3.2.4.2: Experimental Comparison

In measurements of friction at the HDI and their comparison to the ISBL model [47], it was found that friction was overestimated in the ISBL model because lubricant contact was neglected. This is consistent with the expected effective decrease of shear strength in the presence of lubricant as mentioned previously. More importantly, it was found that lubricant expulsion from the interface occurred at a contact force of ~5 mN [47, 62]. When examining the close-up of the contact force as a function of penetration plot in Figure 3.22 for the reference case (1), one can observe that the maximum normal lubricant force predicted in the present MTL dynamic contact model is 5.54 mN. This value is close to the reported experimental value that was measured with an interface of comparable material and roughness properties and the proposed model compares favorably to experiments of friction at the HDI. More importantly, the presence of a lubricant bearing could indeed be beneficial for the protection of the interface.

3.3: SUMMARY

A description of the morphology and behavior of MTL films was presented that can explain the experimental results obtained from dynamic shearing experiments based on the available literature [23]. Models have been proposed that account for viscosity stiffening and interfacial slip. The validity of using the dynamic viscosity measured in shearing experiments has been discussed and an improved formulation has been proposed for the shear force acting on a partially submerged sphere shearing a thin lubricant film. “Apparent” viscosity data were used to predict the hydrodynamic forces acting during lubricant contact found in the HDI of HDDs and these were compared to the forces developed during solid-solid contact.

Subsequently, a mechanistic-based model was proposed that accounts for (a) contact with an MTL layer between two rough surfaces and (b) the variation of surface energy within the lubricant layer [24]. Lubricant contact was shown to be more important in the normal direction where it is possible that some of the loading could be contained within the lubricant layer without damage to the solid substrate. Polar lubricants should exhibit even larger normal stiffnesses and should be more beneficial for this purpose. The lateral stiffness during lubricant contact is negligible for the non-polar lubricant investigated but could be more substantial for polar lubricants. The proposed model yields normal and shear lubricant stiffness components and could be incorporated into any existing model of dry contact, other than the ISBL model used in this work.

Adhesion was also investigated for MTL layers. Its formulation was updated from the ISBL model to account for variation in the surface energy with penetration into the lubricant. The maximum adhesive forces were attained during solid contact and correspond to the previous formulation; however, the adhesive force was shown to have a generally smaller magnitude during lubricant contact than the case of constant surface energy. This should result in milder jump-to-contact behavior. Model predictions were compared favorably to available experimental data. More importantly, the lubricant bearing predicted in the proposed model could be beneficial at the interface and could be utilized to reduce wear and damage to the solid substrate.

3.4: FIGURES

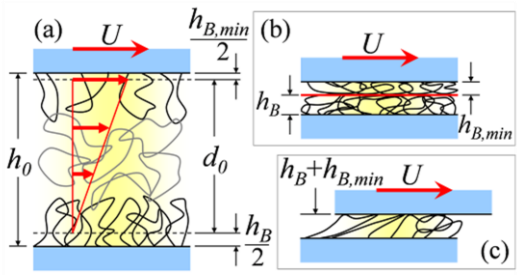


Figure 3.1: Physical description of confined lubricant molecules: (a) shearing for $h_0 > h_{0,min}$; (b) shearing between bonded layers corresponding to maximum viscosity and shear rate; and, (c) lubricant layer rupture and transition from lubricant to solid contact.

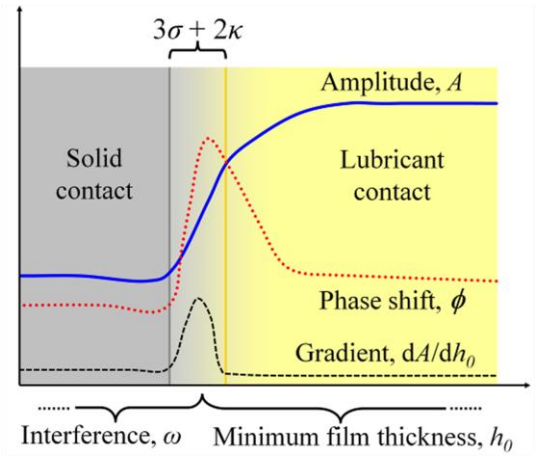


Figure 3.2: Regimes of contact; figure adapted from experimental results of Itoh *et al.*

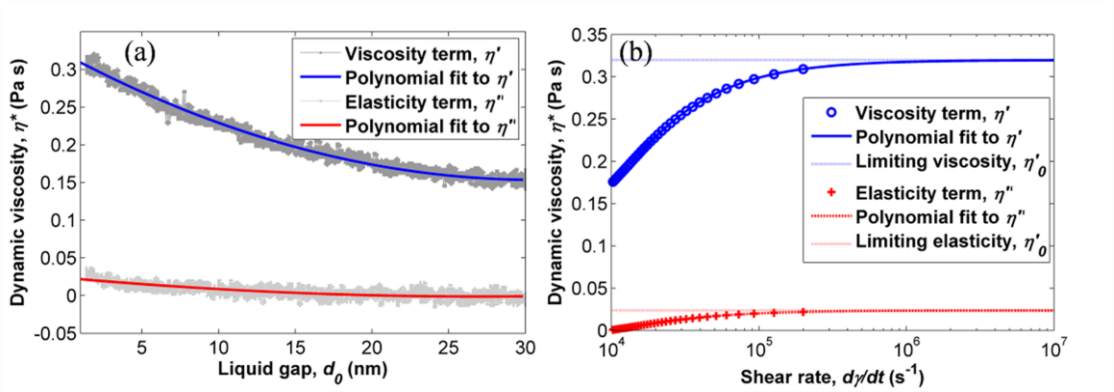


Figure 3.3: Viscosity data capture from Fukuzawa *et al.* [20] as a function of gap with second-order polynomial curve fits ($d_{0,min} = \kappa = 1$ nm); (b) viscosity data as function of shear rate.

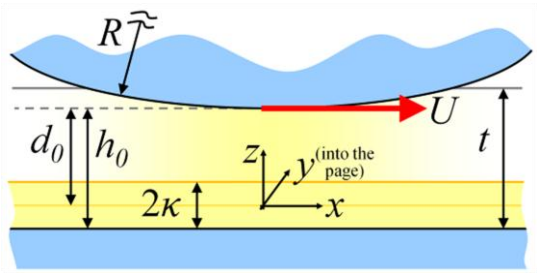


Figure 3.4: Rigid smooth sphere moving in a viscous fluid of thickness *t* parallel to a plane.

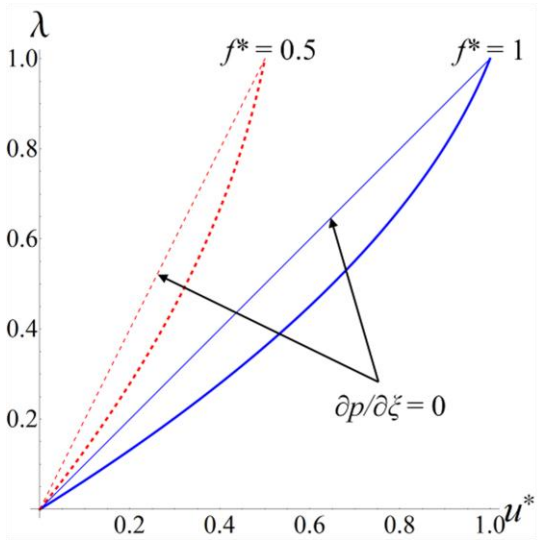


Figure 3.5: Normalized velocity immediately under the sphere for no-slip and finite slip conditions.

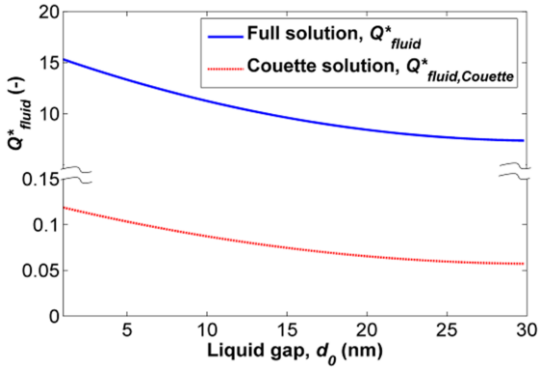


Figure 3.6: Comparison of shear force calculations with full and Couette solutions.

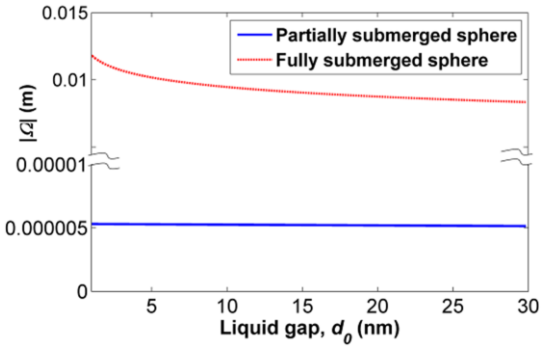


Figure 3.7: Comparison of geometric factors for fully and partially submerged spheres under no-slip conditions.

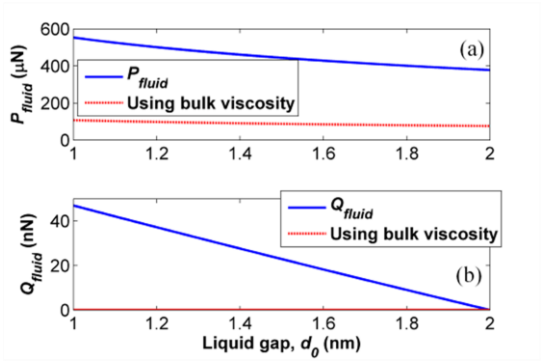


Figure 3.8: Hydrodynamic normal (a) and shear (b) forces for a 500 nm radius sphere (relevant to magnetic storage).

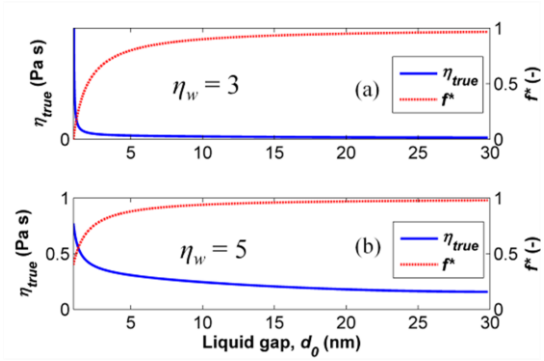


Figure 3.9: 'True' viscosity and slip factor as functions of the gap for: (a) η_w = 3 and (b) η_w = 5.

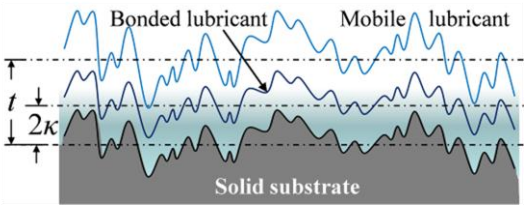


Figure 3.10: Rough lubricated surface topography.

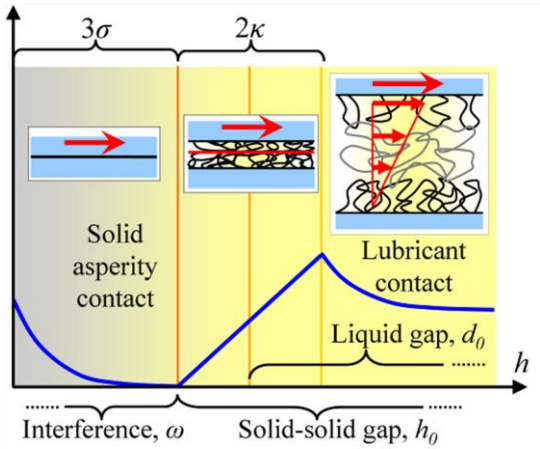


Figure 3.11: Regimes of contact.

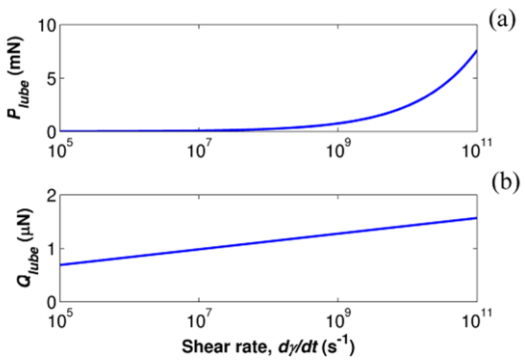


Figure 3.12: Normal (a) and shear force (a) for shear rates larger than the maximum experimental values.

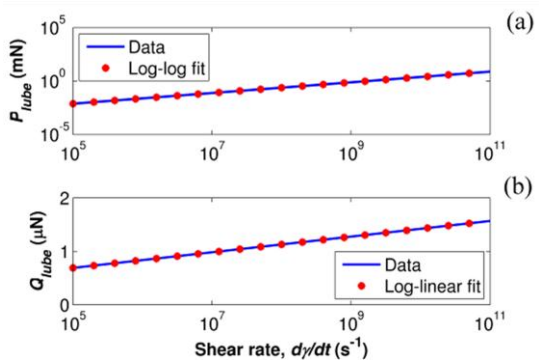


Figure 3.13: Curve-fits to the normal (a) and shear forces (b) as functions of shear rate.

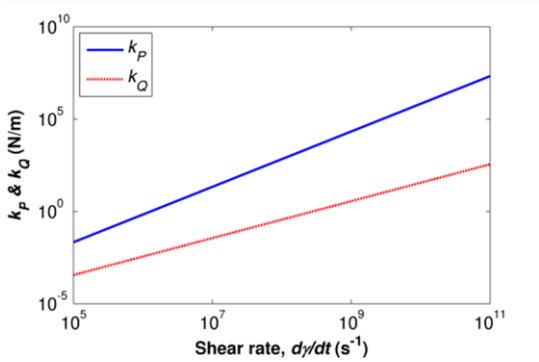


Figure 3.14: Normal and shear stiffnesses as functions of shear rate.

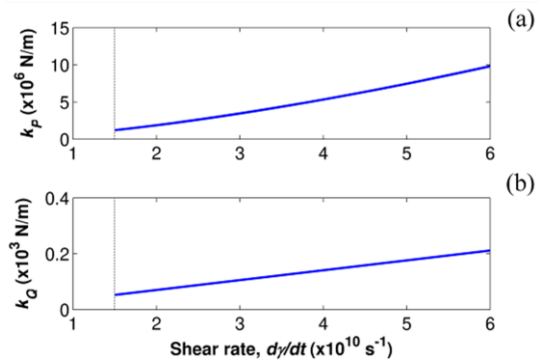


Figure 3.15: Normal (a) and shear stiffnesses (b) in molecularly thin lubricants.

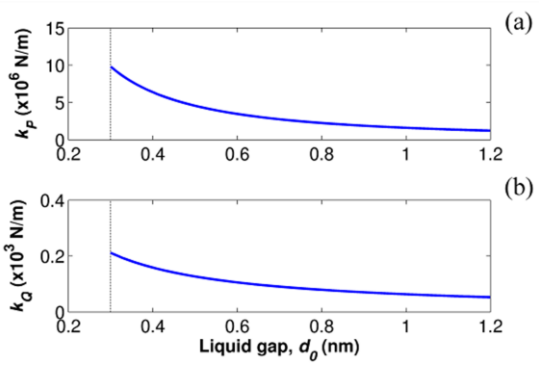


Figure 3.16: Normal k_P (a) and shear k_Q stiffnesses (b) as a function of the liquid gap for very high shear rates of 1.5×10^{10} to 6×10^{10} s^{-1}.

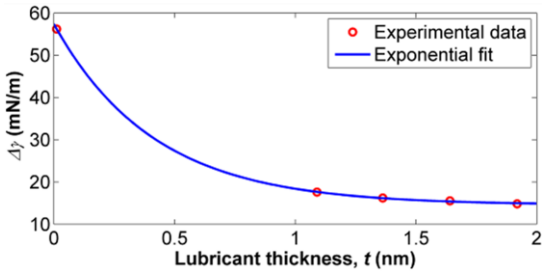


Figure 3.17: Total surface energy as a function of lubricant thickness. Experimental data fromYeo *et al.*

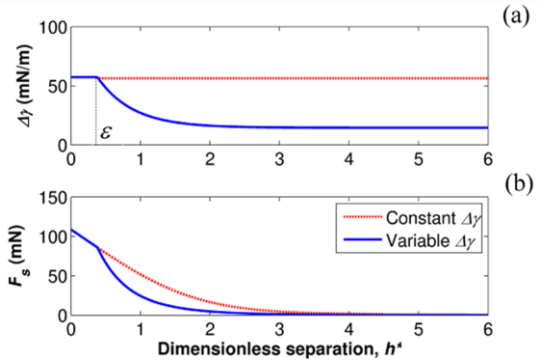


Figure 3.18: Variable surface energy (a) and total adhesive force (b) as a function of dimensionless separation.

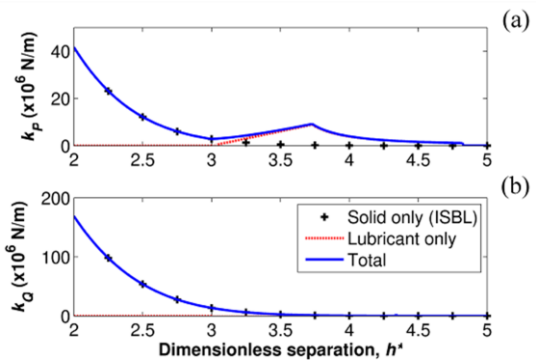


Figure 3.19: Normal (a) and lateral (b) stiffnesses as a function of dimensionless separation.

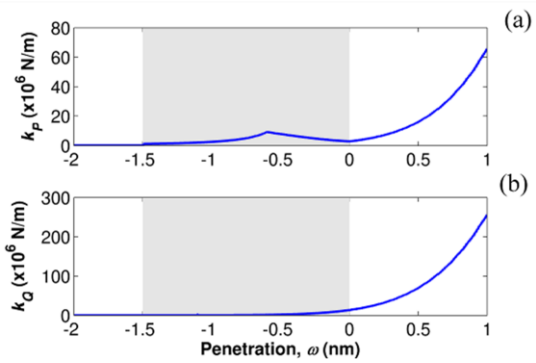


Figure 3.20: Normal (a) and lateral (b) stiffnesses as a function of penetration.

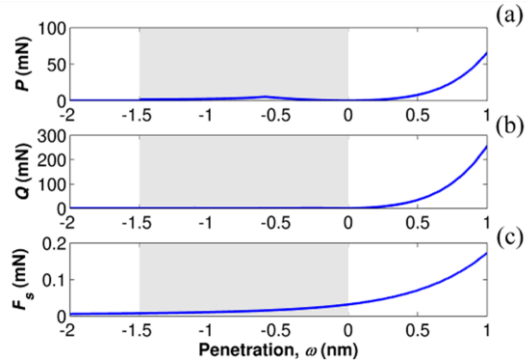


Figure 3.21: Total contact (a), friction (b), and adhesion (c) forces as a function of penetration.

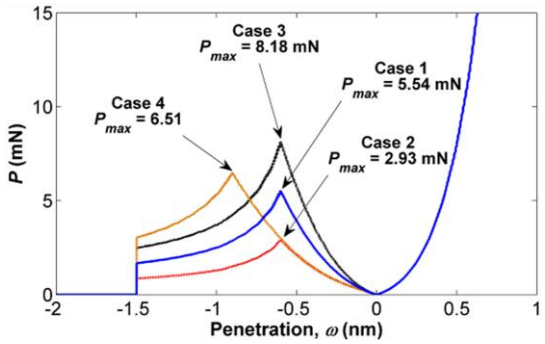


Figure 3.22: Total contact force as a function of penetration for different lubricant conditions.

3.5: TABLES

Table 3.1: Slip model parameters.

Physical behavior	u_s	f^*	u_w
No slip	0	1	U
Slip with $u_s \leq U$	u_s	$1 - u_s^*$	$U–u_s$
Slip with $u_s > U$	u_s	0	0
Unbounded slip	∞	0	0

Table 3.2: Model parameters used in MTL contact model.

Parameters			Unit
RMS roughness #1	σ_1	0.80	nm
Mean asperity radius #2	R_1	32.74	μm
Areal density #1	η_1	1.77	μm^{-2}
RMS roughness #2	σ_2	0.19	nm
Mean asperity radius #2	R_2	3.92	μm
Areal density #2	η_2	47.70	μm^{-2}
RMS roughness	σ	0.82	nm
Mean asperity radius	R	3.89	μm
Areal density	η	34.92	μm^{-2}
Roughness parameter	β	0.112	–
Young's modulus #1	E_1	200	GPa
Poisson ratio #1	v_1	0.20	–
Young's modulus #2	E_2	390	GPa
Poisson ratio #2	v_2	0.21	–
Hardness	H	15	GPa
Equilibrium spacing	ε	0.3	nm
$\Delta\gamma$ coefficient #1	c_1	42.84	mN/m
$\Delta\gamma$ coefficient #2	c_2	2.41	nm^{-1}
$\Delta\gamma$ coefficient #3	c_3	14.54	mN/m
Minimum liquid gap	κ	0.3	nm
Maximum viscosity	μ_0	0.31	Pa s
Lubricant thickness	t	1.5	nm
Sliding velocity	U	30	m/s
Nominal area of contact	A_n	2,500	μm^{-2}

CHAPTER 4 – LUBRICANT CONTACT FOR TFC SLIDERS

4.1: THREE-DOF DYNAMIC CONTACT MODEL WITH LUBRICANT CONTACT

The exact TFC bulge geometry is mathematically obtained in accordance with recent experimental measurements that show a constant bulge profile with actuation. Instead of the bulge changing its height during actuation, the surrounding material actually goes through most of the deformation carrying the TFC bulge towards the disk surface. Three springs and dampers are introduced to model the AB for the 3-DOF system: two nonlinear stiffening springs for the normal and pitch displacements and an angular spring for roll. Spring stiffnesses are calculated directly from the corresponding natural frequencies of each DOF as functions of TFC actuation and for a given nominal FH via modal analysis. The normal spring is highly nonlinear while the pitch and roll springs could be assumed linear. All three springs are treated as nonlinear in the present model, while the damping coefficients are assumed to be constant. The moment arm from the center-of-mass (COM) to the shifting POC affects the moments acting on the slider and could induce angular displacements in the pitch and roll directions. It is possible that two or more points on the slider come into contact with the disk at any given time. Given multiple possible contact points on the slider surface, a calculation of the nominal contact area for each potential feature in contact is performed to obtain the adhesive and, subsequently, the solid contact and friction forces. Details on the modeling methodology can be found in earlier work [10]. The following sections describe the specifics of the AB, possible points of contact and nominal area calculations used in the present mode.

4.1.1: Modeling the AB

Figure 4.1 is a schematic of the proposed 3-DOF model. The slider body is allowed to move in the normal direction with displacement $z = z_{COM}$ at its COM. The other two DOFs correspond to rotations about the COM by pitch and roll angles θ and φ respectively as shown in Figure 4.1. The slider body is mounted on a suspension with normal stiffness and damping coefficient k and c in the normal DOF, and angular stiffnesses k_θ and k_φ and angular damping coefficients c_θ and c_φ in the pitch and roll DOFs respectively; these stiffnesses and damping coefficients are constant and known by design. In addition, a preload force F is also applied on the suspension.

To balance the suspension and preload forces, the ABS is designed to develop forces and moments with air-flow between the slider and disk that will maintain a relatively constant FH under the influence of disk vibrations. Figure 4.1 also shows the flying condition (a) and two possible contacting conditions at the TFC bulge (b) or an ABS corner (c); it is assumed that contact may occur on different points on the slider, as will be further explained later. The variable POC would result in various moments acting on the slider COM.

The AB forces and moments can be extracted by solving the Reynolds equations (accounting for temperature variations and other effects) for the air flow under the ABS and are functions of the FH at the pole-tip [25]. The pole-tip FH (FH @ PT) can be related directly to the read-back signal of the read element – this is experimentally measureable – and is defined within the context of the present 3-DOF model through geometry as the physical separation at the location of the read element, i.e. FH @ PT is the difference between the slider and disk displacements at the location of the read transducer. TFC actuation results in stiffening of the AB and push-back of slider such that the slider FH (measured at the TFC base) is larger than the nominal value; the resulting increase of the local FH at the TFC bulge is compensated by additional actuation. To model these effects we introduce three AB springs and dampers and include AB stiffening forces based on published experimental and simulation results [7]. Two AB spring forces at the front (k_f, c_f) and rear (k_r, c_r) are used to model normal (z) and rotational pitch angle motion (θ) while an angular spring and damper (k_l, c_l) counter rotational roll angle motion (φ).

The mass matrix of the system is

$$\mathbf{M} = \begin{bmatrix} m & 0 & 0 \\ 0 & \frac{1}{12} m\left(l^2 + l_t^{\,2}\right) & 0 \\ 0 & 0 & \frac{1}{12} m\left(l_w^{\,2} + l_t^{\,2}\right) \end{bmatrix} \tag{4.1}$$

The slider has mass m while its moments of inertia about the COM for the pitch and roll DOFs can be expressed in terms of the slider dimensions of length l, width l_w and thickness l_t as shown in equation (4.1). Eccentricity e is introduced to describe possible offset of the point of attachment of the suspension on the slider along the slider length and relative to the COM;

hence, the damping and stiffness matrices are

$$\mathbf{C} = \begin{bmatrix} c & ec & 0 \\ ec & e^2c + c_\theta & 0 \\ 0 & 0 & c_\varphi + c_l \end{bmatrix} \tag{4.2}$$

$$\mathbf{K} = \begin{bmatrix} k & ek & 0 \\ ek & e^2k + k_\theta & 0 \\ 0 & 0 & k_\varphi + k_l \end{bmatrix} \tag{4.3}$$

The angular stiffness and damping of the AB in the roll DOF, k_l and c_l respectively, are included in the above matrices while the front and rear AB forces and moments are expressed in terms of the front and rear AB spring forces F_{af} and F_{ar} on the right hand side of the equations of motion. This is done because the roll AB moments depend only on the roll angle φ, while the front and rear spring forces depend on the local FH at the spring locations, which is a function of the local value of DMW (i.e., displacement and velocity of the disk).

To describe the local FH at the front and rear spring locations we introduce the following rotation matrix:

$$\mathbf{R} = \begin{bmatrix} \cos\theta & \sin\theta\sin\varphi & -\sin\theta\cos\varphi \\ 0 & \cos\varphi & \sin\varphi \\ \sin\theta & -\cos\theta\sin\varphi & \cos\theta\cos\varphi \end{bmatrix} \tag{4.4}$$

The front AB spring (and damper) is located at a distance d_f from the COM along the slider length while the rear AB spring is at a distance d_r as shown in Figure 4.1. Then, the locations of the AB springs relative to the COM can be found as

$$\begin{Bmatrix} x \\ y \\ z \end{Bmatrix}_f = \mathbf{R} \begin{Bmatrix} d_f \\ 0 \\ 0 \end{Bmatrix} \tag{4.5}$$

$$\begin{Bmatrix} x \\ y \\ z \end{Bmatrix}_r = \mathbf{R} \begin{Bmatrix} -d_r \\ 0 \\ 0 \end{Bmatrix} \tag{4.6}$$

The origin for the system is centered at the COM and is defined as follows: positive *x*-coordinates lie along the slider length in the direction of the LE; positive *z*-coordinates lie along the slider thickness in the direction of the slider suspension; positive *y*-coordinates lie along the slider width and are defined relative to *x* and *z* with the right-hand rule (i.e., positive *y* points into the page in Figure 4.1). It should be noted that the skew angle could be accounted for by left-multiplying matrix (4.4) with a rotation matrix imposing slider rotations about the *z*-axis. Since the AB changes with the skew angle, the skew angle is kept constant at zero for the present work and emphasis is placed on studying the effects of the third DOF and lubricant contact.

Let us define the distance between the COM and the ABS as a function of the pitch and roll angle rotations:

$$\Delta_{ABS} = \tfrac{1}{2} l_t \cos\theta \cos\varphi \tag{4.7}$$

Then, the local FH at the front and rear AB springs is

$$\mathrm{FH}_f = \left(z - \Delta_{ABS} + z_f \right) - z_{df} \tag{4.8}$$

$$\mathrm{FH}_r = \left(z - \Delta_{ABS} + z_r \right) - z_{dr} \tag{4.9}$$

The vertical displacement of the COM is denoted as *z*. To estimate the initial values of the AB spring forces, we let the local FH be equal to the nominal value at each spring and use the spring stiffness values corresponding to the nominal values.

A simplified (discounting adhesion and contact) undamped 3-DOF model is used to calculate the AB stiffnesses as functions of the FH at the pole-tip. AB simulator data relates the resonant frequencies corresponding to each DOF to the FH @ PT, as shown in Figure 4.2, and can be used

to calculate the AB stiffnesses through modal analysis. The front and rear AB springs with stiffnesses k_f and k_r are extracted from the two pitch modes corresponding to vertical motion (2^{nd} pitch mode) and pitch angle rotation (1^{st} pitch mode), while the rotational roll spring with stiffness k_l is assumed to be effectively decoupled from the pitch modes for symmetric ABS designs and zero skew angles [25].

The search space for k_f and k_r is varied between 10^4 and 10^7 N/m and the values are selected for which modal analysis yields eigenvalues corresponding, within ±5%, to the target normal and pitch resonant frequencies. This is performed for each FH data point (FH @ PT = 2.5, 5, 10, 15 and 20 nm) and the results are interpolated to yield smooth curves for the stiffnesses as functions of FH @ PT. The lateral angular AB spring stiffness k_l is inherently decoupled from k_f and k_r as discussed above and can be calculated analytically from the roll resonant frequency, which is approximately constant.

TFC actuation results in AB stiffening, which, in turn, results in push-back to the slider that changes the nominal FH [7]. Experiments showed that environmental temperature and humidity, while having significant effects on the FH, have limited effects on the TFC bulge height [98]. Therefore, ambient effects can be adequately captured by changing the AB simulation conditions to predict the modes as functions of FH @ PT (Figure 4.2), and the effect of TFC actuation can be decoupled and superposed as proposed in the current AB model. Published data pertaining to AB stiffening are summarized in Figure 4.3 and describe the FH change ΔFH, the push-back factor α and increase in AB force ΔFAB as functions of the normalized actuation power.

These data can be expressed as functions of TFC actuation by using the following equation relating the change in FH and the push-back factor [7]:

$$h_{TFC} = \frac{\Delta \mathrm{FH}}{1-\alpha} \tag{4.10}$$

Since both ΔFH and α as functions of normalized power are known, we can rearrange the quantities as shown in Figure 4.4 to ultimately obtain the increase in AB force as a function of the TFC actuation. Also, the change in FH as a function of actuation, which follows the relation

$\Delta FH \approx 0.5 h_{TFC}$, is useful in validating the AB model proposed in the present work.

The initial front and rear AB spring FH are equal to the nominal value. The initial AB spring forces correspond to the values at nominal FH

$$F_{af,nom} = k_{f,nom} \mathrm{FH}_{nom} + \left(\frac{d_r}{d_f + d_r} \right) \Delta F_{AB,nom} \tag{4.11}$$

$$F_{ar,nom} = k_{r,nom} \mathrm{FH}_{nom} + \left(\frac{d_f}{d_f + d_r} \right) \Delta F_{AB,nom} \tag{4.12}$$

The factor in front of the stiffening force comes from taking the moment balance about the COM and distributes the stiffening force between the front and rear AB springs. In the case where $d_f = d_r$, each AB spring experiences half of the total stiffening force. For example, for nominal FH = 11 nm, the sum of the nominal values of F_{af} and F_{ar} is 11.75 mN; this is expected to be balanced by the preload force of 14.7 mN at slightly smaller FH than the nominal value (where the AB will be stiffer) while there will also remain net moments to be balanced by the suspension at angles that will be somewhat smaller than the initial values.

The following equations are used to calculate the AB spring forces beyond the initial conditions:

$$F_{af} = k_f \left(\mathrm{FH}_{nom} - \mathrm{FH}_f \right) + \left(\frac{d_r}{d_f + d_r} \right) \Delta F_{AB} + c_f \left(\dot{z}_{df} - \dot{z}_f \right) \tag{4.13}$$

$$F_{ar} = k_r \left(\mathrm{FH}_{nom} - \mathrm{FH}_r \right) + \left(\frac{d_f}{d_f + d_r} \right) \Delta F_{AB} + c_r \left(\dot{z}_{dr} - \dot{z}_r \right) \tag{4.14}$$

The local AB spring FH values are given in equations (4.8) and (4.9). The DMW velocity can be obtained by numerical differentiation of the displacement signal; the opposite may also be true when the DMW velocity signal is measured experimentally and the displacement is calculated via numerical integration. The velocities of the slider at the AB spring locations are

$$z_f = d_f \dot{\theta} \cos\theta \tag{4.15}$$

$$z_r = -d_r \dot{\theta} \cos\theta \tag{4.16}$$

The resulting AB and suspension forces and moments applied to the right hand side of the equations of motion are

$$\mathbf{f}_a = \begin{Bmatrix} F_{af} + F_{ar} \\ x_f F_{af} + x_r F_{ar} \\ y_f F_{af} + y_r F_{ar} \end{Bmatrix} + \begin{Bmatrix} -F \\ -(e\cos\theta) F \\ 0 \end{Bmatrix} \tag{4.17}$$

The moment arms for each spring can be found using equations (4.5) and (4.6).

4.1.2: TFC Bulge Geometry

Experimental work performed by the authors was successful in measuring the TFC bulge profile during actuation. Unlike the model used previously that assumed a bulge of variable height with actuation [10], these experiments identified a constant TFC bulge height that changed only by a couple of nanometers in height, while most of the thermal deformation occurred in the surrounding material. As shown in Figure 4.5, this can be visualized by imagining the TFC bulge as a fixed protruding stylus pushed toward the disk surface by the deformation of the material supporting it. Hence, modeling of the TFC bulge needs to be adjusted accordingly. The bulge itself can still be accurately modeled as an ellipsoid having constant dimensions a_{TFC}, w_{TFC} and b_{TFC} and offset from the TE by x_{TFC} as was done in previous work. However, the overall actuation height h_{TFC} is now defined relative to the "zero" surface of the slider and its minimum value is equal to b_{TFC}. Specifically, the overall TFC height at zero actuation is that of the bulge such that $h_{TFC} = b_{TFC}$; the TFC base is on the same level as the "zero" surface before actuation.

Actuation results in the TFC base deforming such that the total actuation height becomes $h_{TFC} > b_{TFC}$. Even though the pitch and roll angles of the slider are expected to be very small (of the order of few hundred and tens of microradians respectively), it is conceivable that contact could occur on the TFC base corners. For this reason, it is necessary to describe the TFC base

geometry relative to the COM and calculate the position of its corners for any given combination of pitch and roll angles. The same is done for the contact pads as well as the TE and LE.

4.1.3: Possible POCs

In the most general case, contact may occur on whichever feature of the slider surface is closest to the rotating disk. At the same time, adhesion may act on any such location without contact: this requires the estimation of a nominal area of contact for each feature, which will be addressed in more detail later. Contact could occur on the lowest point of the TFC bulge as was the case in our previous 2-DOF model [10]. In the present work, contact is allowed to occur on the corners of the TFC base, the contact pads located close to the LE and on either corner of the TE or LE in the absence of significant slider body deformation.

Figure 4.6 shows, in the general case, the topography of the ABS. While TE and LE refer to the leftmost and rightmost edges (along l_w) of the slider as shown in Figure 4.1, contact could occur on the recessed surface located at a height step h_S below the "zero" surface and recessed by a step length l_S relative to the slider edges. For simplicity, we shall refer to the recessed surface edges as the TE and LE for the purposes of this model.

The TFC base and contact pads constitute the "zero" surface, which is one-half l_t distance away from the slider COM, while the TFC bulge, as stated earlier, protrudes from the "zero" surface by $h_{TFC} \geq b_{TFC}$. The width of the TFC base is denoted as w_{BASE}, while the contact pads are located at distances x_{PAD} and y_{PAD} relative to the slider COM. The contact pads are represented as spherical caps having radius R_{PAD}. There may be more than one POC at any given time, while more than one slider features may experience contact and/or adhesion at any given time. Hence, a description of each slider feature location is necessary. Figure 4.7 shows the possible POC for negative roll angle φ.

The modeling methodology for the TFC bulge ellipsoid was presented in previous work [10]. Each feature is described geometrically relative to the COM. Then, the local FH is calculated for the lowest point of each feature. For example, given a combination of pitch and roll angles, the lowest point may lie on the TFC bulge, followed by the left corner of the base, the left contact

pad and the left corners of the TE and LE respectively. Next, we need to rigorously define the different possible regimes of operation. This is important for the calculation of the nominal area of contact at each feature. The tallest asperities of the combined rough surface, extracted from the roughness parameters of the individual rough slider and disk surfaces, are contained within a distance of 3σ from their mean, especially after some mild burnishing of the surfaces. An MTL layer of total average thickness t lies on top of the combined rough surface. For convenience, we assume that the combined rough surface containing the total lubricant layer is on the bottom and moves with the DMW of the disk while the smooth surface corresponds to the slider and changes its location based on z, θ and φ. The slider is considered to be flying, steadied by the balance of the preload and suspension with the AB forces and adhesive interactions, when the local (at each slider feature) FH = FH_i, defined as the difference between the dynamic local altitude and the local value of the DMW is $FH_i > 3\sigma+t$. Lubricant contact occurs when $3\sigma \leq FH_i \leq 3\sigma+t$ and solid contact occurs when $FH_i < 3\sigma$. The AB forces are assumed to become negligible beyond some limiting FH (~15 nm) while adhesion is negligible for $FH_i > 6\sigma$ (assuming $3\sigma \approx t$). Based on these definitions, any feature on the slider can be described as being in the flying, lubricant or solid contact regimes.

The modeling methodology for the TFC bulge ellipsoid was presented in previous work [10]; this is presently updated for the additional DOF: roll. The parametric equations for a scalene ellipsoid are

$$\begin{Bmatrix} x \\ y \\ z \end{Bmatrix}_{ELL} = \begin{Bmatrix} a_{TFC} \cos\alpha \sin\beta \\ \frac{1}{2} w_{TFC} \sin\alpha \sin\beta \\ b_{TFC} \cos\beta \end{Bmatrix} \tag{4.18}$$

The semi-widths along the x- and z-axes are a_{TFC} and b_{TFC} respectively, while the width along the y-direction is w_{TFC}. The parametric angle α is measured from the positive x-axis in the xy-plane and is positive in the clockwise direction; β is measured from the positive z-axis in the yz-plane and is positive in the counter-clockwise direction. The vector describing the location of the ellipsoid center relative to the COM is

$$\begin{Bmatrix} x \\ y \\ z \end{Bmatrix}_{TFC,0} = \begin{Bmatrix} -\frac{1}{2}l + x_{TFC} \\ 0 \\ -\frac{1}{2}l_t - \left(h_{TFC} - b_{TFC}\right) \end{Bmatrix} \tag{4.19}$$

The slider has dimensions $l \times l_w \times l_t$ and the TFC ellipsoid is offset from the TE by x_{TFC}. The parametric equations of the TFC ellipsoid are

$$\begin{Bmatrix} x \\ y \\ z \end{Bmatrix}_{TFC,ELL} = \begin{Bmatrix} x \\ y \\ z \end{Bmatrix}_{TFC,0} + \begin{Bmatrix} x \\ y \\ z \end{Bmatrix}_{ELL} = \begin{Bmatrix} -\frac{1}{2}l + x_{TFC} + a_{TFC}\cos\alpha\sin\beta \\ \frac{1}{2}w_{TFC}\sin\alpha\sin\beta \\ -\frac{1}{2}l_t - \left(h_{TFC} - b_{TFC}\right) + b_{TFC}\cos\beta \end{Bmatrix} \tag{4.20}$$

The coordinates of the POC surface cannot be calculated analytically from geometry. Instead, the POC can be found numerically by creating a rectangular grid in the *xy*-plane and extracting the indices where the altitude (*z*-coordinate) reaches its minimum. The coordinates of the POC are found by minimizing the *z*-coordinate of the following equations to find the angles α and β:

$$\begin{Bmatrix} x \\ y \\ z \end{Bmatrix}_{TFC} = \mathbf{R}\begin{Bmatrix} x \\ y \\ z \end{Bmatrix}_{TFC,ELL} \tag{4.21}$$

The moment arm for contact at the lowest point of the TFC bulge can be extracted numerically based on the methodology described above. The moment arms for contact at the corners of the TFC base, contact pads, or the corners of the TE and LE can be found by left-multiplying the vectors describing the location of each feature with the rotation matrix (4.4). Either of the slider sides may come into contact depending on the sign of the roll angle φ; this is addressed with the use of the sign function. The vectors describing the moment arms are

$$\mathbf{r}_{COM\to TFC} = \min\begin{Bmatrix} x \\ y \\ z \end{Bmatrix}_{TFC} \quad \forall\,\alpha \in \left[0, \pi\right], \beta \in \left[\tfrac{1}{2}\pi, \tfrac{3}{2}\pi\right] \tag{4.22}$$

$$\mathbf{r}_{COM\to BASE} = \mathbf{R}\begin{Bmatrix} -\left(\frac{1}{2}l - l_S\right) \\ \operatorname{sgn}(\phi)\frac{1}{2}w_{BASE} \\ -\left[\frac{1}{2}l_t + \left(h_{TFC} - b_{TFC}\right)\right] \end{Bmatrix} \tag{4.23}$$

$$\mathbf{r}_{COM\to PAD} = \mathbf{R}\begin{Bmatrix} x_{PAD} \\ \operatorname{sgn}(\phi)\, y_{PAD} \\ -\frac{1}{2}l_t \end{Bmatrix} \tag{4.24}$$

$$\mathbf{r}_{COM\to TE} = \mathbf{R}\begin{Bmatrix} -\left(\frac{1}{2}l - l_S\right) \\ \operatorname{sgn}(\phi)\left(\frac{1}{2}l_w - l_S\right) \\ -\left(\frac{1}{2}l_t - h_S\right) \end{Bmatrix} \tag{4.25}$$

$$\mathbf{r}_{COM\to LE} = \mathbf{R}\begin{Bmatrix} \left(\frac{1}{2}l - l_S\right) \\ \operatorname{sgn}(\phi)\left(\frac{1}{2}l_w - l_S\right) \\ -\left(\frac{1}{2}l_t - h_S\right) \end{Bmatrix} \tag{4.26}$$

4.1.4: Location of Read/Write Elements

A final geometric consideration is to find the exact altitudes of the read/write (R/W) elements in order to better calculate the magnetic spacing. This can be achieved through geometric manipulation. First, we need to rotate the TFC ellipsoid by -90 degrees about its local *y*-axis so that the definitions of the angles α and β are changed: α is now measured from the negative *z*-axis in the *yz*-plane and is positive in the counter-clockwise direction; β is measured from the positive *x*-axis in the *xz*-plane and is positive in the clockwise direction. This rotation also necessitates the switching of a_{TFC} and b_{TFC} to retain the proper ellipsoid dimensions. Now, simply setting $\alpha = 0$ defines a cross-sectional ellipse on the *xz*-plane and β, ranging between 0 and π, defines any point on its bottom half. The coordinates of this z*x*-plane ellipse are

$$\begin{Bmatrix} x \\ y \\ z \end{Bmatrix}_{TFC,xz} = \begin{Bmatrix} a_{TFC}\cos\beta \\ 0 \\ -b_{TFC}\sin\beta \end{Bmatrix} \tag{4.27}$$

Let the R/W elements be offset from the ellipsoid center by distances x_R and x_W in the x-direction. Provided that $x_R < {}_{aTFC}$ and $x_W < {}_{aTFC}$, the x-coordinate of equation (4.27) can be set equal to either x_R or x_W to find the angles βR and βW defining the location of the read and write elements on the bulge respectively. Assuming that the write element is offset from the ellipsoid center towards the TE and the read element is offset in the opposite direction, the values of β are

$$\beta_R = \cos^{-1}\left(\frac{x_R}{a_{TFC}}\right), \beta_W = \cos^{-1}\left(\frac{-x_W}{a_{TFC}}\right) \tag{4.28}$$

The R/W element z-coordinates measured from the ellipsoid center can be calculated by plugging these angles into the z-component of equation (4.27). Since the location of the ellipsoid center relative to the COM is known, the altitude of the R/W elements relative to the COM can be easily found through geometry. Then, the read transducer FH, termed the FH at the pole-tip (FH @ PT), can be extracted and used to determine the value of the AB stiffnesses as discussed previously.

4.1.5: Nominal Areas of Contact

An estimate of the nominal area of contact (as we are dealing with the proximity and contact of rough surfaces) is necessary to calculate the adhesive, contact and friction forces acting on any feature on the slider based on the ISBL model [48]. The nominal area can be calculated by truncating each feature experiencing adhesion or lubricant or solid contact at a local truncation height. As per previous work that has shown very good agreement with experimental data [10], adhesion is negligible when the local FH is larger than 6σ (assuming that the lubricant thickness is of the order of the roughness, i.e. $3\sigma \approx t$). Therefore, we define the truncation height as $h_{T,i} = 6\sigma – \mathrm{FH}_i$ where FH_i is the local separation at each feature; the range of truncation heights will vary between zero (for $\mathrm{FH}_i > 6\sigma$) and 3σ so that $h_{T,i} = 6\sigma – 3\sigma = 3\sigma$ beyond the initiation of solid contact even though $\mathrm{FH}_i < 3\sigma$ during solid contact. The nominal area allows for the calculation of the local contact, friction and adhesion forces as well as the real area of contact. Contact and friction forces exist for both the lubricant and solid contact regimes; their formulation is shown in recent work by the authors [23, 24].

The calculation of the nominal area of contact of the TFC bulge is performed numerically. The cutting plane is in general defined relative to the lowest point of a feature on the slider and is parallel to the *xy*-plane:

$$\begin{Bmatrix} x \\ y \\ z \end{Bmatrix}_{CUT} = \begin{Bmatrix} s \\ r \\ z_{POC} + h_{T,i} \end{Bmatrix} \tag{4.29}$$

For example, in the case of the TFC bulge, the parameterized variables s and r along the *x*- and *y*-directions respectively may vary between $-w_{TFC}$ and $+w_{TFC}$ (chosen because it is the largest dimension of the ellipsoid) and z_{POC} is the altitude (*z*-coordinate) of the lowest point (POC) found numerically as described in the previous section. Then, using the parametric equations describing the ellipsoid geometry, the following equation can be solved numerically to yield the coordinates of the points along the cross-section of the ellipsoid with the cutting plane, which is translated up from the POC by a truncation height $h_{T,TFC}$ varying between 0 and 3σ:

$$\begin{Bmatrix} x \\ y \\ z \end{Bmatrix}_{TFC} = \begin{Bmatrix} x \\ y \\ z \end{Bmatrix}_{CUT} \tag{4.30}$$

Figure 4.8 shows the truncation of the TFC bulge ellipsoid with a cutting plane situated at $h_{T,TFC} = 3\sigma = 1.5$ nm from the POC. The dimensions of the TFC bulge are: $a_{TFC} = 5$ μm, $b_{TFC} = 5$ nm, $h_{TFC} = 20$ nm, $w_{TFC} = 50$ μm and $x_{TFC} = 15$ μm; the dimensions of the slider are: $l = 1.23$ mm, $l_w = 0.7$ mm and $l_t = 0.3$ mm; the pitch and roll angles are: $\theta = 100$ μrad and $\varphi = -50$ μrad. Note the high aspect ratio of the plot where the ellipsoid height in the *z*-direction is of the order of nanometers while the lateral dimensions are of the order of micrometers.

The nominal area calculated for the given parameter values is 186.79 μm^2. It is rather difficult and time consuming to calculate the surface area of the truncated scalene ellipsoid; instead, the nominal area is approximated as that of the cross-sectional ellipse with negligible error. Using the same methodology, the nominal areas for the TFC base, TE and LE can be calculated from the truncation of cuboids with the cutting plane described in equation (4.29). The surface area of

the contact pads is equal to the surface area of a spherical cap, i.e. $2\pi R_{PAD} h_{T,PAD}$.

4.1.6: Dynamic Equations of Motion

The equations of motion of the slider are given in matrix form as:

$$\mathbf{M}\ddot{\mathbf{s}} + \mathbf{C}\dot{\mathbf{s}} + \mathbf{K}\mathbf{s} = \mathbf{f}_a + \mathbf{f}_c \tag{4.31}$$

The mass, damping and stiffness matrices are given in equations (4.1), (4.2) and (4.3), while the state vector is $\mathbf{s} = \langle z, \theta, \varphi \rangle^T$. The AB vector includes the suspension preload force contributions as well as the initial and current AB forces and moments and is shown in equation (4.17). The total contact force vector includes contributions from the contact, friction and adhesion forces:

$$\mathbf{f}_c = \begin{Bmatrix} F_{net} \\ M_{net,\theta} \\ M_{net,\varphi} \end{Bmatrix} \tag{4.32}$$

The total contact force vector components are

$$F_{net} = \sum_{i=1}^{n} \left(F_{c,i} - F_{s,i} \right) \tag{4.33}$$

$$M_{net,\theta} = -\sum_{i=1}^{n} \left[x_{POC \to i} \left(F_{c,i} - F_{s,i} \right) + z_{POC \to i} Q_i \right] \tag{4.34}$$

$$M_{net,\varphi} = \sum_{i=1}^{n} \left[y_{POC \to i} \left(F_{c,i} - F_{s,i} \right) \right] \tag{4.35}$$

There may be n features in contact at any time; if these experience only adhesive interactions, then only $F_{s,i}$ will be non-zero. The friction force is extracted from the corresponding magnitude of the dynamic force as explained in previous work. Hence, the friction coefficient time history may be calculated as the ratio of the magnitudes of the friction and contact forces. The active

forces and their resulting moments are summed at every time increment.

The nonlinear system of equations (4.31) can be solved numerically at each time increment using a Runge-Kutta 5th order numerical scheme to yield time histories of the displacements, nominal and real areas of contact, forces and moments acting on each slider feature. The convergence of the solution is sensitive to the time step; it was found that this must be at least 10^{-10} seconds to guarantee convergence, especially in the presence of discontinuities such as contact forces and impulses.

4.1.7: Results and Discussion

Three conditions were simulated using the 3-DOF dynamic contact model with friction: constant TFC actuation; constant TFC actuation with impulse shock; and, variable TFC actuation. The first is used to determine the accuracy of the AB model. A shock is applied to the slider COM to test whether slider features other than the TFC bulge come into contact as well as for system identification purposes. Then, an actuation profile is applied to simulate realistic HDI behavior and test whether the model can capture the transient effects observed in experiments. Finally, lubricant parameters are varied as per the MTL contact model [24] to investigate the effect of the lubricant layer on contact and flyability.

4.1.7.1: Model Parameters and Dynamic Input

Table 4.1 lists the dynamic model parameters used in the 3-DOF model. These were adopted from previous work [10]. The nominal FH is 11 nm, while the limiting FH, at twice the nominal value, is the FH beyond which the AB is assumed to be negligible. An initial roll angle of -10 μrad was used to introduce some initial roll. The suspension stiffness and damping ratio in the roll DOF were assumed to be equal to those of the pitch DOF. Table 4.2 lists the material and roughness parameters used in previous work [10]. These are used in the ISBL model to calculate the contact, friction and adhesion forces as functions of mean plane separation [10, 13].

Modeling the ABS topography, as shown for the general case in Figure 4.6, is important in predicting the possible POC. Feature dimensions are summarized in Table 4.3. The TFC bulge and base were measured before and during actuation using profilometry (P-15, KLA-Tencor,

CA, USA) and analyzed with custom software created by the authors. Contact pad locations, ABS recessions and the offsets at the TE and LE, were estimated from published data [60, 99] and experimental measurements; the radius of the contact pads was assumed to be 1 mm.

The DMW was experimentally measured for disks used in TFC technology drives. However, the three-dimensional nature of the model requires the use of more than a single DMW time history since, arguably, each part of the slider ABS "experiences" different disk motion along the slider width. We take this into account by transforming the measured DMW time history to produce two DMW tracks that share the same frequency content but are different from the original. The second DMW track is created by flipping the time scale of the original so that it starts from the original's end. The third DMW track is created by taking the negative of the flipped signal. The original track is used as the DMW at the TFC bulge, while the flipped and negative tracks are used on the positive and negative *y*-direction of each feature respectively. If only one track is used, roll motion predictably goes to zero very quickly. Using three incommensurable (in time) DMW tracks as described above induces further roll vibrations as would be expected in reality.

4.1.7.2: Constant TFC Actuation Results

Contact is observed only at the TFC bulge for a constant TFC actuation of 12 nm. This is consistent with the assumptions of our previous 2-DOF model that neglected the roll DOF [10]. (Note that the results below are different than what was reported in [10] as in this work the contact model is more realistic and includes the contact of the MTL). After the initial transients that depend on the initial conditions used in the simulation, the slider follows the DMW with small modulation as shown in Figure 4.9. In Figure 4.9(a), the DMW is translated by 3σ and $3\sigma+t$ to denote the limits of solid and lubricant contact respectively. The FH @ PT, defined relative to z_{TFC} in section 2.4, becomes constant beyond the initial transients, as shown in Figure 4.9(b).

The steady state result for constant actuation is the same regardless of whether the ISBL or the MTL model is used. However, the improved formulation of the adhesive force in the MTL model, where the surface free energy varies with penetration into the lubricant layer, results in reduced vibrations that diminish beyond the initial transient. In contrast, as shown in the comparison of Figure 4.10, the ISBL model predicts a prolonged regime of sustained vibrations

due to the proximity of the slider to the disk DMW.

As was shown in Figure 4.4(b), the relationship between FH gain and TFC actuation is $\Delta FH \approx 0.5h_{TFC}$. Hence, an actuation of 12 nm should result in an FH gain of ~6 nm. In comparison, neglecting AB stiffening and FH gain, the expected FH would be equal to the difference between the nominal FH and the TFC actuation, i.e. 11-12 = -1 nm. Our simulation for a constant TFC actuation of 12 nm results in FH @ PT = 7.5 nm, as shown in Figure 4.9(b). Accounting for the combined roughness $3\sigma \approx 1.5$ nm, which is not accounted for in the AB solver solution [7], the distance between the slider and disk solid surfaces is calculated as FH @ PT – 3σ = 6 nm. Since, nom. FH – h_{TFC} + ΔFH = 11 – 12 + 6 = 5 nm, the model prediction of the slider-disk contact is within 1 nanometer of the expected value and serves as quantitative validation of the proposed AB model. The accuracy of this prediction could be further improved with the use of calibrated model parameters, including the exact distances of the read/write elements x_R and x_W with respect to the TFC ellipsoid center.

4.1.7.3: Impulse Shock Results

A 0.25 μN s impulse shock is applied over 5 microseconds starting at 0.6 milliseconds. The maximum impulse force (direction is toward the disk) has a magnitude of 100 mN, while the TFC actuation is kept constant at 5 nm, i.e., sufficiently away from the disk surface. The impulse results in the contact pads coming into instantaneous contact with the disk in addition to the expected contact at the TFC bulge as shown in Figure 4.11.

There is significant penetration into the disk surface at the contact pads, while the maximum magnitude of the contact force (not shown) is slightly larger than the impulse force itself, presumably due to inertial contributions. Recovery from the impulse shock at the TFC bulge is very quick without significant loss of magnetic spacing: the TFC bulge is able to keep tracking the DMW. It should be noted that the ISBL and MTL models give practically identical flyability results, while lubricant contact is too brief to affect system behavior: the slider penetrates the lubricant layer and enters into solid contact with the substrate. Current results agree with previous work in that solid contact should be avoided altogether [10].

The frequency content of the TFC bulge displacement is shown in the wavelet transform (WT) plot of Figure 4.12. While the impulse excites a large range of frequencies, the dominant modes observed correspond to the AB frequencies as well as the DMW at 12 kHz that represents the dynamic motion of the disk. The latter becomes dominant whenever the slider is tracking the disk motion. The observed AB modes correspond to the ~300, 110 and 100 kHz content in the WT for the normal (2nd pitch), pitch (1st pitch) and roll modes respectively. The close proximity of the pitch and roll modes results in their not being clearly distinguishable in Figure 4.12.

4.1.7.4: Variable TFC Actuation Results

A TFC actuation power profile is applied to the heater embedded under the R/W elements to bring them closer to the disk. The actual TFC actuation h_{TFC} can be related to the applied power using equation (4.10) and the pushback factor of Figure 4.3(b) as shown in Figure 4.4(a). The resulting TFC actuation profile, shown in Figure 4.13, is used to simulate realistic TFC behavior. The minimum possible TFC actuation of 5 nm is based on experimental measurements of TFC sliders that show a stylus-like bulge even when the heater is not powered.

Contact occurs only on the TFC bulge. As shown in Figure 4.14, the proposed 3-DOF model shows very good qualitative agreement with experimental observations that predict two zones of significant vibrations before and after steady contact [9-11]. Vibrations in the first zone are larger in magnitude as the TFC bulge is brought into contact with the disk corresponding to "jump-to-contact." This is followed by steady contact during the plateau in TFC actuation where h_{TFC} is constant at 18 nm and finally significant vibrations until "snap-off" as the TFC bulge is retracted. The slider is able to accurately track the DMW outside the two zones with the least amount of vibrations during the steady contact phase. Figure 4.14(a) shows the results of the MTL model while Figure 4.14(b) shows the corresponding results of the ISBL model. The MTL model clearly predicts that the lubricant can support steady contact and solid contact occurs only during the transients of "jump-to-contact" and "snap-off." The ISBL model predicts significantly larger vibrations than the MTL. This occurs because the lubricant can support some of the loading during transient behavior at separations where the adhesion force (within the lubricant) is smaller than what predicted with the ISBL formulation. The net effect is that contact with the lubricant layer provides more damping as shown in Figure 4.14.

Figure 4.15 shows the contact conditions at the interface during variable actuation using the MTL model. During the "jump-to-contact" and "snap-off" transients, the forces are significantly higher than during steady state solid contact. This is clearly reflected in the coefficient of friction, which varies during the transients but has a lower constant value during steady state lubricant contact. The friction coefficient is larger than unity during steady state contact due to the effect of adhesion. Specifically, the net vertical force $F_c - F_s$ (including inertial contributions) determines the value of the maximum friction force, resulting in the friction force being larger than the contact force and dominating the interface.

The friction coefficient time history, shown in Figure 4.15(d), qualitatively correlates well with experimental measurements of contact at the HDI based on acoustic emission (AE) sensing [6, 100]. Overall, the behavior at the HDI agrees with published experimental data that report pure lubricant contact for TFC actuations slightly larger than those required for TD [100]. The presented simulation results for variable actuation predict steady lubricant contact between the "jump-to-contact" and "snap-off" transients. Hence, the hypothesis that the slider's altitude may adjust so as to achieve stable flying with no contact for actuations larger than those required for TD appears to not hold [9, 100].

4.1.7.5: Effect of Lubricant Properties

The MTL model used experimental measurements of the limiting (maximum) viscosity μ_0 for a specific lubricant chemistry and morphology and defined the minimum liquid thickness κ as a measure of the bonded layer thickness [23, 24]. Varying μ_0 allows us to change the effective lubricant layer stiffness, which, for example, could be smaller than the nominal experimental case in the presence of increased temperature or humidity, or larger for more polar lubricants. The minimum liquid thickness, which in the MTL model was correlated to the lubricant molecule radius of gyration, can also be varied to reflect changes in lubricant chemistry.

Table 4.4 lists four cases used in our simulations to investigate the effect of lubricant chemistry and morphology to the contact and flyability at the HDI as well as the resulting vibrations. Case 0 is the nominal case used up to here. Case 1 uses a lubricant layer with 50% decreased viscosity due to temperature or humidity effects. Case 2 corresponds to a 50% stiffer lubricant layer due to

increased polar bonds. Finally, case 3 is the same as case 2 but using a different lubricant chemistry with a 50% increase in the radius of gyration; this results in double the bonded lubricant thickness relative to the nominal case.

The simulation results for variable lubricant properties are summarized in the last column of Table 4.4, where Bouncing Vibrations (BV) or Flying Height Modulation (FHM), defined in previous work [10], are used to quantify the amount of vibrations; BV and FHM refer to contact and flying respectively. While unfavourable mode coupling is a possible cause of increased vibrations at the interface [9], lubricant chemistry and morphology appear to be equally important determinants of transient vibrations. Referring to the nominal and stiffer lubricant cases, the solid forces (shown only for the nominal case in Figure 4.15) have the same magnitude during the "jump-to-contact" and "snap-off" transients. Nevertheless, a stiffer MTL, which can be the result of more polar lubricant or a higher bonding ratio, results in reduced vibrations during contact as shown in Figure 4.16(a), since the lubricant layer is able to contain most of the contact. In contrast, reducing lubricant layer stiffness is worse because of increased solid contact, which induces larger transient vibrations as well. Larger lubricant molecules, featuring a larger radius of gyration or higher molecular weight, diminish the hydrodynamic bearing that the lubricant layer is able to provide, which is proportional to the amount of mobile molecules in the contact; hence, case 3 results in even larger transient vibrations. Experimental measurements of lubricant contact with older, non-TFC sliders have shown that a lower molecular weight and a higher bonding ratio result in reduced slider vibrations [101], while newer experiments suggested that the presence of more mobile molecules results in stable lubricant contact [102]. While these two conclusions appear contradictory, we postulate, based on the presented simulation results, that the determinant is not the ratio of bonded-to-mobile molecules per se, but, rather, the thickness of the bonded lubricant layer. Then, the optimum lubricant layer would feature small radius of gyration molecules, adsorbed on the substrate via polar bonds, and featuring large coverage of the substrate area, thus increasing the bonded ratio while maintaining low bonded layer thickness.

4.2: SUMMARY

A 3-DOF model with lubricant contact was presented and validated using available experimental and simulation data. Multiple POC on the slider ABS were investigated due to the inclusion of the third DOF, roll, to slider motion and were found to be important within the context of operational shock when the contact pads also come into contact with disk in addition to the TFC bulge. The inclusion of lubricant contact was found to be important both for steady contact, where the lubricant bearing allows for near-contact recording, as well as for the transients before and after steady contact where lubricant parameters affect the amount of vibrations at the HDI. Investigation of the effects of lubricant properties revealed that a polar lubricant with small radius of gyration and larger coverage of the substrate would be more beneficial to both contact and flyability at the HDI, while an increase in total lubricant thickness would dampen the transient vibrations during "jump-to-contact."

4.3: FIGURES

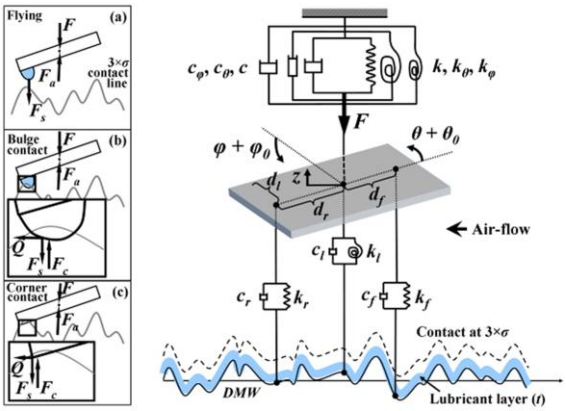


Figure 4.1: Schematic of 3-DOF model. Insets show possible flying (a), TFC bulge contacting (b), and corner contacting (c) states.

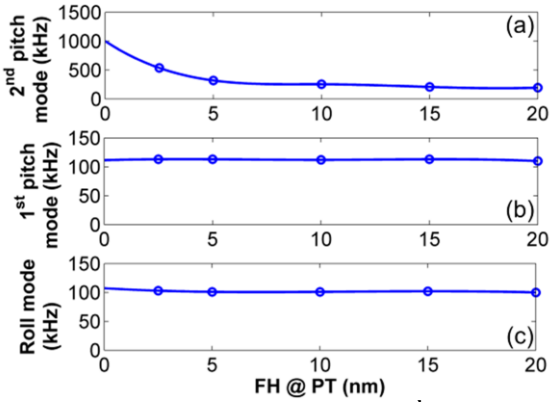


Figure 4.2: Air bearing resonant frequencies in the normal or 2nd pitch (a), 1st pitch (b), and roll DOF (c) as functions of FH @ PT.

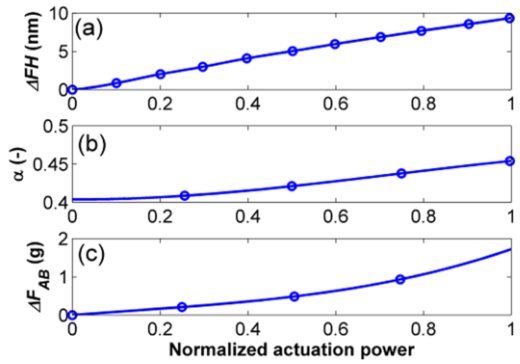


Figure 4.3: AB stiffening with actuation power [7]: (a) change in FH; (b) pushback factor; and (c) AB force increase.

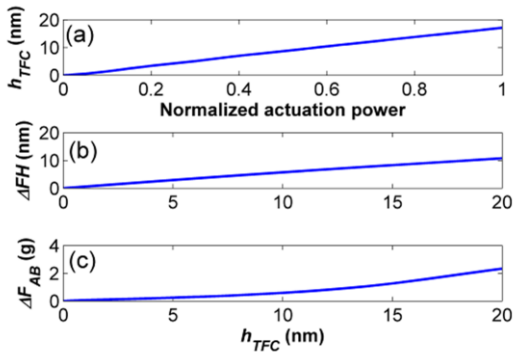


Figure 4.4: AB stiffening as function of actual actuation: (a) actual TFC actuation versus applied power; (b) change in FH versus actual TFC actuation; and (c) AB force increase.

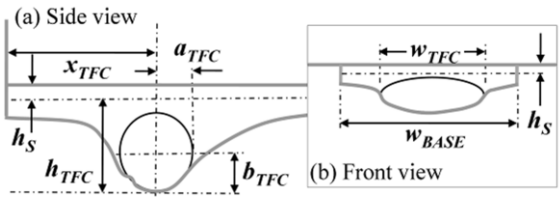


Figure 4.5: Side (a) and front view (b) of the TFC bulge, and surrounding material (not to scale).

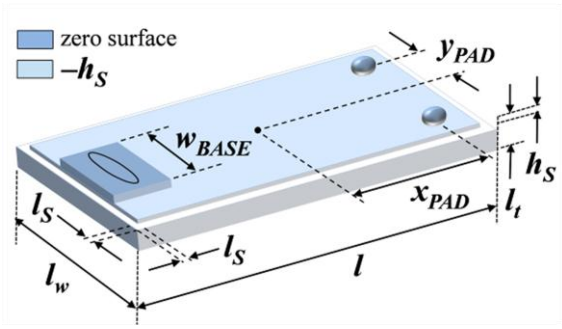


Figure 4.6: ABS topography (not to scale).

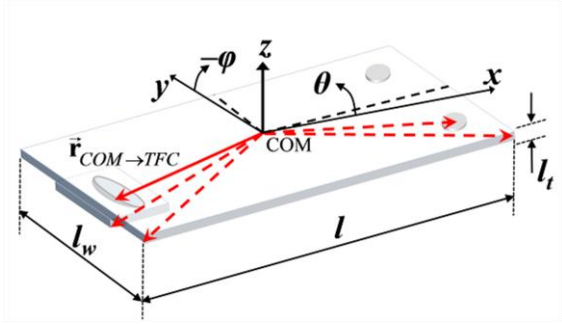


Figure 4.7: Possible POC on the slider (not to scale).

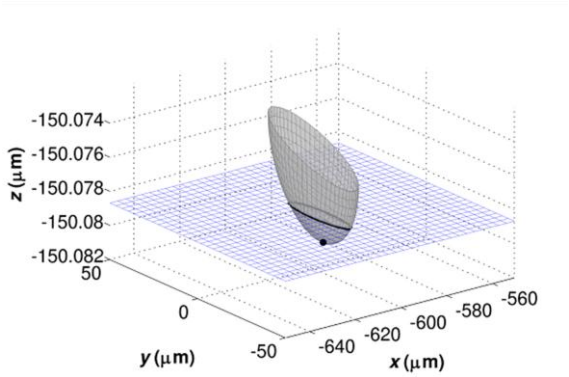


Figure 4.8: Truncation of TFC ellipsoid by cutting plane (high aspect ratio). Also plotted are the POC and cross-sectional ellipse.

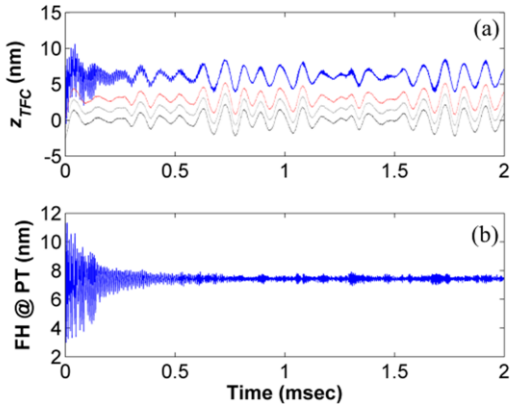


Figure 4.9: Time histories of displacement at the TFC bulge (a), and clearance at the PT (b) for constant actuation.

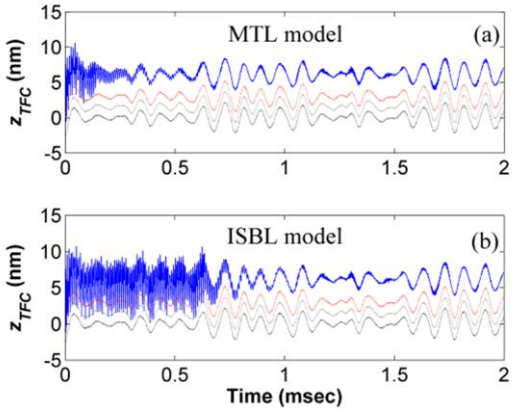


Figure 4.10: Time histories of displacement at the TFC bulge for constant actuation using the MTL (a), and ISBL models (b).

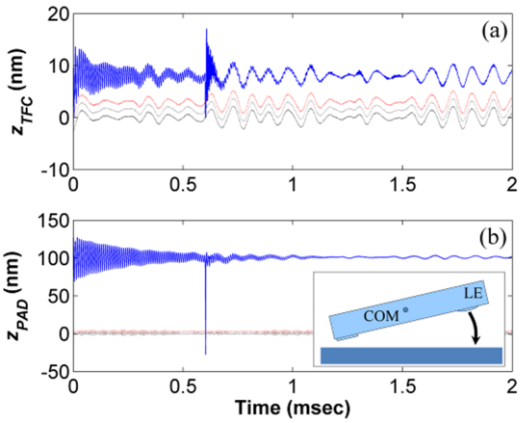


Figure 4.11: Time histories of displacement at the TFC bulge (a), and contact pads (b) under operational shock. The inset shows the motion of the LE that causes contact at the contact pads.

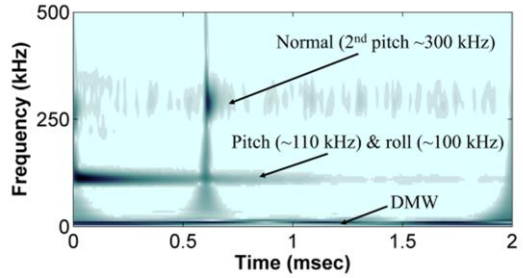


Figure 4.12: Wavelet transform of displacement at the TFC bulge.

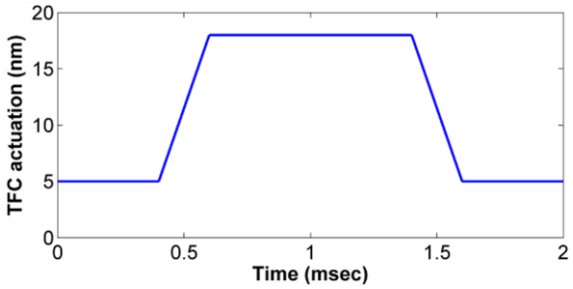


Figure 4.13: Time history of TFC actuation.

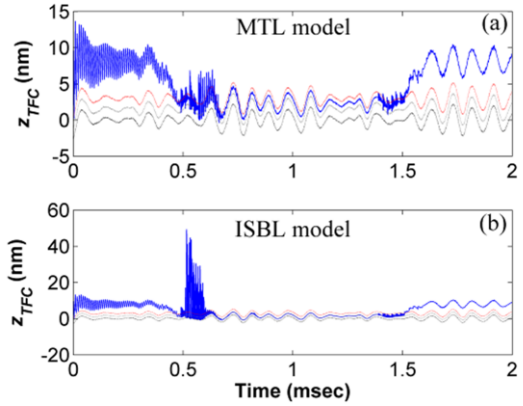


Figure 4.14: Time histories of displacement (a), and clearance (b) at the TFC bulge for variable actuation.

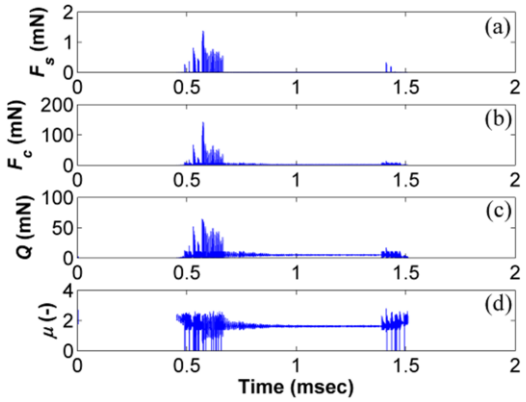


Figure 4.15: Time histories of adhesive (a), contact (b), and friction forces (c), as well as the friction coefficient (d) for variable actuation.

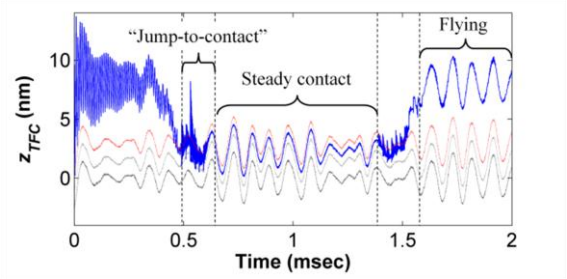


Figure 4.16: Time history of displacement at the TFC bulge for a 50% larger limiting viscosity (stiffer) lubricant under variable actuation. Also shown are the regimes where vibrations were measured as BV or FHM.

4.4: TABLES

Table 4.1: Dynamic contact model parameters for 3-DOF model with lubricant contact.

Symbol	Quantity	Value	Unit
FH_{nom}	Nominal FH	11	nm
FH_{lim}	Limiting FH where AB is lost	22	nm
θ_0	Initial pitch angle	100	μrad
φ_0	Initial roll angle	-10	μrad
m	Slider mass	0.8932	mg
l	Slider length	1.23	mm
l_w	Slider width	0.70	mm
l_t	Slider thickness	0.30	mm
F	Suspension preload	14.7	g
e	Suspension offset	0	mm
k	Suspension normal stiffness	10	N/m
k_θ	Suspension pitch angular stiffness	1.6×10^{-4}	N m/rad
k_φ	Suspension roll angular stiffness	1.6×10^{-4}	N m/rad
ζ	Suspension normal damping ratio	0.02	-
ζ_θ	Suspension pitch damping ratio	0.02	-
ζ_φ	Suspension roll damping ratio	0.02	-
ζ_c	Contact damping ratio	0.005	-
d_f	Offset of front AB spring	$l/2$	mm
d_r	Offset of rear AB spring	$l/2$	mm
ζ_f	Front AB spring damping ratio	0.02	-
ζ_r	Rear AB spring damping ratio	0.02	-
ζ_l	Lateral AB spring damping ratio	0.02	-

Table 4.2: Material and roughness parameters for 3-DOF model with lubricant contact.

Symbol	Quantity	Value	Unit
E_1	Slider Young's modulus	280	GPa
ν_1	Slider Poisson ratio	0.24	-
E_2	Disk Young's modulus	280	GPa
ν_2	Disk Poisson ratio	0.24	-
H	Disk hardness	13	GPa
ε	Equilibrium spacing	0.098	nm
$\Delta\gamma$	Surface energy	0.055	mN/m
t	Total lubricant thickness	1.5	nm
σ_1	Slider RMS roughness	0.340	nm
R_1	Slider mean radius of asperities	0.430	μm
η_1	Slider areal density of asperities	220	μm^{-2}
σ_2	Disk RMS roughness	0.360	nm
R_2	Disk mean radius of asperities	0.534	μm
η_2	Disk areal density of asperities	74.35	μm^{-2}
σ	Combined RMS roughness	0.495	nm
R	Combined mean radius of asperities	0.335	μm
η	Combined areal density of asperities	124	μm^{-2}

Table 4.3: Slider feature parameters for 3-DOF model with lubricant contact.

Symbol	Quantity	Value	Unit
a_{TFC}	TFC ellipsoid semi-width	5	μm
b_{TFC}	TFC ellipsoid height	5	nm
w_{TFC}	TFC ellipsoid width	50	μm
x_{TFC}	TFC ellipsoid offset from TE	15	μm
w_{BASE}	TFC base width	100	μm
x_R	Offset of read transducer on ellipsoid	3	μm
x_W	Offset of write transducer on ellipsoid	3	μm
R_{PAD}	Radius of spherical pad	1	mm
x_{PAD}	x-offset of contact pads	0.6	mm
y_{PAD}	y-offset of contact pads	0.3	mm
l_S	Lateral recession of TE/LE	10	μm
h_S	Step height from zero surface	0.16	μm

Table 4.4: Effect of lubricant properties on vibrations.

Case	Lubricant parameters	Regime	BV / FHM
0	Original case (μ_0 = 0.31 Pa s; κ = 0.3 nm)	"Jump-to-contact"	**61.7%**
		Steady contact (BV)	**5.7%**
		Flying (FHM)	**7.8%**
1	50% decrease in viscosity (μ_0 = 0.16 Pa s; κ = 0.3 nm)	"Jump-to-contact"	623.9%
		Steady contact (BV)	19.4%
		Flying (FHM)	5.9%
2	50% increase in viscosity (μ_0 = 0.46 Pa s; κ = 0.3 nm)	Jump-to-contact	**61.8%**
		Steady contact (BV)	**1.7%**
		Flying (FHM)	**6.4%**
3	50% increase in viscosity and radius of gyration (μ_0 = 0.46 Pa s; κ = 0.45 nm)	"Jump-to-contact"	900.0%
		Steady contact (BV)	23.6%
		Flying (FHM)	6.0%

CHAPTER 5 – CONCLUSIONS

5.1: SUMMARY

Two main contributions are presented in this dissertation: the systematic modeling of TFC nanotechnology sliders, aiming to increase the recording density in magnetic storage; and, a novel, semi-empirical model for contact with MTL layers that exhibit solid-like responses under extremely high shear rates. Sliding contact at the nanoscale was studied, and a methodology was proposed to calculate the interfacial contact, friction and adhesive forces in the presence of roughness, based on the geometry of the contacting surfaces. Contact severity was rigorously characterized, to examine the possibility of operating in the near-contact regime, under the initial assumption that the lubricant layer offered no resistance to shearing. This assumption was relaxed when dynamic shearing experiments, measuring the response of PFPE lubricant sheared between two sliding surfaces, were used to investigate the behavior of MTL layers, and a model was proposed to predict the effective lubricant stiffness. The limits of continuum theory were probed in the formulation of the MTL model, by discussing the applicability of continuum concepts, such as shear rate, within the context of monolayer dynamic contact. The validity of the proposed models was examined through comparison with experimental and atomistic simulation results reported in the literature.

A new flyability parameter was introduced and global optimization algorithms were employed, together with design-of-experiments and analysis-of-variance methods, to optimize TFC slider design for reduced head-media spacing and vibrations. Subsequently, the MTL contact model was integrated into a comprehensive 3-DOF dynamic model that allowed for the study of the effect of lubricant properties on the operating state at the HDI. Results suggest that near-contact or “surfing” recording is possible with the proper design of MTL layers, which affect both the transient “jump-to-contact” response as well the steady state operation within the lubricant. It was found that increased lubricant stiffness and reduced molecule size result in reduced vibrations during transient and steady lubricant contact. Thus, while “true” contact recording remains unobtainable with existing technologies and materials, the work presented in this dissertation suggests that sub-nanometer solid clearances can be achieved with minimal modulation.

5.2: RECOMMENDATIONS FOR FUTURE WORK

Having reached the physical limits of traditional magnetic recording, the presented models and methodologies are expected to be useful in the design and optimization of the HDI for future magnetic recording technologies such as heat-assisted magnetic recording (HAMR) and bit-patterned media recording (BPMR) [103, 104]. Further work is necessary to systematically investigate the effect of temperature and humidity to lubricant and solid contact. Temperature effects in both the lubricant layer and solid surfaces would be especially important within the context of HAMR, while an understanding of contact between patterned surfaces is necessary for BPMR.

Furthermore, modeling assumptions should be investigated and relaxed where possible. For example, the MTL model assumes that the lubricant layer follows the morphology of the substrate, and the presence of lubricant moguls or ripples created by the air shear at small slider-disk separations has not been accounted for [80, 105]. These lubricant modulations would induce changes in the adhesive force and the severity of jump-to-contact behavior; hence, they are responsible for the increase in vibrations with increasing average lubricant layer thickness, an effect that is not captured with the MTL model. In addition, improved solid contact models accounting for the effects of bulk substrate deformation and asperity interaction are also necessary, while contact severity and wear is another aspect that warrants further investigation. The modular nature of the 2- and 3-DOF models allows for the straightforward implementation of improved contact, AB, or geometric components to capture the effects of HAMR or BPMR.

The transition from continuum to atomic scales can be further investigated within the context of MTL layer sliding contact. Stochastic models could potentially be developed to model the regime between hydrodynamic and solid contact via mechanisms such as molecular chain scission. Atomistic simulations, calibrated to match the predictions of dynamic shearing experiments, could also be used to predict lubricant behavior. Hence, the results presented in this dissertation can serve as the starting point in the search for answers to fundamental questions beyond the scope of magnetic storage.

REFERENCES

1. Lee, S.-C. and B.D. Strom, *Characterization of thermally actuated pole tip protrusion for head-media spacing adjustment in hard disk drives.* Transactions of the ASME. Journal of Tribology, 2008. **130**(2): p. 022001-1.
2. Zheng, H., et al., *The effect of write current on thermal flying height control sliders with dual heater/insulator elements.* Microsystem Technologies, 2011: p. 1-6.
3. Fritzsche, J., et al., *The effect of air bearing contour design on thermal pole-tip protrusion.* Microsystem Technologies, 2011: p. 1-8.
4. Zheng, J. and D. Bogy, *Investigation of Flying-Height Stability of Thermal Fly-Height Control Sliders in Lubricant or Solid Contact with Roughness.* Tribology Letters, 2010. **38**(3): p. 283-289.
5. Liu, N., J. Zheng, and D.B. Bogy, *Predicting the flying performance of thermal flying-height control sliders in hard disk drives.* Journal of Applied Physics, 2010. **108**(1): p. 016102.
6. Xu, J. and G. Sheng, *Characterization of light contact in head disk interface with dynamic flying height control.* Microsystem Technologies, 2011. **17**(5): p. 1225-1230.
7. Zheng, J., et al., *Effects of Altitude on Thermal Flying-Height Control Actuation.* Tribology Letters, 2010. **40**(3): p. 295-299.
8. Su, L., et al., *Tribological and Dynamic Study of Head Disk Interface at Sub-1-nm Clearance.* IEEE Transactions on Magnetics, 2011. **47**(1): p. 111-116.
9. Canchi, S.V. and D.B. Bogy, *Thermal fly-height control slider instability and dynamics at touchdown: Explanations using nonlinear systems theory.* Transactions of the ASME. Journal of Tribology, 2011. **133**(2).
10. Vakis, A.I. and A.A. Polycarpou, *Head-disk interface nanotribology for Tbit/in2 recording densities: near-contact and contact recording.* Journal of Physics D: Applied Physics, 2010. **43**(22).
11. Vakis, A.I., S.-C. Lee, and A.A. Polycarpou, *Dynamic Head-Disk Interface Instabilities with Friction for Light Contact (Surfing) Recording.* IEEE Transactions on Magnetics, 2009. **45**(11): p. 4966-4971.
12. Vakis, A.I., C.N. Hadjicostis, and A.A. Polycarpou, *Three-DOF dynamic model with*

lubricant contact for thermal fly-height control nanotechnology. Journal of Physics D: Applied Physics, 2011(Submitted).

13. Vakis, A.I. and A.A. Polycarpou, *Optimization of thermal fly-height control slider geometry for Tbit/in^2 recording.* Microsystem Technologies, 2010. **16**(6): p. 1021-1034.
14. Thornton, B.H., T. Eguchi, and M. Suk, *A Novel HDD "Component-Level" Operational-Shock Measurement Method.* IEEE Transactions on Magnetics, 2007. **43**(6): p. 2316-2318.
15. Yu, S., et al., *Contact-induced off-track vibrations of air bearing-slider-suspension system in hard disk drives.* Tribology Letters, 2006. **24**(1): p. 27-36.
16. Bhargava, P. and D.B. Bogy, *Numerical Simulation of Operational-Shock in Small Form Factor Hard Disk Drives.* Transactions of the ASME. Journal of Tribology, 2007. **129**(1): p. 153-160.
17. Sinha, S.K., M. Kawaguchi, and T. Kato, *Surface profiles and modulation of ultra-thin perfluoropolyether lubricant in contact sliding.* Journal of Physics D: Applied Physics, 2004. **37**(16): p. 2247-2255.
18. Liu, B., et al., *Towards fly- and lubricant-contact recording.* Journal of Magnetism and Magnetic Materials, 2008. **320**(22): p. 3183-3188.
19. Lee, S.-C. and A.A. Polycarpou, *Microtribodynamics of pseudo-contacting head-disk interfaces intended for 1 Tbit/in^2*. IEEE Transactions on Magnetics, 2005. **41**(2): p. 812-18.
20. Hua, W., et al., *Nanoscale roughness contact in a slider-disk interface.* Nanotechnology, 2009. **20**(28): p. 285710 (7 pp).
21. Yu, S.K., et al. *Head Disk Interface Dynamic Stability Analysis for Surfing Recording*. in *Asia-Pacific Magnetic Recording Conference (APMRC)*. 2009. Singapore.
22. Chen, D. and D.B. Bogy, *Dynamics of partial contact head disk interface.* IEEE Transactions on Magnetics, 2007. **43**(6): p. 2220-2.
23. Vakis, A.I., M. Eriten, and A.A. Polycarpou, *Modeling Bearing and Shear Forces in Molecularly Thin Lubricants.* Tribology Letters, 2011. **41**(3): p. 573-586.
24. Vakis, A.I. and A.A. Polycarpou, *Modeling Sliding Contact of Rough Surfaces with Molecularly Thin Lubricants.* Tribology Letters, 2011: p. 1-12.
25. Thornton, B.H. and D.B. Bogy, *Nonlinear aspects of air-bearing modeling and dynamic*

spacing modulation in sub-5-nm air bearings for hard disk drives. IEEE Transactions on Magnetics, 2003. **39**(2): p. 722-8.

26. Zeng, Q.H. and D.B. Bogy, *A simplified 4-DOF suspension model for dynamic load/unload simulation and its application.* Transactions of the ASME. Journal of Tribology, 2000. **122**(1): p. 274-9.
27. Juang, J.Y. and D.B. Bogy, *Nonlinear compensator design for active sliders to suppress head-disk spacing modulation in hard disk drives.* IEEE/ASME Transactions on Mechatronics, 2006. **11**(3): p. 256-264.
28. Stanley, H.M., I. Etsion, and D.B. Bogy, *Adhesion of contacting rough surfaces in the presence of sub-boundary lubrication.* Transactions of the ASME. Journal of Tribology, 1990. **112**(1): p. 98-104.
29. Demirel, A.L. and S. Granick, *Relaxations in molecularly thin liquid films.* Journal of Physics: Condensed Matter, 1996. **8**: p. 9537-9.
30. Fukuzawa, K., S. Itoh, and Y. Mitsuya, *Fiber wobbling shear force measurement for nanotribology of confined lubricant molecules.* IEEE Transactions on Magnetics, 2003. **39**: p. 2453-5.
31. Itoh, S., et al., *Fiber wobbling method for dynamic viscoelastic measurement of liquid lubricant confined in molecularly narrow gaps.* Tribology Letters, 2008. **30**(3): p. 177-89.
32. Guo, Q., et al., *Nano-Rheology of Single Unentangled Polymeric Lubricant Films.* Macromolecular Theory and Simulations, 2008. **17**(9): p. 454-459.
33. Demirel, A.L. and S. Granick, *Transition from static to kinetic friction in a model lubricated system.* Journal of Chemical Physics, 1998. **109**(16): p. 6889-6897.
34. Bonaccurso, E., H.-J. Butt, and V.S.J. Craig, *Surface Roughness and Hydrodynamic Boundary Slip of a Newtonian Fluid in a Completely Wetting System.* Physical Review Letters, 2003. **90**(14): p. 144501.
35. Zhu, Y. and S. Granick, *Limits of the Hydrodynamic No-Slip Boundary Condition.* Physical Review Letters, 2002. **88**(10): p. 106102.
36. Zhu, Y. and S. Granick, *Rate-Dependent Slip of Newtonian Liquid at Smooth Surfaces.* Physical Review Letters, 2001. **87**(9): p. 096105.
37. Martini, A., et al., *Slip at high shear rates.* Physical Review Letters, 2008. **100**(20): p.

206001.

38. Priezjev, N.V. and S.M. Troian, *Molecular Origin and Dynamic Behavior of Slip in Sheared Polymer Films.* Physical Review Letters, 2004. **92**(1): p. 018302.
39. Barrat, J.L. and L. Bocquet, *Large slip effect at a nonwetting fluid-solid interface.* Physical Review Letters, 1999. **82**(23): p. 4671-4.
40. Thompson, P.A. and S.M. Troian, *A general boundary condition for liquid flow at solid surfaces.* Nature, 1997. **389**(6649): p. 360-2.
41. Hu, H.-W., S. Granick, and K.S. Schweizer, *Static and dynamical structure of confined polymer films.* Journal of Non-Crystalline Solids, 1994. **172-174**: p. 721-728.
42. Peachey, J., J. Van Alsten, and S. Granick, *Design of an apparatus to measure the shear response of ultrathin liquid films.* Review of Scientific Instruments, 1991. **62**(2): p. 463-73.
43. Fukuzawa, K., et al., *Monolithically fabricated double-ended tuning-fork-based force sensor.* Journal of Applied Physics, 2006. **99**(9): p. 094901.
44. Fukuzawa, K., et al., *Simultaneously Measuring Lateral and Vertical Forces with Accurate Gap Control for Clarifying Lubrication Phenomena at Nanometer Gap.* Tribology Letters, 2009. **37**(3): p. 497-505.
45. Suh, A.Y. and A.A. Polycarpou, *Adhesive contact modeling for sub-5-nm ultralow flying magnetic storage head-disk interfaces including roughness effects.* Journal of Applied Physics, 2005. **97**(10): p. 104328-1.
46. Yeo, C.-D., et al., *Friction Force Measurements and Modeling in Hard Disk Drives.* IEEE Transactions on Magnetics, 2008. **44**(1): p. 157-162.
47. Suh, A.Y., et al., *Experimental and theoretical evaluation of friction at contacting magnetic storage slider-disk interfaces.* Tribology Letters, 2006. **23**(3): p. 177-90.
48. Suh, A.Y., S.-C. Lee, and A.A. Polycarpou, *Design optimization of ultra-low flying head-disk interfaces using an improved elastic-plastic rough surface model.* Transactions of the ASME. Journal of Tribology, 2006. **128**(4): p. 801-810.
49. Israelachvili, J., *Intermolecular and Surface Forces, Second Edition: With Applications to Colloidal and Biological Systems (Colloid Science)*1992: Academic Press.
50. Knigge, B., O. Ruiz, and P. Baumgart. *Minimum stable flying height with thermal protrusion actuation*. in *Asia-Pacific Magnetic Recording Conference 2006, APMRC*

2006, Nov 29-Dec 1 2006. 2006. Piscataway, NJ 08855-1331, United States: Institute of Electrical and Electronics Engineers Computer Society.

51. Fan, Z., Z. Zhang, and H. Tang. *Study of Head-Disk Interaction and Spacing Based on Readback Signal*. in *Asia-Pacific Magnetic Recording Conference (APMRC)*. 2009. Singapore.
52. Wood, R.W., J. Miles, and T. Olson. *Recording technologies for terabit per square inch systems*. in *North American Perpendicular Magnetic Recording Conference (NAPMRC), 7-9 Jan. 2002. IEEE Transactions on Magnetics.* 2002. USA: IEEE.
53. Suh, A.Y. and A.A. Polycarpou, *Design optimization of sub-5 nm Head-Disk Interfaces using a two-degree-of-freedom dynamic contact model with friction.* International Journal of Product Development, 2008. **5**(3-4): p. 268-91.
54. Katta, R.R., et al., *Analytical and Experimental Elastic-Plastic Impact Analysis of a Magnetic Storage Head-Disk Interface.* Journal of Tribology, 2009. **131**(1): p. 011902.
55. Katta, R.R., et al., *High Velocity Oblique Impact and Coefficient of Restitution for Head Disk Interface Operational Shock.* Journal of Tribology, 2009. **131**(2): p. 021903.
56. Yu, N., A.A. Polycarpou, and J.V. Hanchi, *Elastic contact mechanics-based contact and flash temperature analysis of impact-induced head disk interface damage.* Microsystem Technologies, 2008. **14**(2): p. 215-27.
57. Zhou, W.D., et al., *Effects of temperature dependent air properties on the performances of a thermal actuated slider.* Tribology International, 2009. **42**(6): p. 902-910.
58. Greenwood, J. and J. Williamson, *Contact of Nominally Flat Surfaces.* Proceedings of the Royal Society of London. Series A: Mathematical and Physical Sciences, 1966. **295**(1442): p. 300-319.
59. Yu, N. and A.A. Polycarpou, *Adhesive contact based on the Lennard-Jones potential: A correction to the value of the equilibrium distance as used in the potential.* Journal of Colloid and Interface Science, 2004. **278**(2): p. 428-435.
60. Zhang, S., et al., *Air bearing surface designs in consideration of thermomechanical actuation efficiency.* Transactions of the ASME. Journal of Tribology, 2008. **130**(4): p. 041901.
61. Greenwood, J.A. and J.H. Tripp, *Elastic contact of rough spheres.* American Society of Mechanical Engineers -- Transactions -- Journal of Applied Mechanics, 1967. **34**(1): p.

153-159.

62. Mate, C.M., et al., *Will the numbers add up for sub-7-nm magnetic spacings? Future metrology issues for disk drive lubricants, overcoats, and topographies.* IEEE Transactions on Magnetics, 2005. **41**(2): p. 626-31.
63. Johnson, K.L., *Contact mechanics*1985, Cambridge, UK: Cambridge University Press.
64. Katta, R.R., et al., *Plane strain sliding contact of multilayer magnetic storage thin-films using the finite element method.* Microsystem Technologies, 2009. **15**(7): p. 1097-1110.
65. Liu, B., et al., *Low flying-height slider with high thermal actuation efficiency and small flying-height modulation caused by disk waviness.* IEEE Transactions on Magnetics, 2008. **44**(1): p. 145-50.
66. Peng, W. and B. Bhushan, *Three-dimensional contact analysis of layered elastic/plastic solids with rough surfaces.* Wear, 2001. **249**(Copyright 2001, IEE): p. 741-60.
67. DeVor, R.E., T.-h. Chang, and J.W. Sutherland, *Statistical Quality Design and Control: Contemporary Concepts and Methods*1992, Upper Saddle River, NJ: Prentice-Hall, Inc.
68. Minn, M., et al., *High-speed tribology of PFPEs with different functional groups and molecular weights coated on DLC.* Tribology Letters, 2006. **24**(1): p. 67-76.
69. Itoh, S., et al., *Spreading properties of monolayer lubricant films: effect of bonded molecules.* IEEE Transactions on Magnetics, 2009. **45**(11): p. 5055-60.
70. Thompson, P.A., M.O. Robbins, and G.S. Grest, *Structure and Shear Response in Nanometer-Thick Films.* Israel Journal of Chemistry, 1995. **35**(1): p. 93-106.
71. Dhinojwala, A. and S. Granick, *Surface forces in the tapping mode: Solvent permeability and hydrodynamic thickness of adsorbed polymer brushes.* Macromolecules, 1997. **30**(4): p. 1079-1085.
72. Kogut, L. and I. Etsion, *A semi-analytical solution for the sliding inception of a spherical contact.* Transactions of the ASME. Journal of Tribology, 2003. **125**(3): p. 499-506.
73. Yeo, C.-D., et al., *Nanomechanical properties of sub-10 nm carbon film overcoats using the nanoindentation technique.* Journal of Materials Research, 2007. **22**(1): p. 141-151.
74. Demirel, A.L. and S. Granick, *Origins of solidification when a simple molecular fluid is confined between two plates.* Journal of Chemical Physics, 2001. **115**(3): p. 1498-512.
75. Goldman, A.J., R.G. Cox, and H. Brenner, *Slow viscous motion of a sphere parallel to a plane wall. I. Motion through a quiescent fluid.* Chemical Engineering Science, 1967.

22(4): p. 637-652.

76. Brinson, H. and C. Brinson, *Polymer Engineering Science and Viscoelasticity: An Introduction*2007, New York: Springer.
77. Vinogradova, O.I., *Drainage of a thin liquid film confined between hydrophobic surfaces.* Langmuir, 1995. **11**(6): p. 2213-2213.
78. Williams, J., *Engineering Tribology*2005: Cambridge University Press.
79. Stahl, J. and B.O. Jacobson, *A lubricant model considering wall-slip in EHL line contacts.* Transactions of the ASME. Journal of Tribology, 2003. **125**(3): p. 523-32.
80. Marchon, B., et al., *The physics of disk lubricant in the continuum picture.* IEEE Transactions on Magnetics, 2005. **41**(2): p. 616-20.
81. Mate, C.M. and B. Marchon, *Shear response of molecularly thin liquid films to an applied air stress.* Physical Review Letters, 2000. **85**(18): p. 3902-5.
82. Mate, C.M., M.F. Toney, and K.A. Leach, *Roughness of thin perfluoropolyether lubricant films: influence on disk drive technology.* IEEE Transactions on Magnetics, 2001. **37**(4): p. 1821-1823.
83. Pit, R. and B. Marchon, *Direct measurement of lubricant relaxation on a disk surface.* IEEE Transactions on Magnetics, 2001. **37**(4): p. 1830-1832.
84. Suh, A.Y. and A.A. Polycarpou, *Effect of molecularly thin lubricant on roughness and adhesion of magnetic disks intended for extremely high-density recording.* Tribology Letters, 2003. **15**(4): p. 365-76.
85. Ciavarella, M., J.A. Greenwood, and M. Paggi, *Inclusion of "interaction" in the Greenwood and Williamson contact theory.* Wear, 2008. **265**(5-6): p. 729-34.
86. Greenwood, J.A., *A simplified elliptic model of rough surface contact.* Wear, 2006. **261**(2): p. 191-200.
87. Ciavarella, M., V. Delfine, and G. Demelio, *A "re-vitalized" Greenwood and Williamson model of elastic contact between fractal surfaces.* Journal of the Mechanics and Physics of Solids, 2006. **54**(12): p. 2569-2591.
88. Yu, N. and A.A. Polycarpou, *Contact of rough surfaces with asymmetric distribution of asperity heights.* Transactions of the ASME. Journal of Tribology, 2002. **124**(2): p. 367-76.
89. Bush, A.W., R.D. Gibson, and T.R. Thomas, *The elastic contact of a rough surface.*

Wear, 1975. **35**(1): p. 87-111.

90. Gee, M.L., et al., *Liquid to solidlike transitions of molecularly thin films under shear.* Journal of Chemical Physics, 1990. **93**(3): p. 1895-906.
91. Shi, X. and A.A. Polycarpou, *Investigation of contact stiffness and contact damping for magnetic storage head-disk interfaces.* Transactions of the ASME. Journal of Tribology, 2008. **130**: p. 1-9.
92. Kogut, L. and I. Etsion, *A static friction model for elastic-plastic contacting rough surfaces.* Transactions of the ASME. Journal of Tribology, 2004. **126**(1): p. 34-40.
93. Tani, H., K. Sakamoto, and N. Tagawa, *Conformation of ultrathin PFPE lubricants with different structure on magnetic disks - direct observation and MD simulation.* IEEE Transactions on Magnetics, 2009. **45**(11): p. 5050-4.
94. Waltman, R.J., et al., *Investigation of a new cyclotriphosphazene-terminated perfluoropolyether lubricant. Properties and interactions with a carbon surface.* Chemistry of Materials, 2003. **15**(12): p. 2362-2375.
95. Lei, R.Z. and A.J. Gellman, *Humidity effects on PFPE lubricant bonding to a-CHx overcoats.* Langmuir, 2000. **16**(16): p. 6628-35.
96. Choi, H.J., et al., *Molecular rheology of perfluoropolyether lubricant via nonequilibrium molecular dynamics simulation.* IEEE Transactions on Magnetics, 2007. **43**(2): p. 903-5.
97. Marchon, B., et al., *Lubricant dynamics on a slider: "the waterfall effect".* Journal of Applied Physics, 2009. **105**(7).
98. Zhou, W., et al., *Effects of environmental temperature and humidity on thermal flying height adjustment.* Microsystem Technologies, 2010. **16**(1): p. 49-55.
99. Juang, J. and D.B. Bogy, *Air-bearing effects on actuated thermal pole-tip protrusion for hard disk drives.* Transactions of the ASME. Journal of Tribology, 2007. **129**(3): p. 570-8.
100. Canchi, S.V. and D.B. Bogy, *Slider dynamics in the lubricant-contact regime.* IEEE Transactions on Magnetics, 2010. **46**(1): p. 764-9.
101. Dai, Q., et al., *Time evolution of lubricant-slider dynamic interactions.* IEEE Transactions on Magnetics, 2003. **39**(5): p. 2459-2461.
102. Tani, H., T. Yamaguchi, and N. Tagawa, *Experimental Study of Head-Disk Interface Instability on Light Contact Recording Using Dynamic Flying Height Control.* IEEE

Transactions on Magnetics, 2011. **47**(1): p. 117-123.

103. Hellwig, O., et al., *Bit patterned media based on block copolymer directed assembly with narrow magnetic switching field distribution.* Applied Physics Letters, 2010. **96**(5): p. 052511.
104. Challener, W.A., et al., *Heat-assisted magnetic recording by a near-field transducer with efficient optical energy transfer.* Nature Photonics, 2009. **3**(4): p. 220-224.
105. Pit, R., et al., *Formation of lubricant moguls at the head/disk interface.* Tribology Letters, 2001. **10**(3): p. 133-42.
106. Knigge, B. and F.E. Talke, *Slider Vibration Analysis at Contact Using Time-Frequency Analysis and Wavelet Transforms.* Transactions of the ASME. Journal of Tribology, 2001. **123**(3): p. 548-554.
107. Knigge, B.E., et al., *Influence of contact potential on slider-disk spacing: simulation and experiment.* IEEE Transactions on Magnetics, 2004. **40**(4): p. 3165-3167.
108. Lee, K.M. and A.A. Polycarpou, *Dynamic microwaviness measurements of super smooth disk media used in magnetic hard disk drives.* Mechanical Systems and Signal Processing, 2006. **20**(6): p. 1322-1337.
109. Lee, S.-C. and A.A. Polycarpou, *Effect of hard-disk drive spindle motor vibration on dynamic microwaviness and flying-height modulation.* Tribology International, 2005. **38**(6-7): p. 665-674.
110. Chang, W.R., I. Etsion, and D.B. Bogy, *An elastic-plastic model for the contact of rough surfaces.* Transactions of the ASME. Journal of Tribology, 1987. **109**(2): p. 257-63.
111. Suh, A.Y., A.A. Polycarpou, and T.F. Conry, *Detailed surface roughness characterization of engineering surfaces undergoing tribological testing leading to scuffing.* Wear, 2003. **255**(1-6): p. 556-568.

APPENDIX A

A.1: ISBL CONTACT MODEL EQUATIONS

The following are the expressions of the solid adhesion, contact and friction forces of the ISBL model. These are to be added to the lubricant adhesion, contact and friction forces of the MTL model to yield the total forces. The solid adhesive force comprises the contributions of elastically and elastically-plastically contacting asperities. It is a function of the maximum surface energy, as well as the radius and number of asperities in contact:

$$F_{s,solid} = 2\pi RN \max(\Delta\gamma)\left[0.98\int_{d}^{d+\omega} J_{-0.29}^{0.298} + 0.79\int_{d+\omega}^{d+6\omega} J_{-0.321}^{0.356} + 1.19\int_{d+6\omega}^{d+110\omega} J_{-0.332}^{0.093}\right] \quad \text{(A.1)}$$

The integrands are defined as

$$J_c^b = \left(\frac{\omega}{\omega_c}\right)^b \left(\frac{\varepsilon}{\omega_c}\right)^c \varphi(z)\,dz \quad \text{(A.2)}$$

The local and critical interference of each asperity is ω and ω_c respectively, while ε is the equilibrium spacing. A Gaussian distribution of asperity heights φ (z) is assumed.

The solid contact force is

$$P_{solid} = \frac{2}{3}(\pi RKH\omega_c) N\left[\int_{d}^{d+\omega_c} I^{1.5} + 1.03\int_{d+\omega_c}^{d+6\omega_c} I^{1.425} + 1.4\int_{d+6\omega_c}^{d+110\omega_c} I^{1.263} + \frac{3}{K}\int_{d+110\omega_c}^{\infty} I^{1}\right] \quad \text{(A.3)}$$

The solid contact force includes contributions from elastically, elastically-plastically and fully plastically deforming asperities. The hardness is H and the hardness coefficient is K = 0.454+0.41ν. The critical interference is

$$\omega_c = \left(\frac{\pi KH}{2E^*}\right)^2 R \quad \text{(A.4)}$$

where E^* is the combined elastic modulus at the interface

$$E^* = \left[\left(\frac{1-\nu_1^{\,2}}{E_1} \right) + \left(\frac{1-\nu_2^{\,2}}{E_2} \right) \right]^{-1} \tag{A.5}$$

The solid friction force is

$$Q_{solid} = \frac{2}{3}(\pi RKH\omega_c) N \left[0.52 \int_d^{d+\omega_c} I^{0.982} + \int_{d+\omega_c}^{d+6\omega_c} -0.01 I^{4.425} + 0.091 I^{3.425} + 0.85 I^{1.425} \right] \tag{A.6}$$

and the real area of contact is

$$A_{r,solid} = (\pi R\omega_c) N \left[\int_d^{d+\omega_c} I^1 + 0.93 \int_{d+\omega_c}^{d+6\omega_c} I^{1.136} + 0.94 \int_{d+6\omega_c}^{d+110\omega_c} I^{1.146} + 2 \int_{d+110\omega_c}^{\infty} I^1 \right] \tag{A.7}$$

The integrands are

$$I^b = \left(\frac{z-d}{\omega_c} \right)^b \varphi(z)\, dz \tag{A.8}$$

A.2: MTL CONTACT MODEL EQUATIONS

The MTL model utilizes the solid force formulations of the ISBL model and includes lubricant contact as well as a variable surface energy for the lubricant. The expressions for the stiffnesses can be rewritten as functions of the mean plane separation h as:

$$k_P = \frac{m_P P_0}{U\dot{\gamma}_0^{\,m_P}}\dot{\gamma}^{m_P+1} = \frac{m_P P_0}{U\dot{\gamma}_0^{\,m_P}}\left(\frac{U}{h-3\sigma-\kappa}\right)^{m_P+1} \tag{A.9}$$

$$k_Q = \frac{n_Q}{U\ln(10)}\dot{\gamma} = \frac{n_Q}{\ln(10)}\left(h-3\sigma-\kappa\right)^{-1} \tag{A.10}$$

In the absence of displacement control, the minimum liquid gap κ is assumed to be equal to the radius of gyration of the lubricant molecules, i.e. $\kappa = r_g = 0.3$ nm. The constants m_P and n_Q are fitting coefficients calculated from the lubricant response to dynamic shearing experiments with a maximum (achievable) experimental shear rate $\dot{\gamma}_0 = 2\times10^5$ s^{-1}. P_0 is the maximum experimentally measured normal force that corresponds to a critical viscosity μ_0. For example, based on the experimental data of Fukuzawa *et al.*, the fitting coefficients are $m_P = 0.5$ and $n_Q = 1.46\times10^{-7}$, while the critical viscosity is $\mu_0 = 0.31$ Pa s. The maximum experimental normal force is calculated as:

$$P_0 = \frac{6\pi}{5}\mu_0 U_0\sqrt{\frac{2R_0^{\,3}}{\kappa}} \tag{A.11}$$

For an average experimental shearing velocity $U_0 = 200$ μm/s and a spherical probe radius $R_0 = 102$ μm, equation (A.11) yields $P_0 = 10.77$ μN.

The normal and shear stiffnesses for solid contact can be calculated as the slopes of the force-separation curves:

$$k_c = \left|\frac{\Delta P}{\Delta h}\right| \tag{A.12}$$

$$k_{fr} = \left| \frac{\Delta Q}{\Delta h} \right| \tag{A.13}$$

The formulations of the solid contact and friction forces are based on the ISBL model. The MTL model assumes hydrodynamic contact for mean plane separations $3\sigma+2\kappa \leq h < 3\sigma+t$ and solid contact for $h < 3\sigma$. Hence, the transition over the bonded layer thickness for $3\sigma \leq h < 3\sigma+2\kappa$ is modeled using the following linear equations:

$$k_{c-P} = \left| \frac{k_P\left(\dot{\gamma} = \dot{\gamma}_{\max}\right) - k_c\left(h = 3\sigma\right)}{2\kappa} \right| h \tag{A.14}$$

$$k_{fr-Q} = \left| \frac{k_Q\left(\dot{\gamma} = \dot{\gamma}_{\max}\right) - k_{fr}\left(h = 3\sigma\right)}{2\kappa} \right| h \tag{A.15}$$

The maximum shear rate for the nominal case examined in the present work is calculated as the ratio U/κ and is equal to 6×10^{10} s^{-1}. The normal and shear stiffnesses transition from the maximum hydrodynamic values for $\dot{\gamma}_{\max} = U/\kappa$ to the solid stiffnesses at the inception of solid contact for $h = 3\sigma$.

The MTL model also includes a variable surface energy formulation based on experimental measurements, as opposed to the constant value assumed in the ISBL model.

$$\Delta\gamma = \Delta\gamma\left(h_0\right) = c_1 \exp\left(-c_2 t\right) + c_3 \tag{A.16}$$

The fitting coefficients c_1, c_2 and c_3 are 42.84 mN/m, 2.41 nm^{-1} and 14.54 mN/m respectively. The surface energy reaches its maximum value when the mean place separation becomes equal to the equilibrium spacing, i.e. $h = \varepsilon$.

APPENDIX B

B.1: THE ROLE OF DYNAMIC EXCITATION

During slider flying and transition to contact, nonlinearities enter in the form of AB stiffnesses and interfacial adhesive forces. The normal (2^{nd} pitch mode) AB stiffness in particular is highly nonlinear for sub-5-nm FHs [25]. This nonlinearity is exacerbated further by the presence and actuation of the TFC bulge; the increase in normal AB stiffness increases nonlinearly with actuation [7, 10, 12]. The adhesive force is inherently nonlinear and increases sharply with decreasing separation. This effect is captured sufficiently with the use of the Lennard-Jones potential used, for example, in the adhesive force calculations of the ISBL model. Recent experimental measurements of surface free energy at the HDI [46], which were implemented in the MTL model [24], reveal that $\Delta\gamma$ is itself nonlinear with respect to separation and reaches its maximum value at the equilibrium spacing. Finally, during contact, the lubricant and solid forces change nonlinearly with respect to the interference. Behavior at the HDI is expected to be even more convoluted when the interface transitions between flying and solid contact during actuation and retraction as was shown in experiments and simulations [5, 9, 12].

The excitation to the system is the dynamic microwaviness (DMW), which is the motion of the rotating disk and comprises the disk roughness in a dynamic sense together with secondary effects such as spindle vibrations [11]. The experimentally measured DMW signal is quasi-periodic, its spectrum consisting of incommensurate frequencies. To identify the effect of the dynamic excitation input, and in addition to the presented simulations of the 3-DOF model utilizing DMW, simulations were performed for constant and variable TFC actuation with two additional inputs: a pure sinusoidal (periodic) signal; and, zero excitation. Figure B.1 shows the DMW and pure sinusoidal input time histories (a, h), Fast Fourier Transform (FFT) plots (b, g), Wavelet Transform (WT) plots (c, f), and Poincaré plots (d, e). Poincaré sections were constructed by extracting the displacement values for zero velocity (within the half-period of the motion) from the phase space plots and their evolution was plotted. As one would expect, these plots show the quasi-periodic nature of the DMW and the periodic nature of the pure sinusoidal excitation.

The resonant frequency of the DMW at 10.7 kHz dominates the flying response, as shown in both the FFT and WT plots of Figure B.2(b, f) and (c), reflecting the fact that the slider faithfully tracks the disk motion. The 1st pitch AB mode is clearly discernible at 109.5 kHz, while the roll AB mode at ~100 kHz shows up as a smaller peak to the left of the 1st pitch mode in Figure B.2(f). The normal (2nd pitch) AB mode is also shown clearly around the 275 kHz peak, but its amplitude is smaller than that of the 1st pitch mode; the broader peak is due to its inherent nonlinearity. The phase space and Poincaré plots of Figure B.2(d) and (e) demonstrate the quasi-periodic nature of the response. The time-domain signal of variable TFC actuation simulations was truncated between 0.7 and 1.3 milliseconds to focus solely on steady lubricant contact and the FFT and Poincaré plots are shown in Figure B.3. During lubricant contact, the slider again follows the disk motion with peaks in the FFT plot corresponding to the DMW and 1st pitch AB mode vibrations, while the Poincaré plot shows that the response is again quasi-periodic.

The same methodology was followed for the sinusoidal and zero excitations and the results are shown in Figures B.4 to B.7. As expected, the slider again faithfully tracks the disk motion, while the nature of the excitation is reflected in the slider response during both flying and lubricant contact. Specifically, periodic sinusoidal excitation yields a periodic response, while, in the absence of excitation, the response tends to a fixed point. From the FFT plots we can also surmise that the 1st pitch AB mode dominates the vibrations. In fact, the normal (2nd pitch) and roll modes are not discernible, except in the experimentally measured DMW case. In the absence of excitation, the 1st pitch mode and its harmonics dominate the response during the initial transients (these arise from the simulation initial conditions) as shown in Figure B.6.

Additional simulations were performed to investigate the effect of frequency content in the dynamic excitation on the response. The suspension bending and torsional modes lie within the range of 0.3 to 3 kHz [16], while the bending and torsional modes of the slider range between 1.2 and 1.6 MHz [106]. Hence, an input signal was generated with a frequency bandwidth of 10-50 kKz, safely away from the AB modes of the slider, and a second input signal was generated with a bandwidth of 80-320 kHz, overlapping with the AB mode bandwidth. The responses for each are shown in Figure B.8. As expected, the low bandwidth input signal excited primarily the 1st pitch mode and its harmonics as shown in Figure B.8(a-c). The response to the higher bandwidth

input signal, shown in Figure B.8(d-f), features significantly higher vibrations with clearly discernible peaks at each of the AB modes, including roll and normal (2^{nd} pitch). A third simulation for even higher frequency content (350-450 kHz, not shown) yielded even larger vibrations. It appears that the highly nonlinear normal (2^{nd} pitch) AB mode, which varies with FH between ~200 and ~1,000 kHz (refer to Figure 4.2 in Chapter 4) dominates the response for frequencies higher than ~200 kHz and exacerbates the vibrations at the HDI.

This behavior is also evident in the frequency sweep response of Figure B.9(c), where the excitation frequency was varied between 40 and 500 kHz, using the quadratic chirp signal of Figure B.9(a), corresponding to published experimental measurements [107]. Two regions are identified, as shown in Figure B.9(c), were the excitation frequencies don't overlap with the AB modes: region I for frequencies smaller than 90 kHz; and, region II for excitation frequencies between 120 and 240 kHz. Contact occurs when the pitch AB mode is excited at ~110 kHz (0.75 msec), as reported in the literature [107].

In conclusion, the type of dynamic excitation – quasi-periodic, periodic, or fixed – may dictate the slider response, but does not control the state of vibrations since the slider can always accurately track the disk motion. On the contrary, the frequency content of the excitation affects the vibrations, such that, for example, a low waviness input with frequencies of the order of tens of kHz would result in diminished vibrations. Since the 1^{st} pitch mode dominates slider response, increasing the frequency content of the dynamic excitation at and beyond the ~110 kHz results in significantly increased vibrations, affecting the recording signal quality and possibly inducing catastrophic slider-disk contact.

B.2: FIGURES

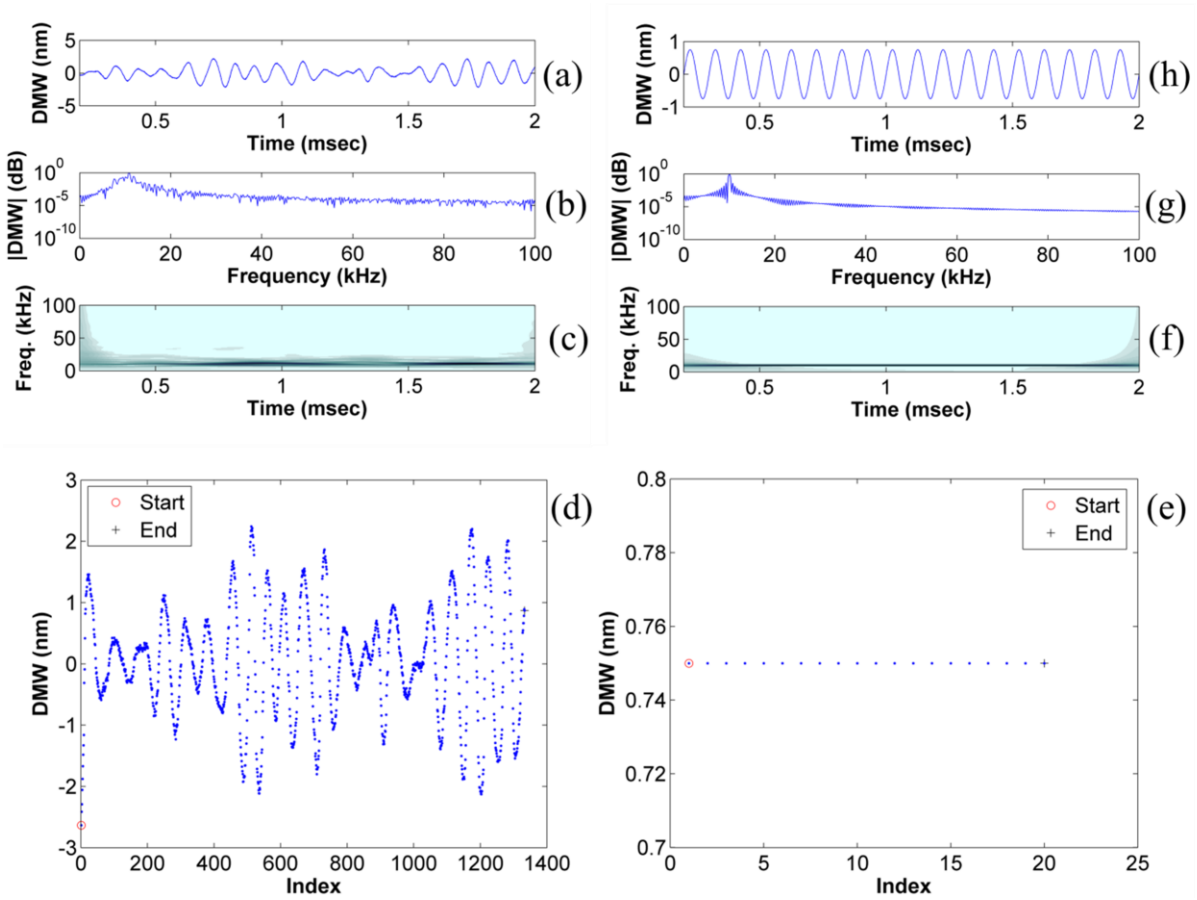


Figure B.1: Experimentally measured DMW (a-d) and pure sinusoidal excitation (e-h): time domain signals (a, h); FFT plots (b, g); WT plots (c, f); and, Poincaré plots (d, e).

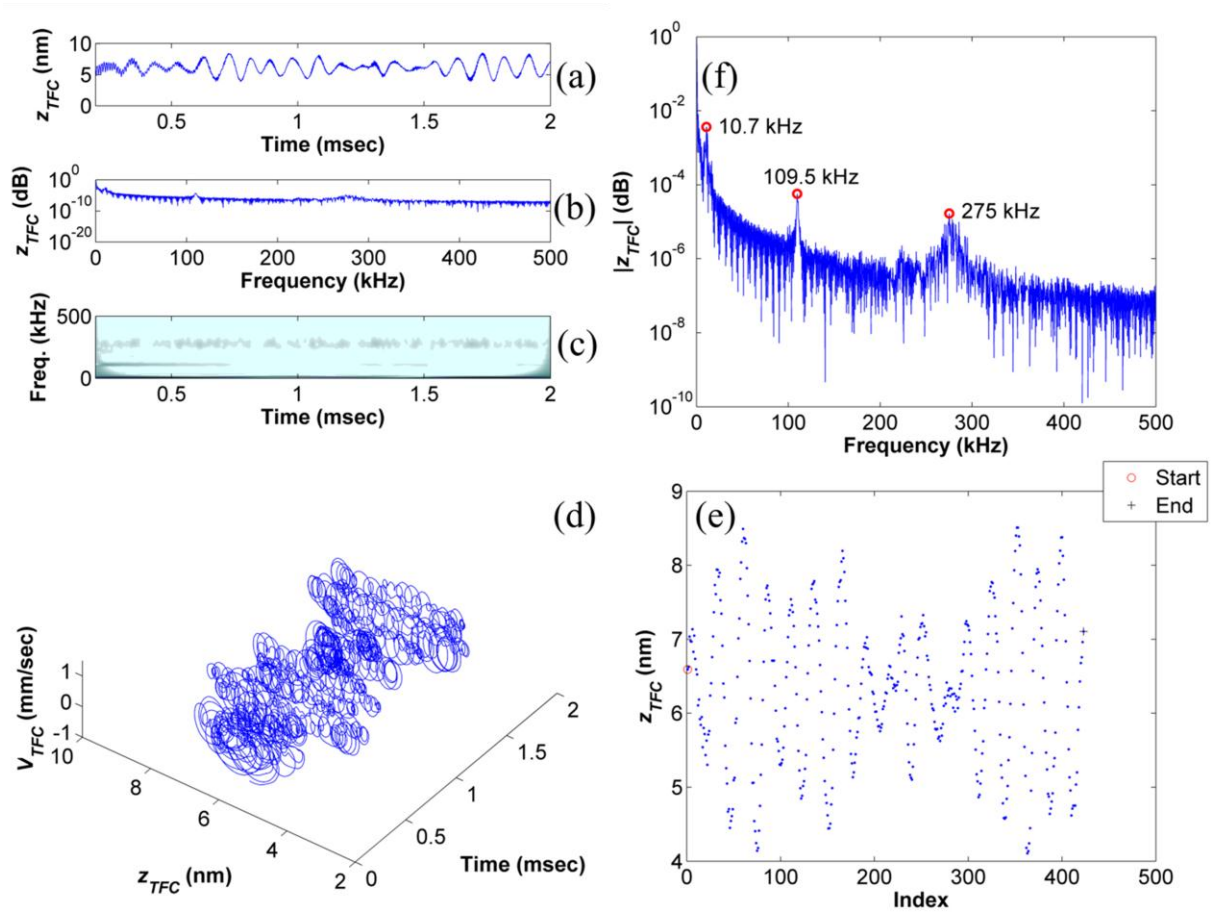


Figure B.2: Slider response for experimentally measured DMW: time domain signal (a); FFT plot (b); WT plot (c); phase space plot (d); Poincaré plot (e); and, close-up of FFT (f).

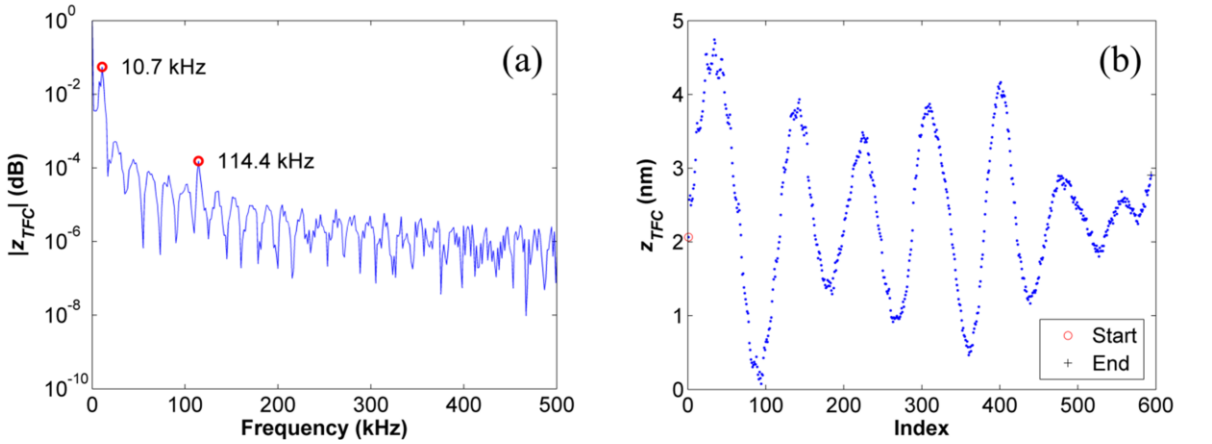


Figure B.3: Steady lubricant contact response for experimentally measured DMW and variable TFC actuation: FFT plot (a); and, Poincaré plot (b).

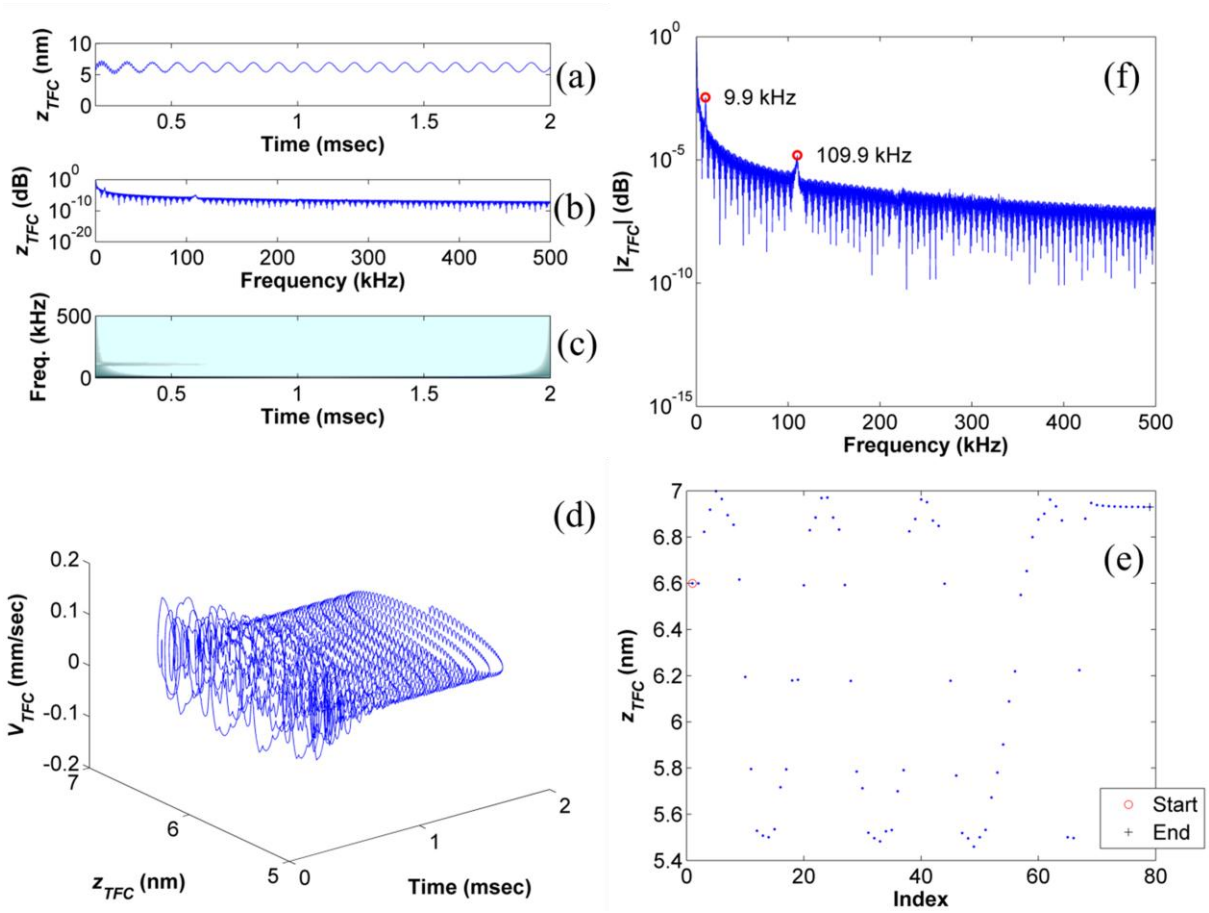


Figure B.4: Slider response for pure sinusoidal excitation: time domain signal (a); FFT plot (b); WT plot (c); phase space plot (d); Poincaré plot (e); and, close-up of FFT (f).

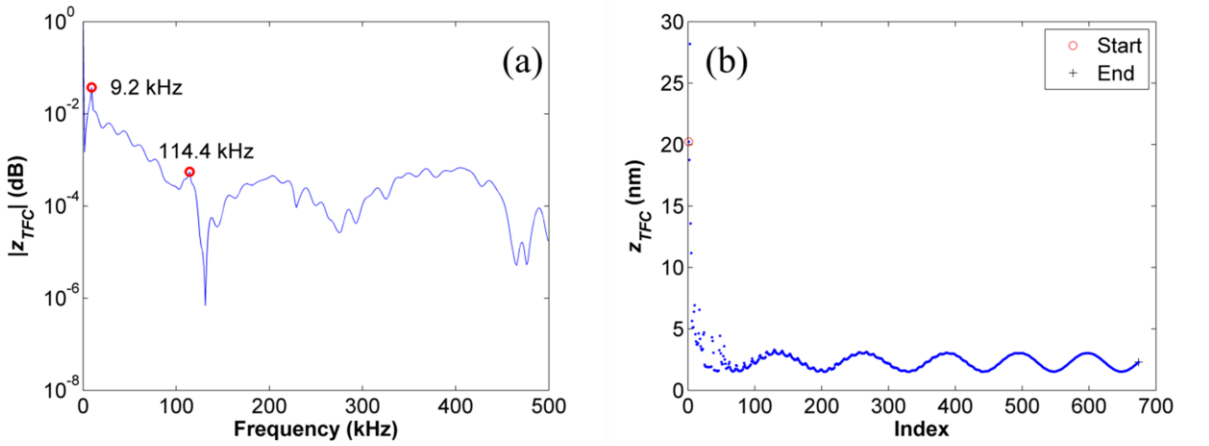


Figure B.5: Steady lubricant contact response for pure sinusoidal excitation and variable TFC actuation: FFT plot (a); and, Poincaré plot (b).

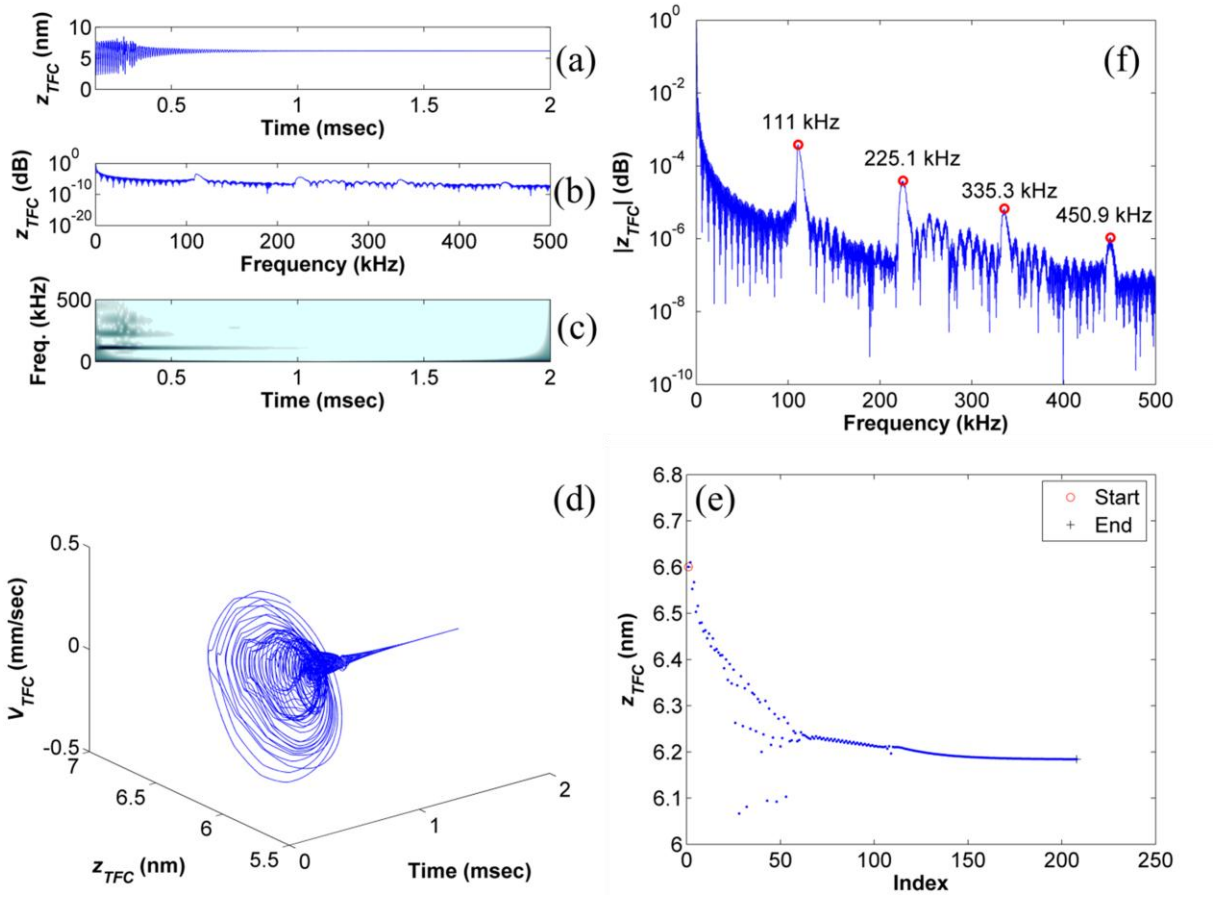


Figure B.6: Slider response for no excitation: time domain signal (a); FFT plot (b); WT plot (c); phase space plot (d); Poincaré plot (e); and, close-up of FFT (f).

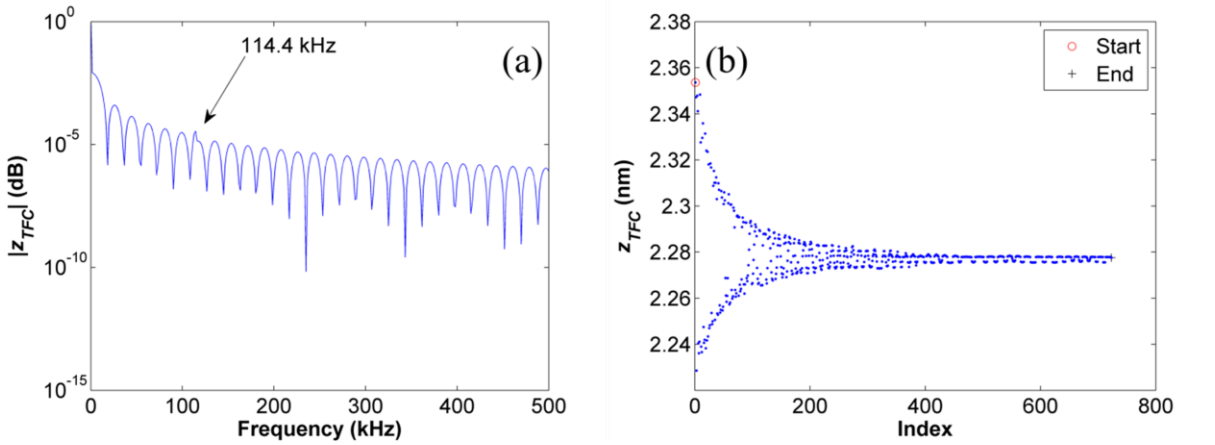


Figure B.7: Steady lubricant contact response for no excitation and variable TFC actuation: FFT plot (a); and, Poincaré plot (b).

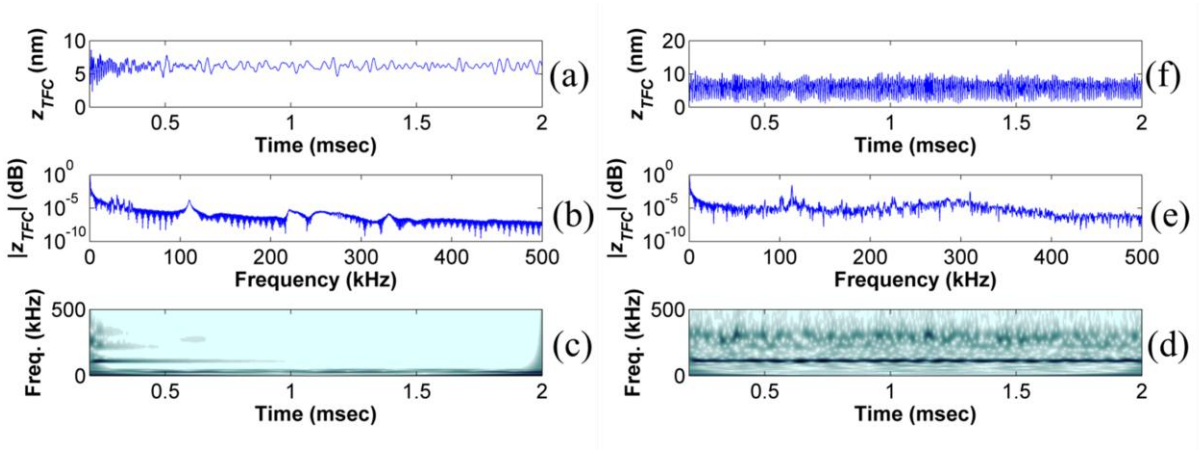


Figure B.8: Slider response for random excitation in the bandwidth of 10-50 kHz (a-c) and 80-320 kHz (d-f): time domain signals (a, f); FFT plots (b, e); WT plots (c, d).

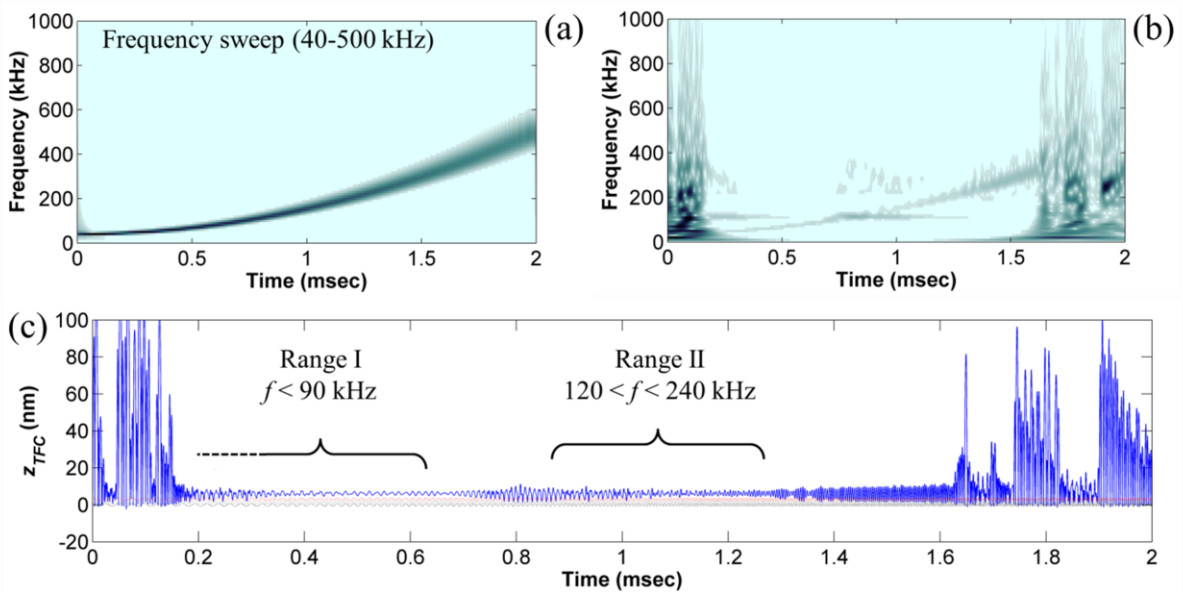


Figure B.9: Frequency sweep signal excitation response (40-500 kHz): Input signal WT plot (a); TFC bulge response WT plot (b); TFC bulge displacement with operating ranges (c).

APPENDIX C

Experimental measurements of the slider surface roughness and the TFC bulge profile during actuation were performed by the author and are summarized below. These results were used as inputs to the dynamic contact models. Additional experiments were performed – but are not presented here – to measure the disk roughness and DMW; the methodology used to measure disk roughness is summarized in the following section. Multiple velocity and displacement time histories were measured using a Laser Doppler Velocimeter (LDV), precisely timed using a Laser Nano-Sensor (LNS), and averaged to yield the DMW signal. The methodology for the DMW measurements is described in detail in the literature [108, 109].

C.1: ROUGHNESS MEASUREMENTS

The roughness of the slider surface in the vicinity of the read/write elements was measured using Atomic Force Microscopy (AFM). To properly mount and secure the head-gimbal assembly containing the slider, the author designed a mounting rig in Pro-Engineer, shown in Figure C.1, and used stereolithography to manufacture the prototype. The sliders used for the measurements were provided by Samsung Information Systems America (SISA). Their roughness parameters were extracted using Dimension AFM's Nanoscope software as well as a custom MATLAB GUI program developed by the Microtribodynamics Laboratory. Smaller, 1×1 μm^2 areas were selected within the larger scans (20×20 and 7×7 μm^2) to exclude artifacts for use with the Nanoscope software. As waviness becomes an issue for large scan sizes in the AFM, the scans were flattened using the Nanoscope software before any further analysis was performed.

A sample AFM image of the measured surface is shown in Figure C.2. The raw data was flattened and the roughness was characterized. The roughness properties used in the models are the RMS roughness σ, the mean radius of asperity R and the areal density of asperities η. In the absence of actuation, the average values of the RMS roughness, mean radius of asperity (or summit) and area density were calculated via the Nanoscope program as 0.381±0.031 nm, 411.237±41.081 nm and 29.708±3.114 μm^{-2} respectively. The roughness parameter β, defined as the product $\sigma R\eta$, is 0.00465±0.00069 and is well below the smallest allowable value of 0.0193

[110]. This hints to errors in the extraction of the roughness parameters. Such errors could occur with RMS roughness values that are of the same order of magnitude as the measurement error but can be addressed by using filtering of the raw data as well as more robust methods of defining and calculating the roughness parameters. The Microtribodynamics Laboratory MATLAB GUI program is able to filter and extract the roughness parameters from profilometric data [111]. The GUI program yields β values above 0.0193, meaning that the filtering applied to the data and the different methodology of defining asperities is more accurate than the Nanoscope software for such atomically smooth surfaces.

Comparison of the non-actuated and actuated roughness parameters for the same area of the slider (containing the read/write elements and the TFC bulge) was performed to understand whether thermal effects and structural deformation at the site of the TFC bulge cause changes in the roughness. One would expect that the effect of actuation on roughness would be small to negligible because of the extremely small deformations involved. After mild filtering, the roughness parameter β lies within the expected range. Referring to Figure C.3, no discernible trend exists in the RMS roughness or the mean radius of asperities; in comparison, there appears to be an increasing trend with TFC actuation for the areal density. The RMS roughness is 1.247±0.153 nm, the mean radius of asperities is 0.406±0.0540 μm, and the areal density of asperities is 74.347±6.125 μm^{-2}. Also shown in Figure C.3 are the corresponding roughness parameters measured on the air bearing surface (ABS), i.e. away from the TFC bulge. The discrepancy between the ABS values and the TFC bulge roughness can be explained by the fact that the location of the bulge contains both AlTiC and Alumina sections, whereas the ABS is fully on AlTiC. The AlTiC and Alumina surfaces could very well have different roughness characteristics. The upward trend of the areal density can be examined more closely by expressing the standard deviations of the quantities as percentages of their mean values. Specifically, the RMS roughness varies by 12.27%, the mean radius of asperities varies by 13.30%, and the areal density of asperities varies by 8.23% from its mean value. In this context, the trend of the areal density of asperities is not significant when compared to that of the other quantities. Hence, the roughness of the TFC bulge can be assumed constant with TFC actuation.

C.2: TFC GEOMETRY MEASUREMENTS

Experiments were performed for various sliders where the TFC bulge was actuated and a profilometer was used to image the resulting profile at the location of the read/write elements. The results presented here were obtained for Seagate STX AAB sliders, commercially available in 7,200 RPM Seagate HDDs. Applied power was varied from 0 to 90 mW, resulting in actuations up to 27 nm, based on the reported TFC efficiency of 0.3 nm per mW. A KLA-Tencor P-4 stylus profilometer was used to make 3D surface measurements of the slider with a reported depth resolution of 0.078 nm. The lateral resolution was 0.5 μm in the scanning direction and 1.0 μm between each scan line. The resulting 3D surface scans were analyzed using custom MATLAB code, developed by the author, which could apply leveling and filtering to the raw data to better visualize the protrusion. After sufficient experimentation, it was decided to eschew filtering altogether so as to retain all the features of the raw scan. Hence, only leveling was applied to the data reported here.

The sliders were 700×1,235 μm in size. The sizes and depths of each feature on the air bearing surface are shown in Figure C.4. The location of the read/write elements could be identified by the protective shields on the Alumina section of the slider; the location of the TFC bulge was expected to be in the vicinity of the protective shields and in the center of the trailing edge. While total area scans of 200×300 μm were taken, the analyzed area was a smaller selection of the total to exclude as much as possible the steep drop at the TE. This drop resulted in scanning artifacts from the profilometer, which is programmed to avoid crushing the stylus on the surface by pulling up upon detection of a sudden change in topography. These artifacts are clearly seen in Figure C.5 and could be mistaken for the TFC bulge because of the similarity in scale. However, the TFC bulge should be offset from the trailing edge so as to coincide with the location of the read/write elements; hence, the artifacts are not considered.

From the scan lines of Figure C.5 one can observe that a bulge exists at the location of the read/write elements before any power is applied to the slider. It is possible that this bulge increases in height by as much as two nanometers; however, this is not entirely clear from these results. Note that, in order to visualize the three-dimensional bulge, a scan line is selected at the approximate center of the topography, and two additional scan lines at +/- 6 μm from the

centerline are plotted as well. The resolution (step between scan lines) in the direction of the width, corresponding to the plots of Figure C.6, is 1.0 μm resulting in a more jagged appearance of the contours. These plots show a step in the topography (approximate width is 100 μm at the AlTiC-Alumina border), whose height increases by about 20 nm and which, within the context of the 3-DOF model is defined as the TFC base. Hence, TFC actuation, which comes partly – if at all – from the bulge itself (2-5 nm) and principally from the surrounding mass (~20 nm), results in an overall height change sum of 22-25 nm and is close to expected value (~27 nm for 0.3 nm/mW efficiency). The side profile of the TFC bulge is not exactly that of an ellipse; nevertheless, and given the high aspect ratio of these plots, the complex shape can be modeled sufficiently accurately as an ellipsoid as far as contact is concerned.

Based on the presented experimental measurements, it seems that a small bulge is actuated towards the disk surface through expansion of the entire material volume surrounding it. Therefore, the surface around the bulge is, itself, also actuated and bulges from the reference (or zero) surface. A more realistic model of the actuated TFC bulge could attribute a small percentage of the total actuation height to expansion of the bulge itself and the remaining, much larger height gain to expansion of the underlying material. This actuation model was formulated and included in the 3-DOF model presented in Chapter 4. The location and size of the TFC bulge, as shown in Figure C.7, is not very different from what was extracted from finite element simulations and used in previous work.

C.3: FIGURES

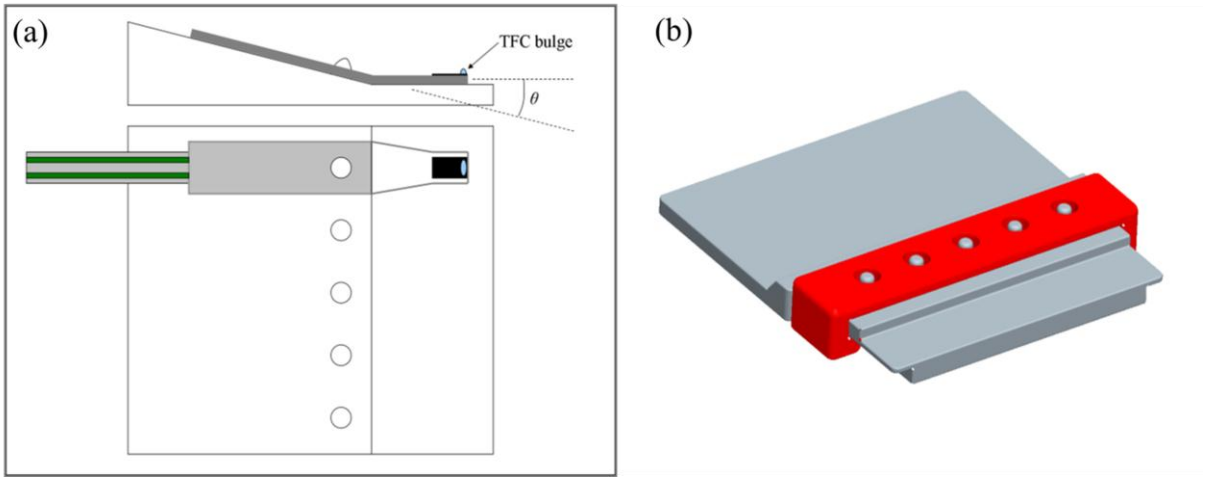


Figure C.1: Custom mounting rig schematic (a) and Pro-Engineer model (b) design for roughness measurements.

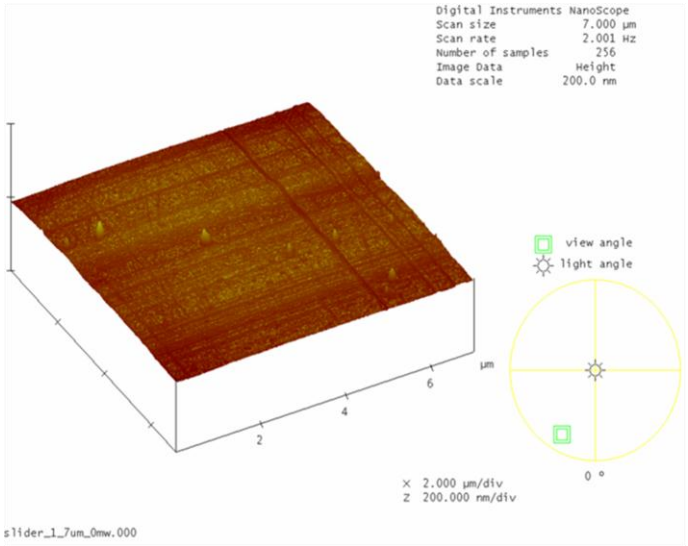


Figure C.2: AFM scan of slider surface in the vicinity of TFC bulge.

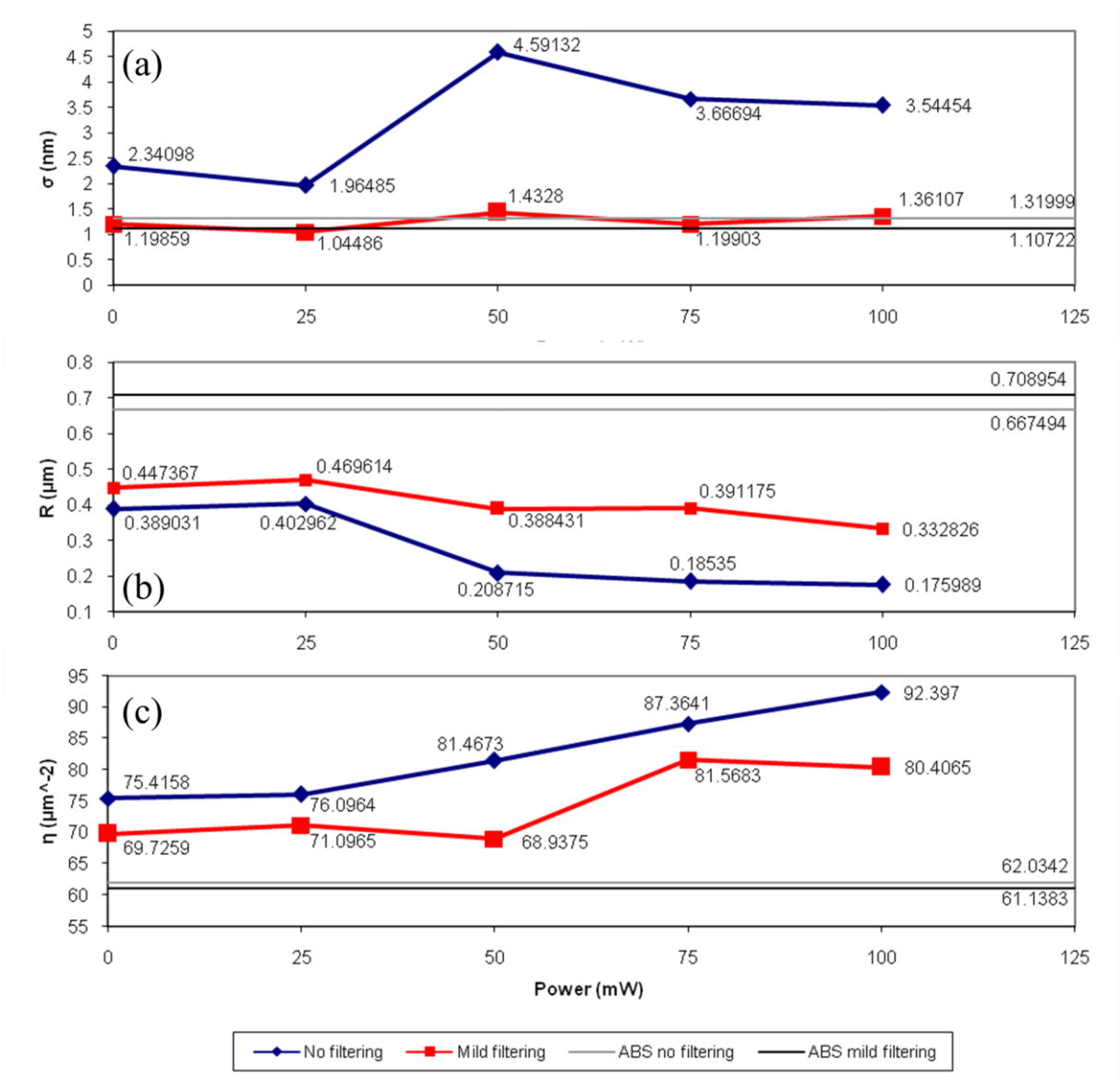


Figure C.3: Roughness parameters as functions of TFC actuation power: (a) RMS roughness; (c) mean asperity radius; and, (c) areal density of asperities. Also shown (horizontal lines) are the roughness parameters measured elsewhere in the ABS; these are to be used as reference values.

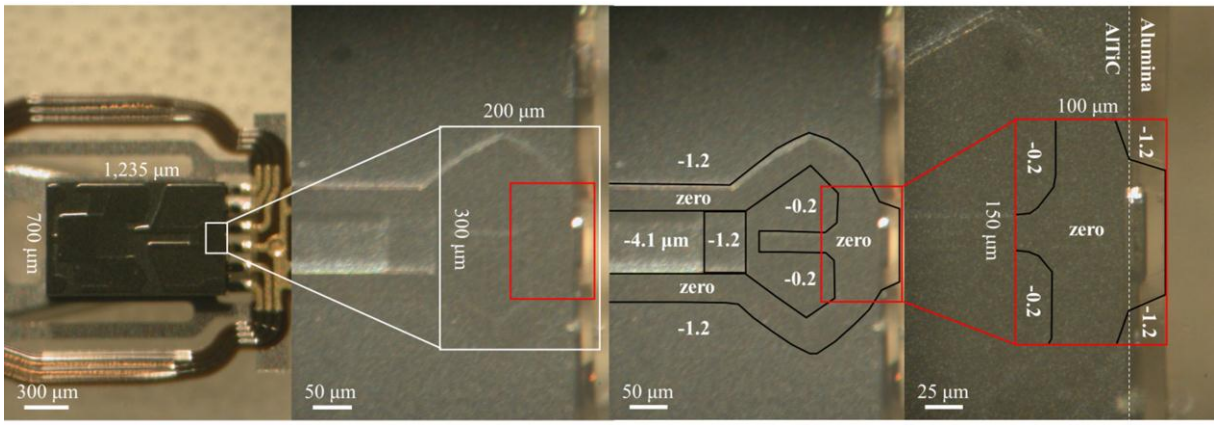


Figure C.4: Microscope images showing the location of features (outlined) on the scan area for Seagate sliders. Depths on the air bearing surface are reported in µm.

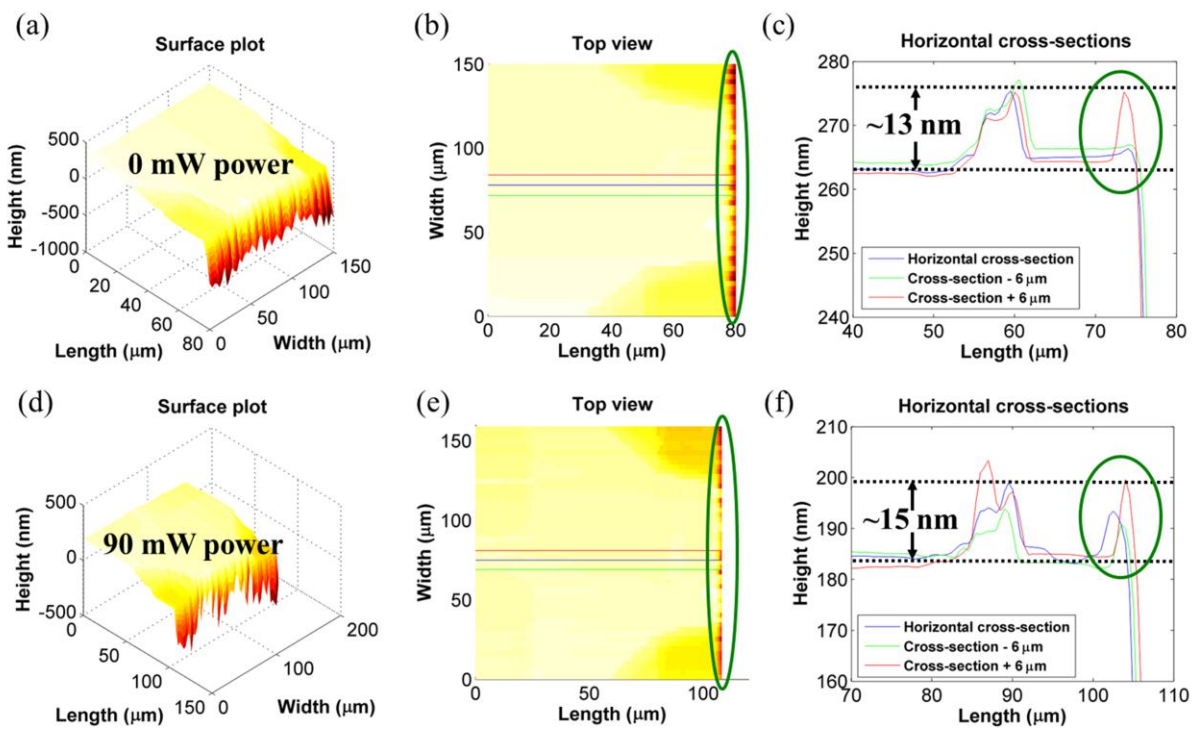


Figure C.5: Experimentally measured profiles along the length direction for 0 mW (a-c) and 90 mW (d-f) applied power. Edge effects are present at the TE.

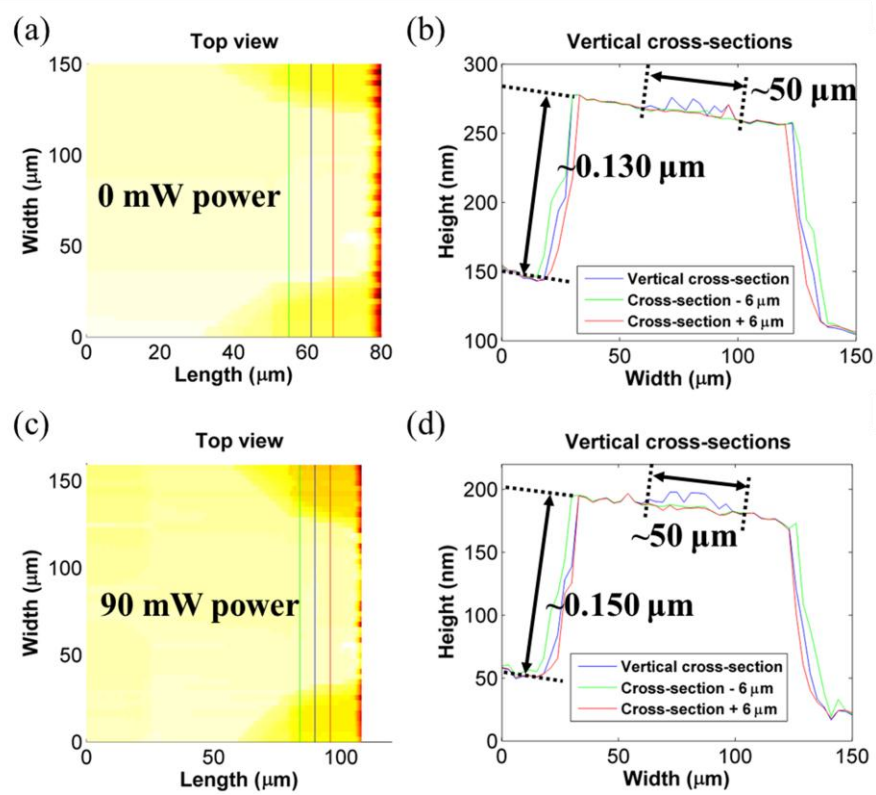


Figure C.6: Experimentally measured profiles along the width direction for 0 mW (a-b) and 90 mW (c-d) applied power.

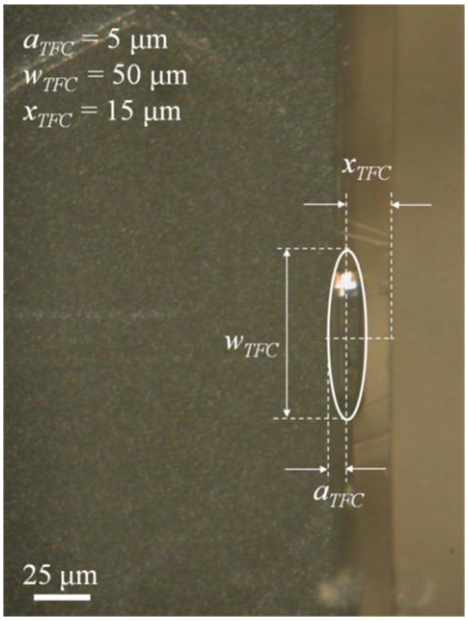


Figure C.7: TFC bulge location and dimensions identified from profilometric scans.